Dynamical Formation and Manipulation of the Persistent Spin Helix

DISSERTATION

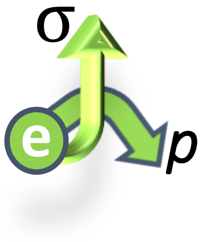

A thesis submitted in partial fulfillment
of the requirements for the degree of

Dr. rer. nat.

to the Faculty of Physics
TU Dortmund University, Germany

by
Felix Paßmann

Dortmund, February 2019

technische universität
dortmund

Accepted by the Faculty of Physics of the TU Dortmund University, Germany.

Day of the oral examination: 12th of April 2019 - Dortmund, Germany

Examination board:
Prof. Dr. Markus Betz
Prof. Dr. Mirko Cinchetti
Prof. Dr. Sergey A. Tarasenko
Prof. Dr. Jan Kierfeld
Dr. Julia Nase

Kurzfassung

Das Verständnis und die Manipulation der Elektronenspindynamik und des Transports in niedrigdimensionalen Halbleiter-Nanostrukturen ist eine Schlüsselanforderung für funktionale Quantentechnologien. In dieser Arbeit wird ein zeit- und ortsaufgelöstes magneto-optisches Kerr-Mikroskop eingesetzt. Dieses ermöglicht es die Wirkung von impulsabhängigen effektiven Magnetfeldern auf die Spin-Dynamik eines zweidimensionalen Elektronengases in GaAs und CdTe Quantentrögen mit hoher Ladungsträgermobilität zu untersuchen. Beide Strukturen verfügen über eine nahezu ausgeglichene Dresselhaus und Rashba Spin-Bahn-Kopplung, die das Entstehen einer unidirektionalen Spinwellentextur mit SU(2)-Symmetrie, der sogenannten persistenten Spin-Helix, ermöglicht. Die Spin-Bahn-Kopplung kann direkt aus dem experimentell gemessenen kohärenten Spin-Präzessionsmuster quantifiziert werden. Es wird beobachtet, dass die Anwendung von (i) Magnetfeldern in der Quantentrogebene die Extraktion der Spin-Bahn-Kopplungsparameter ermöglicht. (ii) Gate-Felder die senkrecht zur Ebene angelegt werden variieren sowohl den Rashba- als auch den kubischen Dresselhaus-Parameter und (iii) elektrische Felder in der Ebene verändern die Modulationsfrequenz der Spin-Helix und den Diffusionskoeffizienten. (iv) Optische Dotierung der CdTe Probe führt zu einer Feinabstimmung der Spin-Helix durch räumliche Gradienten der Spin-Bahn-Kopplungsparameter. Die anschließende präzise Abstimmung aller Spin-Kontrollmechanismen ermöglicht die Unterdrückung von effektiven Magnetfeldern während des Spintransports, so dass die Spinorientierung erhalten bleibt. Alle experimentellen Ergebnisse werden durch Simulationen, basierend auf der Monte Carlo Methode und der kinetischen Theorie bestätigt.

Abstract

Understanding and manipulating the electron spin dynamics and transport in low-dimensional semiconductor nanostructures is a key requirement for functional quantum technologies. In this work, a time- and space-resolved magneto-optic Kerr microscope is employed to explore the effect of momentum-dependent effective magnetic fields on the spin dynamics of a two-dimensional electron gas in high-mobility GaAs and CdTe quantum wells. Both structures feature nearly equal Dresselhaus and Rashba spin-orbit coupling, enabling the emergence of a unidirectional spin wave texture with SU(2) symmetry, the so-called persistent spin helix. The spin-orbit coupling can be quantified directly from the experimentally measured coherent spin precession pattern. It is observed that application of (i) perpendicular in-plane magnetic fields allows for the extraction of the spin-orbit coupling parameters. (ii) Out-of-plane gate fields tune the Rashba and cubic Dresselhaus parameter directly and (iii) in-plane electric fields vary the modulation frequency of the spin helix and the diffusion coefficient. The CdTe sample reveals a fine tuning of the pattern via (iv) optical doping, creating a spatial gradient of the spin-orbit coupling parameters. Precise engineering of all spin control mechanisms enables a regime of locked spin transport where the effective magnetic fields are suppressed. All experimental results are supported by qualitative kinetic theory and Monte Carlo simulations.

Contents

Foreword

Spintronics - The historic development

With the disruptive unfolding of the second quantum revolution during this decade the first century of quantum mechanics is coming to an end. Today, the emerging ability to manipulate single quantum objects opens the access to a fundamentally new way of information processing based on quantum technologies [1].

Looking back on the beginning of quantum physics about 90 years ago, this new theory enabled a feasible explanation for various experimental findings. Among these discoveries was the observation of Stern and Gerlach who had, without knowing it, observed the space quantization of the spin angular momentum in their famous silver beam experiment in 1922 [2]. Further considerations by Goudsmit and Uhlenbeck led to the postulation of the spin as an intrinsic electron property beyond the classical model [3; 4]. In 1928 this considerations culminated in the theoretical derivation of the electron spin by Dirac, who combined quantum mechanics with the theory of special relativity in his eponymous equation [5].

Parallel to the exploration of spin in physics, the silicon based complementary metal-oxide-semiconductor (CMOS) transistors were invented in the 1960s [6]. This development laid the foundation for classical information technologies. CMOS transistors are based on the classical electron charge and have shown an enormously growing influence on daily life. However, it was indirectly observed by Moore in 1965 [7] that the exponential increase of the clock speed in integrated circuits is related to an equally fast miniaturization. Inevitably, this rapid miniaturization is going to encounter physical limits at some point. Generally, this point is dictated by the restrictions to heat dissipation in densely populated chips and ultimately by tunneling effects. Such quantum effects become ineluctable if structure features fall below (10×10) atoms by size [8]. By today, chip manufactures approach the so called 7 nm generation of transistor technology. Although the product naming is not directly aligned with the actual feature size that can be of an order of magnitude higher [9], the pace of innovation is slowing down. This manifests in the cadence of the exponential growth that increased already from two years in 1965 to almost three years today [10]. Predicted by Moore's law this impending slow down triggered the emergence of a new research field called spintronics during the 1980s.

Spintronics represents a new technology that extends or even replaces the electron charge with the quantum mechanical spin as the core element of information processing devices. Being subject of fundamentally different physical phenomena, spin based technology is expected to bypass limitations of their charge-based counterparts. For instance, the switching speed is no longer limited by capacitance and drive current but the spin precession frequency which can reach into the THz range [11]. Moreover, spintronics promises to circumvent the miniaturization limits that result from heat dissipation. For spin based transistors the energy needed for switching can potentially be reduced far below the theoretical lower limit of field-effect transistors (FET) [12]. Spintronics originated from magneto-electronic research some thirty years ago [13]. During this time a series of groundbreaking discoveries made a rapid transition towards industrial information technologies especially in the field of memory devices. This period started with the first observation of tunnel magnetoresistance (TMR) in 1975 [14] and was followed by the injection of spin polarization from a metal-ferromagnetic interface in 1985 [15]. Subsequently, the discovery of giant magnetoresistance (GMR) in 1988 [16; 17] triggered the first implementation of the spin valve, marking a fundamental breakthrough that was rewarded with the Nobel prize in 2007 for Fert and Grünberg. Until today, magnetoresistance plays a vital role for application as in non-volatile magnetoresistive random access memories (MRAMs). With their proposal of a spin-FET in 1990 [18], Datta and Das initiated a trend to make spintronic devices available not only for information storage but as well for the data processing itself. This led to some of the most recent developments in the area of quantum computing.

Envisioned by replacing the conventional bits in computational devices with quantum mechanical two-level systems, the so called qbits, quantum computing promises novel advancements. Due to their fundamentally different functionality quantum computers are highly advantageous for specific tasks. This includes quantum simulations and the search in data bases [19]. In this field, most recent progress was done in quantum mechanical systems based on trapped ions [20] or Josephson junctions in superconducting circuits [21]. Nevertheless, spintronic devices are still promising candidates as shown by recent publications that utilize electron spins in individually addressable quantum dots [22; 23]. Such low-dimensional semiconductor systems are conveniently realized in II/VI or III/V materials. Within this systems, confined spins can be Zeeman split to form a two-state qubit, providing favorable conditions for efficient optical injection and read out of information [24].

It is a staggering advance that links the first steps of Stern and Gerlach, over the last century of quantum physics, with today's prototype quantum computers. However, spintronics is not yet employable as a real alternative to the charge-only-based silicon technology and might never be [25]. Challenges concern primarily the loss of coherence when spin polarized carriers cannot be sufficiently isolated from there environment and their quantum mechanical phase information is deteriorated, reducing the spin lifetime. A remarkable long coherence has already been achieved, but it is an ongoing debate whether the required hermetic separation for hundreds of microseconds at room-temperature is at all thermodynamically possible [26], especially, if a high number of qubits is pursued [27].

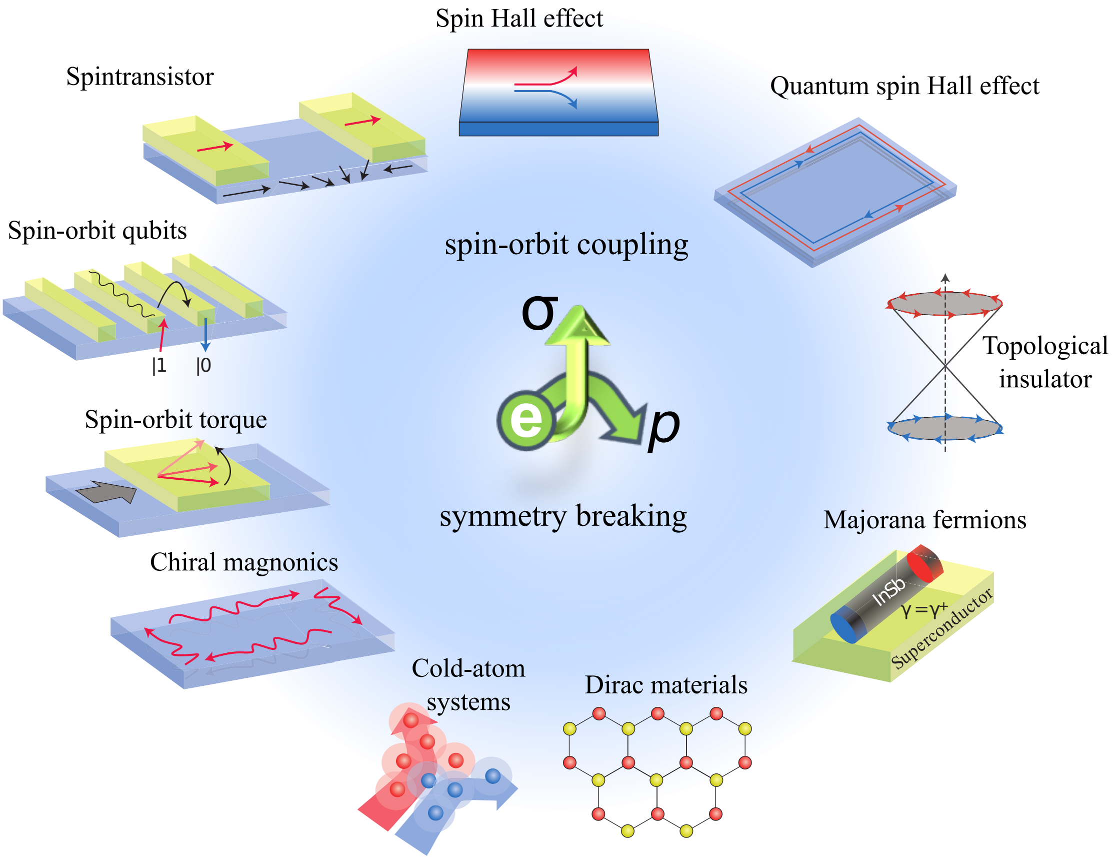

Fig. 1: The family of spin-orbit coupling induced phenomena which are present in recent discoveries of physics and material science. Red and blue colored features illustrate the two polarization states of the spin respectively. Adapted from Manchon *et al.* [29].

Spin-orbit coupling

For spintronics the most relevant limitation arises from randomly oriented, internal effective magnetic fields. These fields are provoked by elevated doping densities and internal electric fields, being commonly employed in state of the art semiconductor structures [11; 28]. Effective magnetic fields result from a relativistic effect called spin-orbit coupling. Acting as spatially and temporally fluctuating torques on the spin magnetic moment, effective fields destroy the coherent spin state of an ensemble. As a consequence of this severe impact, spin-orbit coupling is at the very center of current research. The field of spin-orbitronics forms a branch of spintronics, since it involves an intrinsic coupling of the electron momentum with the quantum nature of spin [29; 30]. It is, therefore, of the utmost importance to continue the research in spintronics and the fundamental physics behind quantum information technologies.

Figure 1 converges a broad selection of groundbreaking effects from material science to physics. All phenomena are fundamentally driven by spin-orbit coupling as a consequence of broken inversion symmetry. The depicted schemes link spin transport phenomena and promising device prototypes with novel states of matter. The spin Hall effect reveals a polarization-dependent mutual conversion of charge- and spin currents [31; 32] whereas spin-orbit qubits [33] and torques [34] stimulate new ways of information storage and processing respectively. In addition, spin-orbit coupling is at the center of the topological state of matter and thus the Nobel prize-winning work of Kosterlitz, Thouless and Haldane [35]. Their work initiated the discovery of topological quantum spin Hall insulators [36] and fermionic Majorana states in superconductor-semiconductor hybrid systems [37] that were originally predicted for graphene. Last but not least, the subfield of two-dimensional Dirac materials around honeycomb crystals represents a new and dynamic area of research. Such structures are found for example in transition metal dichalcogenides (TMDCs), where extreme spin-orbit coupling leads to spin splitting phenomena with immense influence on the closely related valleytronics [38].

The persistent spin helix

The importance of spin-orbit coupling for controlled spin transport serves as motivation for the intensive study of the persistent spin helix in this dissertation. The persistent spin helix is a two-dimensional pattern of spin polarization that arises when electrons propagate through a quantum well with a lack of inversion symmetry. The underlying theory was developed in 1955 and 1960 by Dresselhaus [39] and Rashba [40]. From the bulk inversion symmetry of the crystal and the potential drop in layered semiconductor heterostructures they predicted the emergence of effective magnetic fields. The pattern of the spin helix is inherently shaped by these effective magnetic fields and is therefore an ideal tool for investigating the functionality and manipulation of spin-orbit coupling [41–43].

This thesis comprises a Theoretical Background Chapter focused on the sample properties and the spatiotemporal electron dynamics that are needed to create a spin helix. Parameters that quantify spin-orbit coupling due to Dresselhaus and Rashba inversion asymmetries are introduced. Following the pioneering work of Bernevig *et al.* [44; 45], a balance in the Rashba and Dresselhaus regime creates an enhanced symmetry of the momentum-dependent effective magnetic field. This symmetry suppresses the Dyaknonov-Perel dephasing mechanism, resulting in substantially elevated coherence times up to several nanoseconds at cryogenic temperatures [46; 47]. Further aspects of the persistent spin helix such as diffusive and ballistic spin transport and spin decay are as well covered in the first chapter.

An all-optical detection of the spin helix, which relies on the magneto-optical Kerr effect, has replaced the initially used spin-grating technique as method of choice. This is shown by the approach of Salis *et al.* [48] that allows for a more general extraction of information than for instance magneto-conductance measurements [49] or Raman spectroscopy [50]. The according optical experiment, used in this thesis, is described in the Experimental Techniques Chapter 2.

Being interested foremost in the manipulation of spin-orbit coupling, the Experimental Results Chapter 3 centers on the exploration of possible tuning knobs. External magnetic fields add vectorially to the effective magnetic fields in the quantum well sample and thus help to measure the spin-orbit coupling strength directly [51]. In addition, electric fields applied in- plane and out-of-plane have proven to be precise and effective controls for the spin-orbit properties of the system [52–54]. However, controversial effects of in-plane fields have been reported recently by Kunihashi *et al.* [55] and Anghel *et al.* [51]. This contradiction will be thoroughly discussed and backed with more detailed data. A full characterization of the spin helix observed in CdTe proofs the universality of the persistent spin helix as first study in a II/VI quantum well [56]. In this material, optical doping is revealed as an additional lever for fine tuning the spin-orbit coupling. In the end of the chapter, a novel combination of the various tuning knobs leads to a fully controllable traveling spin helix. This phenomenon is harnessed to propose a new functionality for spintronic switches.

The scope of the studies carried out in the context of this work is of course limited and many other aspects related to the persistent spin helix cannot be covered. Among these aspects is a variety of application oriented publications that deal with the effect of narrowed quantum well channels on the evolution of the spin helix [57]. Moreover, dual modulation-doping geometries of the surrounding heterostructure allow for quantum wells to form a two-subband system. In such systems a stretchable PSH with simultaneous modulation of Rashba and Dresselhaus spin-orbit coupling has been realized [58]. Promising theoretical work for the creation of crossed spin helices is done [59; 60] which predicts the observation of a topologically non-trivial Skyrmion-lattice in a semiconductor electron gas as the result of two superposed spin helices [61].

Chapter 1

Theoretical Background

The persistent spin helix is the main subject of this work. A thorough understanding of the theory behind this phenomenon is therefore at the heart of this Theoretical Background Chapter. Section 1.1 at the beginning of this chapter is focused on the genuine quantum mechanical spin property of electrons. Spin is introduced as an intrinsic angular momentum of the electron and its quantum mechanical origin is derived from the Dirac equation, predicting simultaneously the effect of spin-orbit coupling. Starting from the quantum mechanical idea of angular momentum in Section 1.2, the focus is shifted from individual spins to aspects of macroscopic ensembles in the environment of highly ordered semiconductor crystals. Special emphasis is placed on the role of light in the injection and manipulation of electron spins within the semiconductor band structure. Since the experimental work in this thesis is based on a two-dimensional electron gas, an additional focus is placed on the effects caused by the spatial confinement of the electron wave function. Subsequently, the last Section 1.3 gives an overview of the interplay between temporal and spatial dynamics, including diffusion, drift and the relaxation of spins. Furthermore, the effect of spin-orbit coupling is investigated in order to identify the Rashba and Dresselhaus contributions present in two-dimensional heterostructures where the crystal lattice lacks an inversion center. These two contributions are associated to asymmetric potentials and can be engineered so that they are balanced out. A theoretical framework for this regime is developed and allows for a first understanding of the PSH texture as a tool for the study and manipulation of spin-orbit coupling. Finally, a theoretical discussion of characteristic PSH features is given, including the strongly enhanced lifetime of the spin polarization.

1.1 The Discovery of Spin

1.1.1 The Electron Spin

Following the formalism of quantum mechanics, certain classical observables such as the angular momentum $\boldsymbol{L} = \boldsymbol{r} \times \boldsymbol{p}$ where $\boldsymbol{r}$ is the position vector and $\boldsymbol{p}$ is the vector of momentum can be described by a discrete set of eigenstates $|l, m_\mathrm{l}\rangle$ and eigenvalues (l, m_l). These eigenvalues are accessible via the corresponding orbital angular momentum operator $\hat{\boldsymbol{L}} = (\hat{L}_\mathrm{x}, \hat{L}_\mathrm{y}, \hat{L}_\mathrm{z})$.

Sharing a mutual basis, it appears convenient to diagonalize $\hat{\boldsymbol{L}}^2$ and $\hat{L}_\mathrm{z}$ as $[\hat{\boldsymbol{L}}^2, \hat{L}_\mathrm{z}] = 0$ while the individual components of $\hat{\boldsymbol{L}}$ do not commutate with each other. As a result, the expressions

$$\hat{\boldsymbol{L}}^2|l, m_\mathrm{l}\rangle = \hbar^2 l(l+1)|l, m_\mathrm{l}\rangle \qquad \hat{L}_\mathrm{z}|l, m_\mathrm{l}\rangle = \hbar m_\mathrm{l}|l, m_\mathrm{l}\rangle \tag{1.1}$$

can be written down where $\hbar$ denotes the reduced Planck constant while m_l and l are the magnetic and azimuthal quantum number respectively. Moreover, the eigenstates are assumed to be normalized, allowing for the restriction of $m_\mathrm{l} = -l \ldots l$ to a quantized set of integer values. Consequentially, $l = 0, 1, 2, 3 \ldots$ is given, implying an uneven number of $2l+1$ eigenstates for the orbital angular momentum. These general considerations are not limited to the orbital angular momentum but can be applied to every angular momentum [62; 63].

From here, the interaction Hamiltonian for an electron exposed to a constant magnetic field $\boldsymbol{B} = (B_\mathrm{x}, B_\mathrm{y}, B_\mathrm{z})$ is given by $\hat{H}_\mathrm{int} = -e/(2m)\boldsymbol{B} \cdot \hat{\boldsymbol{L}}$ where c represents the speed of light, e the charge and m the mass of the electron. Accordingly, the quantum operator for the magnetic moment can be introduced as $\hat{\boldsymbol{\mu}}_\mathrm{l} = -e/(2m)\hat{\boldsymbol{L}}$. Thus the applied magnetic field is expected to lift the degeneracy of the $2l+1$ eigenstates, yielding the energy eigenvalues $\mu_\mathrm{B} B m_\mathrm{l}$ where $\mu_\mathrm{B} = -e\hbar/(2m)$ defines the Bohr magneton [62; 63].

In the beginning of quantum mechanics, this considerations represented an established explanation for the magnetic field induced emergence of an uneven number of spectral sub-level lines in atomic spectroscopy. This emergence of sub level lines was known as the normal Zeeman effect [64]. However, the above derived formalism was in strong contradiction with two specific experimental observations of that time. Firstly, the appearance of even numbered level splittings in atoms with uneven atomic charge number Z and secondly the anomalous Zeeman effect* which describes an energy splitting approximately two times higher than predicted by the Bohr magneton [65; 66]. The combination of both phenomena is observable in the Stern-Gerlach experiment where a beam of silver atoms is split into two beams by an applied magnetic field gradient [2]. Here, the field gradient couples to the magnetic moment and deflects the atoms in a direction that depends on the sign of this moment. As the magnetic moment of a silver atom is entirely determined by the single $5s$ electron the observed even number of two resulting beams is incompatible with an integer azimuthal quantum number.

This inconsistency prompted Goudsmit and Uhlenbeck to postulate an intrinsic angular momentum of the electron called spin for which there is no analogue in the classical theory [3; 4]. This new quantum number s relaxes the restriction for possible values of the corresponding quantum number to half-integers like $s = 0, \frac{1}{2}, 1, \frac{3}{2}, 2 \ldots$. Furthermore, the spin permits the appearance of two eigenstates $| \downarrow / \uparrow \rangle = |\frac{1}{2}, \pm\frac{1}{2}\rangle$ in the case of an electron where $s = \frac{1}{2}$ and $m_\mathrm{s} = \pm\frac{1}{2}$. Choosing an orientation along z yields the eigenvalue equation

$$\hat{S}_\mathrm{z} \begin{pmatrix} |\uparrow\rangle \\ |\downarrow\rangle \end{pmatrix} = \frac{\hbar}{2} \begin{pmatrix} +|\uparrow\rangle \\ -|\downarrow\rangle \end{pmatrix} \tag{1.2}$$

---

[*] The differentiation of the normal and anomalous Zeeman effect has become more and more uncommon. Nowadays, the term anomalous refers mostly to the 1 ‰ deviation of the Landé factor from 2, explainable through effects of quantum electrodynamics [63].

for the electron spin. Here, $\hat{S}_\mathrm{z}$ is the z-component of the spin and equivalent to the orbital angular momentum operator $\hat{\boldsymbol{S}}$. A more general notation is based on the Pauli matrices $\hat{\boldsymbol{\sigma}} = (\sigma_\mathrm{x}, \sigma_\mathrm{y}, \sigma_\mathrm{z})$ [†] such that the eigenvalue equation

$$\hat{\boldsymbol{S}} \begin{pmatrix} |\uparrow\rangle \\ |\downarrow\rangle \end{pmatrix} = \frac{\hbar}{2} \boldsymbol{\sigma} \begin{pmatrix} |\uparrow\rangle \\ |\downarrow\rangle \end{pmatrix} \tag{1.3}$$

is found [62].

Although the postulation of the electron spin provides an explanation for the splitting of the silver beam in the Stern-Gerlach experiment, the observed anomalous magnetic moment remains unexplained. It was not until Einstein's theory of relativity was introduced into quantum mechanics that the missing factor of two could be theoretically reproduced. The resulting Dirac equation represents a Lorentz invariant extension of the Schrödinger equation for spin 1/2 particles and predicts a correction factor g of exactly 2 for the spin magnetic moment $\hat{\boldsymbol{\mu}}_\mathrm{s} = 2\frac{e}{2m}\hat{\boldsymbol{S}}$ (cf. Section 1.1.2 for more details) [5]. This g-factor is commonly referred to as Landé factor or gyromagnetic ratio of electrons [65]. Sharing the same nature of angular momentum, $\hat{\boldsymbol{L}}$ and $\hat{\boldsymbol{S}}$ can be summed up in order to define the total angular momentum operator $\hat{\boldsymbol{J}} = \hat{\boldsymbol{S}} + \hat{\boldsymbol{L}}$ and the according magnetic moment is given by μ_j. This results in a modified interaction Hamiltonian which reads

$$\hat{H}_\mathrm{int} = -\boldsymbol{B} \cdot (\hat{\boldsymbol{\mu}}_\mathrm{l} + \hat{\boldsymbol{\mu}}_\mathrm{s}) \cdot \boldsymbol{B} = \mu_\mathrm{B} \left(\frac{\hat{\boldsymbol{L}}}{\hbar} + \hat{\boldsymbol{\sigma}} \right) \tag{1.4}$$

and allows for a complete description of the electron interaction energy in magnetic fields [63]. The eigenstates are described by the total angular momentum quantum numbers $j = |l \pm s|$ and the corresponding magnetic quantum number $m_\mathrm{j} = -j \ldots j$. Both quantum numbers will be of special importance later on to discuss the possible eigenstates in the band structure of semiconductors (cf. Section 1.2).

1.1.2 The Dirac Equation

In quantum mechanics, the Schrödinger equation represents the fundamental description of systems, ranging from the atomic to the macroscopic level. However, regardless of its success in explaining and predicting a vast selection of phenomena beyond classical mechanics, it lacks compatibility with the theory of relativity. Aiming at a more complete picture, Dirac's approach of linearizing a relativisticly invariant version of the Schrödinger equation finally bridges these two fields of physics. Moreover, it allows for a theoretically stringent deduction of the electron spin and the anomalous Zeeman effect. This outcome is particularly important as both effects were only experimentally observed until this point. In the following Section,

---

[†] Forming a basis for 2×2 hermitian matrices, $\boldsymbol{\sigma}$ defines as

$$\sigma_x = \begin{pmatrix} 0 & 1 \\ 1 & 0 \end{pmatrix} \quad \sigma_y = \begin{pmatrix} 0 & -i \\ i & 0 \end{pmatrix} \quad \sigma_z = \begin{pmatrix} 1 & 0 \\ 0 & -1 \end{pmatrix} .$$

the Dirac equation is schematically derived for an electron coupled to an electromagnetic field. For a mathematically more in-depth discussion the reader is referred to literature [5; 62; 67].

As a starting point, the squared relativistic energy E of a free electron can be written as

$$E^2 = \sum_{\mu=x,y,z} c^2 p_\mu^2 + m^2 c^4 \quad \text{with} \quad p_\mu = \gamma m v_\mu \tag{1.5}$$

where p_μ is a component of the relativistic momentum vector derived from the corresponding component of the electron velocity vector $\boldsymbol{v} = (v_\mathrm{x}, v_\mathrm{y}, v_\mathrm{z})$ and the Lorentz factor $\gamma = (1 - \boldsymbol{v}^2/c^2)^{-1/2}$ [62]. From this formula Schrödinger, Klein and Gordon had already found before Dirac a second order differential equation by employing the correspondence principle to Eq. (1.5). The correspondence principle allows for the substitution of energy and momentum with their quantum mechanical operators so that they can act on a time- and space-dependent wave function $\Psi(\boldsymbol{r}, t)$ [68; 69]. However, this differential equation suffered from the necessity of knowing not only an initial value for Ψ but as well the first derivation $\partial\Psi/\partial t$ to solve it. Compared to the established Schrödinger equation this change of the requirements appears to be a too drastic modification. A more promising ansatz is found from reformulating expression Eq. (1.5) to

$$\left(E - c\sum_i \boldsymbol{\alpha}_\mathrm{i} p_\mathrm{i} - \beta mc^2\right)\left(E + c\sum_j \boldsymbol{\alpha}_\mathrm{j} p_\mathrm{j} + \beta mc^2\right) = 0 \tag{1.6}$$

by linearization. Here, i,j$\in x, y, z$ and $\boldsymbol{\alpha}_\mathrm{i}$ as well as $\boldsymbol{\beta}$ represent the quadratic 4×4 Dirac matrices identified as

$$\boldsymbol{\alpha}_\mathrm{i} = \begin{pmatrix} 0 & \boldsymbol{\sigma}_\mathrm{i} \\ \boldsymbol{\sigma}_\mathrm{i} & 0 \end{pmatrix} \quad \text{and} \quad \boldsymbol{\beta} = \begin{pmatrix} \mathbf{1}_2 & 0 \\ 0 & -\mathbf{1}_2 \end{pmatrix} \tag{1.7}$$

with $\mathbf{1}_2$ denoting the 2×2 unity matrix[‡]. The linear character of Eq. (1.6) is used to derive a solution for the whole equation by looking at only one of its two terms. Accordingly, the principle of correspondence is applied by replacing $E \rightarrow i\hbar\partial/\partial t$ and $\boldsymbol{p} \rightarrow \hbar/i\boldsymbol{\nabla}$ and thus the Dirac equation for free electrons is found to be

$$\left(i\hbar\frac{\partial}{\partial t} + i\hbar c\boldsymbol{\alpha}\cdot\nabla - \boldsymbol{\beta} mc^2\right)|\Psi(\boldsymbol{r}, t)\rangle = 0 \tag{1.8}$$

with the Dirac Hamiltonian $H_\mathrm{D} = c\boldsymbol{\alpha}\cdot\boldsymbol{p} - \boldsymbol{\beta} mc^2$. Reflecting the symmetry of space and time coordinates in the theory of relativity, the found expression is a differential equation of first order of both time and space. Further, the equation requires the wave function $|\Psi(\boldsymbol{r}, t)\rangle$ to be a vector with four components. Such four-dimensional structures are referred to as bispinors where the first two components describe the spin up and down states of an electron respectively. The third and fourth components represent the spin states of an electron-like particle with

---

[‡] This choice for the Dirac matrices is motivated by the fact that $\boldsymbol{\alpha}_\mathrm{i}^2 = \boldsymbol{\beta}^2 = \mathbf{1}_4$ and the fulfillment of the anticommutativities $\alpha_\mathrm{i}\alpha_\mathrm{j} + \alpha_\mathrm{j}\alpha_\mathrm{i} = 0$ and $\alpha_\mathrm{i}\beta + \beta\alpha_i = 0$. These requirements must be met in order to transform Eq. (1.5) into Eq. (1.6) while the desired Lorentz covariance is conserved [62].

positive charge. The latter interpretation together with the appearance of negative energy eigenvalues is interpreted as a theoretical prediction of the positron or anti-electron. Being only interested in the electron these solutions are ignored in the following.

In a final step, the Dirac equation is extended to electrons in electromagnetic fields by including a vector potential $\boldsymbol{A}(\boldsymbol{r},t)$ to the momentum operator. An additional term $e\phi(\boldsymbol{r},t)$ takes account for the energy given to an electron by the scalar potential $\phi(\boldsymbol{r},t)$. These terms are added analogous to the Schrödinger equation for electrons in an electromagnetic field, yielding the Dirac function equivalent as

$$\left\{ i\hbar\frac{\partial}{\partial t} - c\boldsymbol{\alpha}\cdot\left[\frac{\hbar}{i}\nabla - e\boldsymbol{A}(\boldsymbol{r},t)\right] - \boldsymbol{\beta}mc^2 + e\phi(\boldsymbol{r},t)\right\}|\Psi(\boldsymbol{r},t)\rangle = 0. \tag{1.9}$$

Basically, it has to be acknowledged that electrons cannot be described by scalar wave functions anymore if it comes to high energies. Within a moderate energy range, however, the spinors with negative eigenvalues become negligible, coinciding with the general single particle picture. This circumstance is harnessed by the Foldy-Wouthuysen transformation (FWT) which removes the spinor contributions with negative eigenvalues in the non-relativistic limit with $\gamma \approx 1$ [70]. Here, based on canonical transformations, the Dirac equation is split into two equations with two components each. As only the first equation describes the solutions with positive energy eigenvalues it is decoupled from the second set of components. For a detailed discussion of the FWT the reader is referred to further textbook literature where the Dirac equation is given by

$$\begin{aligned}\Bigg\{ & i\hbar\frac{\partial}{\partial t} - mc^2 + e\phi(\boldsymbol{r},t) - \frac{1}{2m}\cdot[\boldsymbol{p}-e\boldsymbol{A}(\boldsymbol{r},t)]^2 + \frac{e\hbar}{2mc}\boldsymbol{\sigma}\cdot\boldsymbol{B} \\ & \underbrace{+\frac{\boldsymbol{p}^4}{c^2 8m^3} + \frac{e\hbar}{4m^2c^2}\boldsymbol{\sigma}\cdot\boldsymbol{\mathcal{E}}\times[\boldsymbol{p}-e\boldsymbol{A}(\boldsymbol{r},t)] + \frac{e\hbar^2}{8m^2c^2}\nabla\boldsymbol{\mathcal{E}}}_{\text{relativictic corrections}}\Bigg\}|\Psi(\boldsymbol{r},t)\rangle = 0\end{aligned} \tag{1.10}$$

with a two component wave function $\Psi(\boldsymbol{r},t)$ called spinor. A thorough comparison of this result with the output of the respective Schrödinger equation reveals the correction terms, stemming from relativistic effects.

The first four terms in equation Eq. (1.10) are equivalent to the Schrödinger equation but include the relativistic energy contribution of the rest mass. The fifth term describes the coupling of the spin moment $\boldsymbol{\mu}_s = \frac{e\hbar}{2m}\boldsymbol{\sigma} = 2\frac{e}{2m}\boldsymbol{S}$ to the magnetic field introduced as Zeeman effect in the previous section. Special attention must be paid to the now correct gyromagnetic ratio $g = 2$ for the electron spin which emerges naturally from the Dirac theory. The remaining three terms are relativistic corrections starting with the relativistic mass correction $\boldsymbol{p}^4/(c^2 8m^3)$. The second correction term describes a coupling of spin and momentum with the electric field which is defined as the gradient of the electric potential $\boldsymbol{\mathcal{E}} = -\nabla\phi$. This interaction is known as spin-orbit coupling and will be discussed in-depth in Section 1.3.4 as the coupling of the electron spin to a self-induced effective magnetic field. For the moment, it is sufficient to point out the similarity of the spin-orbit term $\frac{e\hbar}{4m^2c^2}\boldsymbol{\sigma}\cdot\boldsymbol{\mathcal{E}}\times[\boldsymbol{p}-e\boldsymbol{A}(\boldsymbol{r},t)]$ with the Zeeman Hamiltonian introduced earlier. The spin-orbit term can be rewritten as

$$\frac{e\hbar}{4m^2c^2}\boldsymbol{\sigma}\cdot\boldsymbol{\mathcal{E}}\times\boldsymbol{p}=\frac{e}{2m}\boldsymbol{S}\cdot\frac{1}{mc^2}(\boldsymbol{\mathcal{E}}\times\boldsymbol{p})=\frac{e}{2m}\boldsymbol{S}\cdot\boldsymbol{B}_{\mathrm{so}} \tag{1.11}$$

by assuming the electric field to be rotation free and the vector potential to be zero. The calculation makes use of classical electrodynamics which predicts the induction of a magnetic field in a reference system that moves relatively to an electric field with the velocity $\boldsymbol{v}$. This effect leads to the introduction of the designation effective magnetic field $\boldsymbol{B}_{\mathrm{so}}=(\boldsymbol{\mathcal{E}}\times\boldsymbol{v})/c^2$ for the right side of Eq. (1.11). The term effective magnetic field indicates the possibility that the momentum of an electron in an electric field, will result in a torque acting on the magnetic spin moment of the same electron. Such effective magnetic fields differ from standard magnetic fields in that they maintain time reversal symmetry. This feature has far reaching consequences for the band structure of many materials. The third and last contribution of the corrections is called Darwin term and plays a crucial role for the theoretical explanation of the fine structure in atomic spectroscopy. There it can be made responsible for an elevation of the s-level energy states.

1.2 The Concept of Spin in the Band Structure

In the previous Section, the spin was introduced as a property of electrons that are either free or coupled to an atomic electromagnetic field. This concept shall now be transferred to electrons in the periodic potential of crystals. In the following, it is shown that the high symmetry of crystal lattices can be harnessed to develop the theory of the band structure. The band structure reveals the energy dispersion of electrons in a crystal lattice as shown exemplarily in Fig. 1.1 for a bulk GaAs semiconductor. A brief overview of band theory and possible methods of band calculation is followed by a more specific discussion of III/V and II/VI semiconductors which represent the material class investigated in the present thesis. The chapter concludes with the particularities of optical injection and orientation of spin polarization within the band structure.

1.2.1 Band Structure of Semiconductors

It is a defining characteristic of semiconductors that the Fermi energy E_{F} is positioned within a band gap between the conduction (lowest unoccupied band) and valence band (highest occupied band) at low temperatures. Subsequently, electrons can be transitioned from the valence to the conduction band by the help of photons, providing the required energy. This optical excitation process depends on the involved bands, motivating the calculation of the band structure with the help of Bloch's theorem [71].

The Bloch theorem is based on a potential $U(\boldsymbol{r})=U(\boldsymbol{r}+\boldsymbol{R})$ that follows the periodicity of the crystal for all vectors $\boldsymbol{R}$ of the direct lattice. From this theorem it can be concluded that the electron eigenstates with quantum number n take the shape of Bloch waves

$$\Psi_{\boldsymbol{k},\mathrm{n}}(\boldsymbol{r}) = e^{i\boldsymbol{kr}} u_{\boldsymbol{k},\mathrm{n}}(\boldsymbol{r}) \tag{1.12}$$

where $\boldsymbol{k}$ is the wave vector of a plane wave which is multiplied with the Bloch function $u_{\boldsymbol{k},\mathrm{n}}$. This Bloch function reflects the impact of the lattice periodicity on the electron eigenstates via $u_{\boldsymbol{k},\mathrm{n}}(\boldsymbol{r}) = u_{\boldsymbol{k},\mathrm{n}}(\boldsymbol{r} + \boldsymbol{R})$. The resulting energy eigenvalues feature an equivalent periodicity in reciprocal space where $E_\mathrm{n}(\boldsymbol{k}) = E_\mathrm{n}(\boldsymbol{k} + \boldsymbol{G})$ for every vector $\boldsymbol{G}$ of the reciprocal lattice. In the one-electron picture this allows for visualizing the resulting arrangement of eigenstates as bands in the energy spectrum separated by gaps for which no stationary eigenstates exist. The dispersion relation $E(k)$ can be displayed in the reduced zone scheme as the absolute wave vector $k = |\boldsymbol{k}|$ can be projected back into the Brillouin zone with $k \leq \pi/a$ where a is the lattice parameter. In order to find an explicit form of $E(k)$ the band structure calculation can be generally performed in two different approaches [72].

The first group of methods is based on the parabolic dispersion relation of free electrons $E(\boldsymbol{k}) = \hbar^2\boldsymbol{k}^2/(2m)$ that is perturbed by the potential $U(\boldsymbol{r})$. As the perturbation is usually assumed to be weak the parabolic dispersion is mostly maintained and only altered at the borders of the Brillouin zone where gaps in the dispersion are formed. These gaps can be explained phenomenologically from destructive interference of the electron wave function, impinging on the periodic potential. This first group of methods which includes for example the nearly free electron (NFE) model and the pseudo potential (PP) model is applied foremost to conduction band states where electrons can be treated as delocalized[§] [74; 75].

The second group of methods which is more applicable for valence band calculations follows from the idea that due to the proximity of atoms in the crystal lattice their individual atomic orbitals are hybridizing. The wave function overlap in the linear combination of orbitals is hereby treated as an perturbation. Since the level spacing in the resulting high dimensional eigenfrequency spectrum is extremely small it can be viewed as a continuous band. For methods that make use of this approach, as for instance the tight binding model (TB) or linear combination of atomic orbitals (LCAO), a mathematically stringent discussion can be found in literature [72; 76; 77]. In this thesis, the origin of electronic bands is introduced more qualitatively, making use of basic group theory concepts by adapting the formalism of [72; 78] for the abstract group theory of crystals. The irreducible group representations and the corresponding multiplication tables are taken from [79].

Both semiconductors, GaAs as well as CdTe, crystallize in the zincblende structure depicted in Fig. 1.1 (a). Following the Schönflies notation the tetrahedral T_d point group describes all symmetry operations for the zincblende lattice that keep at least one point fixed. This knowledge about the lattice symmetry can be used to reduce the complexity of describing the system. This is the case since all symmetry operations from the point group must not

---

[§] A further candidate from this group is the Kronig-Penney model which is without use for realistic band structure calculation but represents a simple and analytically solvable approach often used for educational purpose [73].

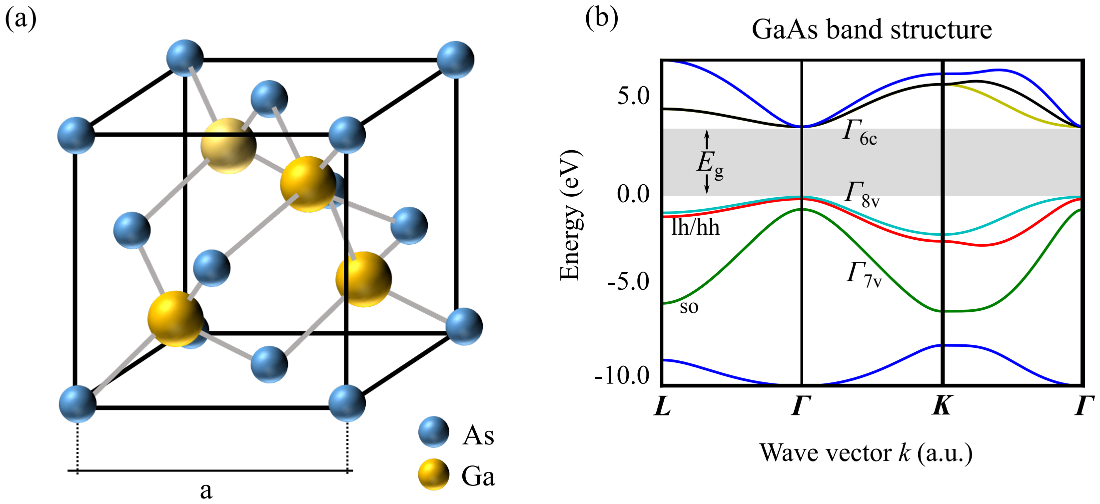

Fig. 1.1: **(a)** Schematic zincblende crystal structure without center of inversion assembled from Ga (yellow) and As (blue) atoms adapted from [80]. **(b)** Band structure calculation in the reduced k-space for bulk GaAs adapted from [81]. The direct band gap of the semiconductor can be found at the Γ-point.

change the Hamiltonian of the system in accordance with Noether's theorem [82]. Hamiltonians of n-dimensional systems take the form of $n \times n$-matrices which can be written as a linear combination of basis matrices described by the irreducible representation Γ_i[¶]. In this context, the irreducible representation can be understood as $n \times n$-matrices which fulfill the corresponding multiplication table of the group with the standard matrix multiplication. Moreover, this irreducible representation links the Hamiltonian to a set of basis functions with corresponding symmetry, representing suitable wave functions for the conduction and valence band at the Γ-point ($k = 0$).

Coming back to the evolution of the band structure, it is shown in Fig. 1.2 that the covalent bonds, formed by the valence electrons of atoms in III/V and II/VI compounds, result in an electronic configuration that stems from p ($l = 1$) and s ($l = 0$) orbitals. Hybridization leads to the molecule-like formation of antibonding and bonding orbitals that are energetically blue and red shifted respectively. The s and p orbitals are described by the spherical symmetries D_0^+ and D_1^- in the full rotation group representation where the subscript is the angular momentum quantum number and the exponent indicates the parity. Through the direct product $\otimes$ the representation of the individual orbital is combined with the symmetry group for spins given by $D_{\frac{1}{2}}^+$. In the next step, the crystal field symmetry is integrated by transferring the spherical symmetry groups to the specific irreducible Γ_i representation of the T_d group. In a last step, the result of the direct product is calculated (using the multiplication table in [79]). The entire

---

[¶] As an example: The basis matrices of the two-dimensional spin space are given by the Pauli matrices $(\boldsymbol{\sigma}_\mathrm{x}, \boldsymbol{\sigma}_\mathrm{y}, \boldsymbol{\sigma}_\mathrm{z})$ and $\boldsymbol{\sigma}^2$ which transform in accordance with the symmetry of the irreducible representation Γ_4 and Γ_1 respectively.

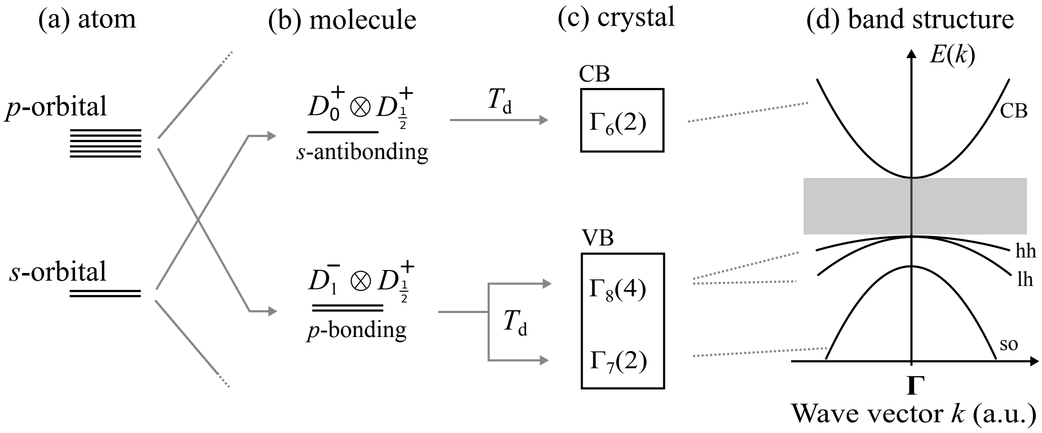

Fig. 1.2: Schematic band evolution from individual atomic orbitals **(a)** to the band structure **(c-d)** via molecule-like hybridization **(b)** in zincblende semiconductors partly adapted from [83]. In accordance with the group theory based symmetry concept of Eq. (1.13), the representation of the orbitals is transferred to the irreducible representation of the T_d point group which is given by the zincblende crystal. Subsequently, these bands are visualized as a schematic band structure in proximity to the Γ-point, similar to the band calculation in Fig. 1.1 (b).

deduction results in

$$\text{conduction band:} \quad D_0^+ \otimes D_{\frac{1}{2}}^+ \xrightarrow{T_\mathrm{d}} \Gamma_1(1) \otimes \Gamma_6(2) = \Gamma_6(2) \tag{1.13}$$

$$\text{valence band:} \quad D_1^- \otimes D_{\frac{1}{2}}^+ \xrightarrow{T_\mathrm{d}} \Gamma_5(3) \otimes \Gamma_6(2) = \Gamma_7(2) + \Gamma_8(4) \tag{1.14}$$

where the integer in parenthesis is the degeneracy level of the represented band.

Finally, the obtained symmetry representation can be linked with their basis functions to characterize the resulting bands with the help of the good quantum number $j = l + s$. The conduction band originates from s-orbitals such that the total angular momentum j takes the value 1/2 since $l = 0$, resulting in twofold spin degenerate states $|j, m_\mathrm{j}\rangle$ as $m_\mathrm{j} = \pm 1/2$. These states $|1/2, \pm 1/2\rangle$ can be understood as the basis functions of $\Gamma_6(2)$. In a similar manner the fourfold degenerate $\Gamma_8(4)$ together with the twofold $\Gamma_7(2)$ representations are identified as the in total sixfold degenerate valence band. Within the valence band the Γ_7 band is separated from the remaining Γ_8 band by an energy Δ_SO which arises from a SO contribution. Furthermore, the basis functions of $\Gamma_8(4)$ are given by $|3/2, \pm 1/2\rangle$ and $|3/2, \pm 3/2\rangle$, taking into account the p-type origin of the bands with $j = 1 + 1/2 = 3/2$. The schematic band structure diagram in the vicinity of the Γ-point in Fig. 1.2 reveals a split of $\Gamma_8(4)$ into two subbands for non-zero values of k. These subbands are the so-called heavy-hole (hh) band for $m_\mathrm{j} = \pm 3/2$ and light-hole (lh) band for $m_\mathrm{j} = \pm 1/2$. This splitting is explained by the link of band curvature and effective mass by the tensor $(m^{*-1})_\mathrm{ij} = \hbar^{-2} \partial E(\boldsymbol{k}) / (\partial k_\mathrm{i} \partial k_\mathrm{j})$.

The introduced concept for the origin of bands can as well be applied to two-dimensional semiconductor structures grown in [001] orientation like the investigated QW samples in this thesis. Analogous to Eq. (1.15) the irreducible band representation for QWs is found from the $D_{2\mathrm{d}}$ point group, taking into account the reduction of symmetry compared to the bulk.

Considering the changed compatibility of the full rotation group with $D_{2\mathrm{d}}$ and the respective multiplication table for this point group the irreducible representation

$$\text{valence band:} \quad D_1^- \otimes D^+_{\frac{1}{2}} \quad \xrightarrow{D_{2\mathrm{d}}} \quad [\Gamma_4(1) + \Gamma_5(2)] \otimes \Gamma_6(2) = \Gamma_7(2) + \Gamma_6(2) + \Gamma_7(2) \tag{1.15}$$

is found for the QW valence band.

By comparison of the QW valence band with Eq. (1.13) it can be seen that for the split-off band Γ_7 the degeneracy of hh and lh, priorly given by a single Γ_8 in the bulk, is now lifted in two separate subbands in the QW. These levels can be identified as twofold degenerate hh and lh bands with Γ_6 and Γ_7 symmetry respectively. This effect is caused by the spatial confinement enforced on the wave function, adding an additional confinement energy E_{con} to the dispersion. Quantum confinement effects arise from the Heisenberg principle of uncertainty that limits the precision of determining the position Δz and the momentum Δp_{z} for one particle simultaneously. This is quantified by $\Delta p_{\mathrm{z}} \sim \hbar/\Delta z$ [83]. Without loss of generality it is concluded that a restriction of the electrons along the growth direction $z \parallel [001]$ leads to the confinement energy $E_{\mathrm{con}} = (\Delta p_{\mathrm{z}})^2/2m^*$. Generally, E_{con} becomes important when it approaches the thermal energy in the system given by $k_{\mathrm{B}}T/2$ where k_{B} is the Boltzmann constant. In GaAs at cryogenic helium temperatures ($\approx 4\,\mathrm{K}$) this case emerges for the confinement $\Delta z \leq 70\,\mathrm{nm}$ if an effective electron mass of $0.066\,m$ is considered. Accordingly, the dependence of E_{con} on the particle mass explains the observed energy difference of the hh and lh band, since a ratio of $m^*_{\mathrm{hh}}/m^*_{\mathrm{lh}} \approx 6.71$ is found in GaAs.

1.2.2 Optical Spin Injection and Orientation

The dynamics of spin polarization, injected due to coherent optical excitation processes, stands at the core of this work. Therefore, an understanding of optical transitions based on light matter interaction in the band structure regime is essential.

Interband absorption describes the creation of electron hole pairs by photon mediated transitions from the valence to the conduction band. Quantum mechanically the probability of such processes is described by the transition rate from an initial eigenstate $|i\rangle$ of the system into a final one $|f\rangle$. This transition is quantified by Fermi's golden rule

$$W_{\mathrm{i}\to\mathrm{f}} = \frac{2\pi}{\hbar}|\langle f|H'|i\rangle|^2\rho(\hbar\omega) \tag{1.16}$$

where $\rho(\hbar\omega)$ is the density of final states and $\hbar\omega$ the energy difference in between the states given by the angular frequency ω [83; 84]. The semi-classical framework allows for the interpretation of the photon as an electromagnetic wave which acts on the system as a perturbation that is quantified by the matrix element $|\langle f|H'|i\rangle|$. If an electron in an electromagnetic field is considered (cf. (1.9) without the relativistic corrections) the obtained Hamiltonian can be separated into $H = H_0 + H'$ with $H_0 = \hat{\boldsymbol{p}}/(2m) + V(\boldsymbol{r})$ for the potential energy $V(\boldsymbol{r})$ and the perturbation Hamiltonian $H' = e\boldsymbol{r} \cdot \boldsymbol{\mathcal{E}_0}$. The latter one is equivalent to the dipole exchange energy in an electric field with strength $\boldsymbol{\mathcal{E}}_0$ and is therefore known as the electric dipole ap-

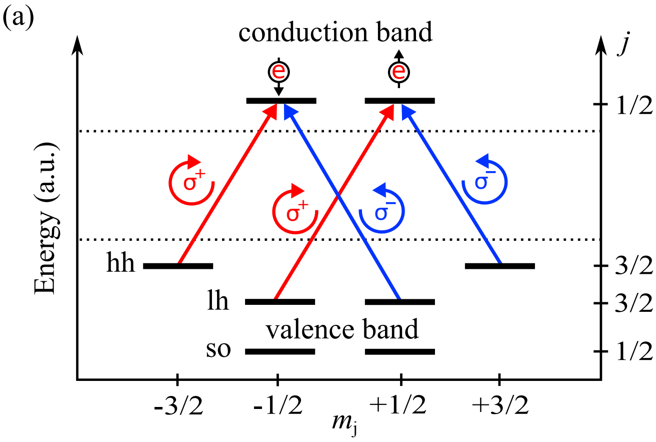

(b) Dipole selection rules

quantum number	allowed transition
j	$\Delta j = \pm 1$
m_j	$\Delta m_j = 0, \pm 1$
l	$\Delta l = \pm 1$
m_l	$\Delta m_l = 0, \pm 1$
s	$\Delta s = 0$
m_s	$\Delta m_s = 0$

Fig. 1.3: (a) Schematic visualization of the eigenstate spectrum in the band structure of III/V and II/VI semiconductor QWs. The states in the conduction and valence band are energetically separated by the band gap and labeled with corresponding quantum numbers. The degeneracy of valence band states is partly lifted due to spin-orbit coupling (split-off band) or as a result of confinement (lh- and hh-band). The selection rules for optically excited transitions are indicated by red (blued) arrows which represent excitation with σ^+ (σ^-) polarized light. **(b)** Table of selection rules for dipole allowed transitions given for a selection of quantum numbers.

proximation. A full mathematical derivation of this perturbation Hamiltonian can be found in [83] [‖]. Subsequently, the matrix element

$$|\langle f|H'|i\rangle| = |\langle f|e\boldsymbol{r}\cdot\boldsymbol{\mathcal{E}}_0|i\rangle| \tag{1.17}$$

can be calculated if the initial and final states are known. This enables the formulation of selection rules for the electric dipole that must be obeyed to get a non-zero result for Eq. (1.17). In the band structure the selection rules determine how the quantum numbers can change due to transitions. A selection of such rules is depicted in Fig. 1.3. Instead of calculating the transition rate for each combination of quantum numbers a more direct approach can be made by harnessing again the symmetry of the bands. However, this method reveals only whether the matrix element is zero or non-zero which is sufficient for the definition of selection rules but does not replace an exact calculation. Group theoretical considerations yield that a Hamilton with irreducible representation Γ_{H} determines the matrix element to be

$$\langle f|H'|i\rangle = \begin{cases} \neq 0 & \text{if}\,\Gamma_{\mathrm{f}}\,\text{is contained in}\,\Gamma_{\mathrm{i}}\otimes\Gamma_{\mathrm{H}}, \\ \neq 0 & \text{if}\,\Gamma_{1}\,\text{is contained in}\,\Gamma_{\mathrm{f}}\otimes\Gamma_{\mathrm{H}}\otimes\Gamma_{\mathrm{i}}, \\ = 0 & \text{otherwise,} \end{cases} \tag{1.18}$$

[‖] By neglecting $\boldsymbol{A}^2$ terms related to weak two-photon absorption and choosing the Coulomb gauge $\nabla\cdot\boldsymbol{A}(t) = 0$ for the vector potential the expression $H' = \frac{e}{m}\boldsymbol{p}\cdot\boldsymbol{A}$ is found. Furthermore, in good approximation $\boldsymbol{A}(t) = \boldsymbol{A}_0 \exp \pm i(\boldsymbol{k}\cdot\boldsymbol{r} - \omega t) \approx \boldsymbol{A}_0$ is assumed since $\boldsymbol{k}\cdot\boldsymbol{r} \ll 1$ terms can be neglected in a Taylor expansion for the visible wavelength spectrum and atomic dimensions. With the electric field strength $\boldsymbol{\mathcal{E}}_0 = i\omega\boldsymbol{A}_0$ this simplification yields H'. Mathematically this transition is justified by employing the Von-Neumann equation for time-dependent operators $\hat{\boldsymbol{O}}$ given by $\mathrm{d}\hat{\boldsymbol{O}}/\mathrm{d}t = i\hbar^{-1}\left[H_0, \hat{\boldsymbol{O}}\right]$ to $\hat{\boldsymbol{p}} = m\mathrm{d}r/\mathrm{d}t$. This allows to write $\langle f|\hat{\boldsymbol{p}}|i\rangle = im\omega\langle f|\hat{\boldsymbol{r}}|i\rangle$ since $\omega = E_{\mathrm{f}} - E_{\mathrm{i}}$ denotes the energy gap in between the initial and final state.

if Γ_i denotes the symmetry of the state $|i\rangle$ and Γ_f of the state $|f\rangle$ [72]. It is known that the dipole exchange Hamiltonian in T_d and $D_{2\mathrm{d}}$ is represented by Γ_5 if the light is polarized perpendicular to the growth direction [72]. The irreducible representations of the involved bands were introduced in the previous section (cf. Fig. 1.1) and thus the selection rules in Fig. 1.3 can be determined with the help of the multiplication table found in [79]. This set of rules can be extended if higher order terms like quadrupole moments of the electric or magnetic field are introduced to the perturbation Hamiltonian H'. However for the physics presented in this work such an extension is not necessary.

The schematic representation of a QW band structure in Fig. 1.3 (a) visualizes the possible optically driven transitions in agreement with the dipole selection rules. Here, it is assumed that photons are carrying angular momentum of either $+\hbar$ or $-\hbar$ projected on the axis of propagation. Light of such polarization is accordingly referred to as σ^+ or σ^- polarized while linear polarization is an equally strong combination of both. As a direct result, σ^+ (σ^-) triggers transitions with a change of $\Delta m_\mathrm{j} = 1$ ($\Delta m_\mathrm{j} = -1$) compliant with the conservation of angular momentum. In general, it can be seen in Fig. (1.3) (a) that a certain kind of circular polarization always triggers two of the possible transitions at once. This suggests an equal excitation of electrons with spin up and down into the conduction band, prohibiting the creation of a net spin polarization. However, Eq. (1.17) can be employed to show that the hh transitions $|3/2, \pm 1/2\rangle \rightarrow |1/2, \pm 1/2\rangle$ are three times more likely than the lh equivalent [83; 85]. As a consequence, it is indeed possible to induce a non-zero spin polarization with defined orientation by using circular polarized light of one kind. This ability is even more enhanced in QW structures as the degeneracy of hh and lh is lifted, allowing to drive the individual transitions by tuning the photon energy to the respective levels. Moreover, the simultaneous orientation of spins in the hole states can be neglected as it is randomized on short time scales by the same strong SO coupling effect which separates lh and hh bands from the split-off band [83].

1.3 Spin Dynamics and Phenomena

The initial Sections 1.1 and 1.2 serve as a fundamental introduction of the spin and its quantum mechanical nature integrated into the framework of semiconductor band structures. Motivated by the field of spintronics the following section deals with phenomena related to the spin itself and the electrons carrying it. In particular, this outline is supposed to enable a better understanding of the space- and time-resolved spin experiments of this thesis which are embedded in fundamental principles of spintronics [86; 87]. In order to organize this overview, the spatial and temporal degrees of freedom in a spin polarized 2DEG are discussed separately. Firstly, particle drift and diffusion are introduced and secondly relaxation dynamics of spin coherence are discussed. Afterwards, the relativistic phenomenon of SO coupling, established with the Dirac equation in Eq. (1.10), is extended to the regime of semiconductor heterostructures. From the resulting combination of spatiotemporal spin dynamics and SO coupling arises a peculiar spin texture in QWs. This spin texture is the so called persistent spin helix and its theoretical description marks the conclusion of the theoretical background.

1.3.1 Spatial Dynamics - Drift and Diffusion

Due to the implantation of electron donors into a semiconductor the Fermi energy E_F can be lifted from within the band gap into the conduction band, creating a Fermi sea of delocalized electrons. The resulting system can be described as a quasi-free two-dimensional electron gas (2DEG). For moderate densities and temperatures not equal to zero, the electrons in the gas scatter elastically with each other and thus perform a random walk in the sense of Brownian motion. In accordance with the Drude model [88] and the relaxation time approximation, the electrons propagate freely in between two scattering events [89; 90]. This uniform propagation is described by the mean free path l_p which is traveled during the flight time τ, leading to a particle velocity $v = l_\mathrm{p}/\tau$. The subsequent scattering redirects the particle velocity stochastically, giving rise to the random walk mentioned above. In lattices such electron scattering occurs mainly due to other electrons, impurities, phonons or the interfaces of the QW. In the case of a non-equilibrium density distribution $n(\boldsymbol{r}, t)$, the resulting random walk will statistically lead to a net motion of electrons from regions of higher concentration towards such with lower concentration. This spreading of particles is known as diffusion. In a steady state, the diffusive flux along the gradient of concentration is described by Fick's first law $\boldsymbol{J} = -D_\mathrm{e}\nabla \cdot n(\boldsymbol{r}, t)$ and will eventually equilibrate the concentration. The proportionality factor D_e is the electron diffusion coefficient which represents a measure for how fast the density distribution approaches its equilibrium state.

Following [91], the diffusion coefficient can be derived from a simplified random walk model by considering only one spatial dimension x and an unchangeable number of electrons $N_0 = \int_{-\infty}^{+\infty} n(x,t)\,\mathrm{d}x$. In this model, time and space are described by discrete steps of t_p and l_p respectively. Consequently, the electron density at position x and time t is determined by the densities at positions $x \pm l_\mathrm{p}$ in the previous time step $t - \tau$, reading

$$n(x,t) = p_+ n(x + l_\mathrm{p}, t - \tau) + p_- n(x - l_\mathrm{p}, t - \tau) \tag{1.19}$$

where p_+ (p_+) is the probability for an electron to move in positive (negative) direction. For a real random walk the probabilities are balanced and $p_+ = p_- = 1/2$. However, an applied external electric field can impose an imbalance $\Delta p = p_+ - p_-$. Due to a Taylor expansion of Eq. (1.19) around (x,t) the density can be rewritten as

$$n(x,t) = n(x,t) - l_\mathrm{p}\Delta p \frac{\partial n(x,t)}{\partial x} + \frac{1}{2} l_\mathrm{p}^2 \frac{\partial^2 n(x,t)}{\partial x^2} - \tau \frac{\partial n(x,t)}{\partial t} + \mathcal{O}(l^2) + \mathcal{O}(\tau) \tag{1.20}$$

in first order of τ and second order of l. Remarkably, the expression takes the form of Fick's second law if $\Delta p = 0$, yielding

$$\frac{\partial n(x,t)}{\partial t} = D_\mathrm{e} \frac{\partial^2 n(x,t)}{\partial x^2} \tag{1.21}$$

if the diffusion coefficient is written as

$$D_\mathrm{e} = l_\mathrm{p}^2/(2\tau) = \tau v^2/2 \tag{1.22}$$

which is the correct form for two-dimensional diffusion [**].

Electrons are fermions and therefore indistinguishable. This has to be taken into account for the occupation probability of 2DEG states by quantum-compatible statistics. The Fermi-Dirac statistic for low temperatures ($k_\mathrm{B}T \ll E_\mathrm{F}$) is determined by Pauli blocking of states below the Fermi energy where the 2DEG is degenerate. However, if the temperature is raised the degeneracy of the 2DEG is lifted and the Fermi-Dirac statistic evolves into the Boltzmann statistic. This two regimes have a distinct impact on the diffusion behavior of the 2DEG and will, therefore, be discussed separately.

(i) The Fermi-Dirac distribution allows only electrons close to the Fermi energy to contribute in scattering events. This is because, in scattering events the electron must transition from an initial to a final state as the electron momentum is changed. This requirement limits scattering to states in a small band around E_F where unoccupied and allowed states exist due to a smearing out of the Fermi-Dirac statistic for non-zero temperature. For higher energies than E_F no allowed states exist and electron states with less energy are Pauli blocked. As a result, the relevant velocity for electron diffusion in a degenerate 2DEG is the Fermi velocity $v_\mathrm{F} = \sqrt{2E_\mathrm{F}/m^*}$. Additionally, this limitation of contributing states to the vicinity of the Fermi edge results in a dominance of elastic scattering events for which the electron energy is conserved. For this reason, it can be concluded that the dominant scattering time τ_ee is given by elastic electron-electron scattering events within the 2DEG and thus the diffusion coefficient is written as $D_\mathrm{e} = l_\mathrm{p}^2/(2\tau_\mathrm{ee}) = \tau_\mathrm{ee} v_\mathrm{F}^2/2$. **(ii)** An increase of the temperature in the 2DEG is accompanied by a smearing out of the Fermi edge and eventually the Fermi-Dirac statistic is transitioned into the Boltzmann statistic. The Boltzmann statistic predicts a non-zero occupation probability for states above E_F and the emergence of unoccupied states for energies below E_F. Consequently, the relevant electron velocity for D_e is an averaged velocity $\langle v^2 \rangle$ with a strong temperature dependence, stemming from the Boltzmann statistic.

For the non-degenerate regime a different form of the diffusion coefficient is given by the Einstein relation $D_\mathrm{e} = \mu k_\mathrm{B} T$, linking diffusion with mobility. The mobility $\mu = -v_\mathrm{dr}/\mathcal{E}$ relates an applied electric field $\mathcal{E} = |\boldsymbol{\mathcal{E}}|$ with the drift velocity v_dr of the accelerated electrons. Within the Drude model, this velocity limitation is caused by inelastic scattering events which generate an energetic equilibrium by the dissipation of energy from the 2DEG into the lattice. Accordingly, the fluctuation-dissipation theorem can be used to derive the Einstein relation provided a parabolic dispersion [74; 93]. In order for the Einstein relation to be valid, the inelastic scattering τ_p must play the dominating role in the general scattering rate $\tau^{-1} =$

[**] In this model the time evolution of the random walk in discrete steps is somewhat simplified. A more sophisticated theory is based on the Boltzmann transport equation and can be found in [89; 92]. This approach yields $D_\mathrm{e} = \tau v^2/3$ with a slightly different yet more correct prefactor 1/3 for one dimensional diffusion. However, 1/2 is by coincidence the correct prefactor for two-dimensional diffusion and the model above can be used in its present shape for 2DEG diffusion.

$\tau_\mathrm{p}^{-1} + \tau_\mathrm{ee}^{-1}$ that determines the diffusion coefficient [94]. The momentum relaxation time τ_p is, on the other hand, related to the mobility by $\mu_\mathrm{e} = e\tau_\mathrm{p}/m^*$, explaining the relation of diffusion and mobility. However, the samples studied in the present thesis exhibit a very high mobility and thus a long momentum relaxation time compared with the electron-electron scattering time, making the Einstein relation inapplicable.

The majority of results presented in this work are related to the dynamics of the macroscopic spin polarization injected into a 2DEG. In such a system, the spatial dynamics of the spin ensemble stem from the electrons that carry the spin. As a result, the diffusion of spin polarization can be explained by employing the description of particle transport and the electron diffusion coefficient. Beyond this simplification, a diffusion that does not arise from a density gradient but a gradient in the spin polarization has to be considered. This motivates the introduction of a spin diffusion coefficient D_s that is relying only on the scattering of electrons with opposite spin polarization. In this work the notation D_s is used to describe spin and electron diffusion in combination. This combination is assumed to be dominated by the electron diffusion which is known to be higher than the pure spin diffusion by an order of magnitude [91].

1.3.2 Temporal Dynamics - Spin Relaxation

As with any physical system that is not in equilibrium, a once excited spin polarization relaxes back into a state of balance. The relevant timescale for this process is defined by the spin lifetime after which the observable polarization has decreased by the factor e^{-1}. Hence, this lifetime is used to characterize a spin polarization that consists of a coherently excited ensemble of individual electron spins.

Depending on the extraction method, the term spin lifetime may refer to processes of different origin and must therefore be further specified. In the absence of external magnetic fields, the general disappearance of an initial spin polarization is characterized by the intrinsic lifetime T_s. If an additional magnetic field is introduced to the spin ensemble the lifetime parallel and perpendicular to this quantization axis has to be discussed individually [95]. (i) The longitudinal spin lifetime T_1 describes the relaxation of the spin polarization projected on the quantization axis. This decay arises from spin flips which change the electron state from $|\uparrow\rangle$ to $|\downarrow\rangle$ (or vice versa) up to the point where there is no net polarization any more. Due to the Zeeman splitting, imposed by a magnetic field, spin flip processes require the dissipation of energy realized for example through the emission of phonons. (ii) The experiments conducted within the present work are exclusively performed in Voigt geometry. In this alignment, the spin polarization perpendicular to the applied magnetic field is monitored. As a direct consequence, the observed decay is characterized by the transversal spin lifetime T_2 which is also referred to as dephasing time. This time scale is determined by the coherence of the spin precession around the magnetic field observed as oscillation of the measured spin projection and denoted as spin beats.

The intrinsic (T_s) as wells as the precession phase (T_2) coherence of ensemble spins is generally destroyed by fluctuating magnetic fields. These momentum-dependent fields arise from SO coupling and cause an inhomogeneous distribution of precession frequencies among the individual spins, resulting in decoherence. Fluctuating fields are characterized by their correlation time τ_c during which the field can be considered constant before it changes its direction and strength. By further elaborating this background the Dyakonov-Perel (DP) mechanism is introduced as the dominant origin of spin relaxation in zincblende semiconductor heterostructures with reduced dimensionality [96; 97]. Reviving the random walk model from Section 1.3.1, a constant momentum can be assumed in between to events of scattering and thus the scattering time τ makes a good guess for the correlation time of the fluctuating field. If the precession frequency caused by B_so is given by ω_so the squared precession angle, accumulated during the time of flight, is $(\omega_\mathrm{so}\tau)^2$. Hence, the total squared precession angle after some time t is given by $(\omega_\mathrm{so}\tau)^2(t/\tau)$. As a first approximation the lifetime T_s represents the time for which the squared precession angle approaches a value of one, resulting in the expression

$$T_\mathrm{s} \sim \frac{1}{\omega_\mathrm{so}^2\tau} \tag{1.23}$$

which allows for an estimation of the lifetime. This relation is derived from the idea that a series of arbitrarily directed rotations averages out, if the angle of precession for each individual rotation is small. For a distinct lifetime quantification Eq. (1.23) might have little importance, however, as a trend it can be concluded that a decreased scattering time τ enhances the spin lifetime.

Other mechanisms of spin relaxation are rather minute in the investigated GaAs and CdTe QWs but shall be briefly mentioned for the purpose of completeness [96; 97]. The Elliot-Yafet mechanism is a consequence of strong SO-splitting in the valence band. In this case, a wave function admixture from the valence band to the conduction band causes electron scattering accompanied by spin-flips. The Bir-Aronov-Pikus mechanism is pronounced in p-doped structures where electron-hole scattering leads to spin relaxation. Further processes arise from exchange interaction or a coupling of spins with the nuclei of the lattice.

1.3.3 Spatiotemporal Dynamics - Spin Diffusion Equation

When it comes to monitoring a 2DEG spin ensemble the above introduced dynamics in space and time can clearly not be treated independently but have to be seen as a conjunct process. Thus, in the two-dimensional case (x- and y-axis) the phenomena of drift, diffusion and relaxation are joint in the drift-diffusion equation for the spin polarization $s(x, y, t)$ projected on the z-axis. This equation is given by

$$\frac{\partial s}{\partial t} = \underbrace{D_\mathrm{s}\frac{\partial^2 s}{\partial \boldsymbol{r}^2} + \mu_\mathrm{e}\mathcal{E}\frac{\partial s}{\partial \boldsymbol{r}}}_{J_\mathrm{s}} - \frac{s}{\tau} \tag{1.24}$$

where $\boldsymbol{r} = (x, y)$ denotes the position vector and the first two terms on the right side are often times referred to as spin current J_s while the last term represents an exponential relaxation of s [91]. The differential equation (1.24) shows the necessity to evaluate a possible influence of J_s on the extraction of the spin decay time τ from a measured $s(x, y, t)$, even in the absence of electric fields ($\mathcal{E} = 0$). According measurements are often based on monitoring an exponential-like decrease of the spin polarization signal with proceeding time after the initial orientation. In such measurements the extracted decay time can be additionally influenced by spatial dynamics when spins diffuse out of the experimentally monitored area. In pump-probe experiments (cf. 2.2) this influence can be estimated by a comparison of the laser spot size on the sample and the diffusion length $L_\mathrm{s} = \sqrt{D_\mathrm{s} T_\mathrm{s}}$. The diffusion length is a measure for the average distance that a spin travels during the spin lifetime. A reasonable description of systems with significant diffusive contributions can be achieved by solving Eq. (1.24), assuming a Gaussian like excitation $s(x, y, 0) = s_0 \exp[-4\ln(2)(x^2 + y^2)^2/w_0]$ as initial condition. The obtained solution is given by

$$s(x, y, t) = s_0 \underbrace{\pi \ln(2) \left[\frac{w_0}{w(t)}\right]^2 e^{-4\ln(2)(x^2+y^2)/w^2(t)}}_{\text{diffusive broadening}} \cdot \underbrace{e^{-t/T_\mathrm{s}}}_{\text{relaxation}} \tag{1.25}$$

where the full width at half maximum (FWHM) of the Gaussian spatial distribution $w(t)$ can be written down in squared form as

$$w^2(t) = w_0^2 + 16\ln(2) D_\mathrm{s} t, \tag{1.26}$$

exhibiting a linear dependence on time [91]. The first term of Eq. (1.25) can be understood as a distribution of the spin ensemble in space and over time, preserving the entire spin population. Only the second contribution reassembles a real relaxation process which eventually leads to a vanishing of measurable spin polarization.

1.3.4 Rashba and Dresselhaus Spin-Orbit Coupling

As a by-product the Dirac equation predicts a coupling of the spin magnetic moment with the angular momentum denoted as spin-orbit coupling. This effect is important for the understanding of the spectral fine structure in atomic spectroscopy and the appearance of the split-off band as shown in Fig. 1.4 (a). In the Dirac equation the SO term is described by an effective magnetic field, adding a Zeeman-like contribution $-\boldsymbol{B}_\mathrm{so} \cdot \boldsymbol{\mu}_\mathrm{s}$ to the Hamiltonian. Regarding individual atoms, this contribution takes the form $\frac{a}{\hbar^2} \boldsymbol{L} \cdot \boldsymbol{S}$, depending on the SO coupling constant $a = Ze^2 \mu_0 \hbar/(8\pi m^2 r_\mathrm{B}^3)$ where r_B is the Bohr radius [67]. It is discussed around Eq. (1.11) that the involved effective magnetic fields emerge from a coupling of electron momentum and electric fields. This interpretation is confirmed since $\boldsymbol{L}$ and a represent the electron momentum and the Coulomb central field of the nucleus. Shifting the focus from single atoms to two-dimensional semiconductor heterostructures, two additional mechanisms have to be considered known as Rashba and Dresselhaus SO coupling [39; 40]. Generally, in

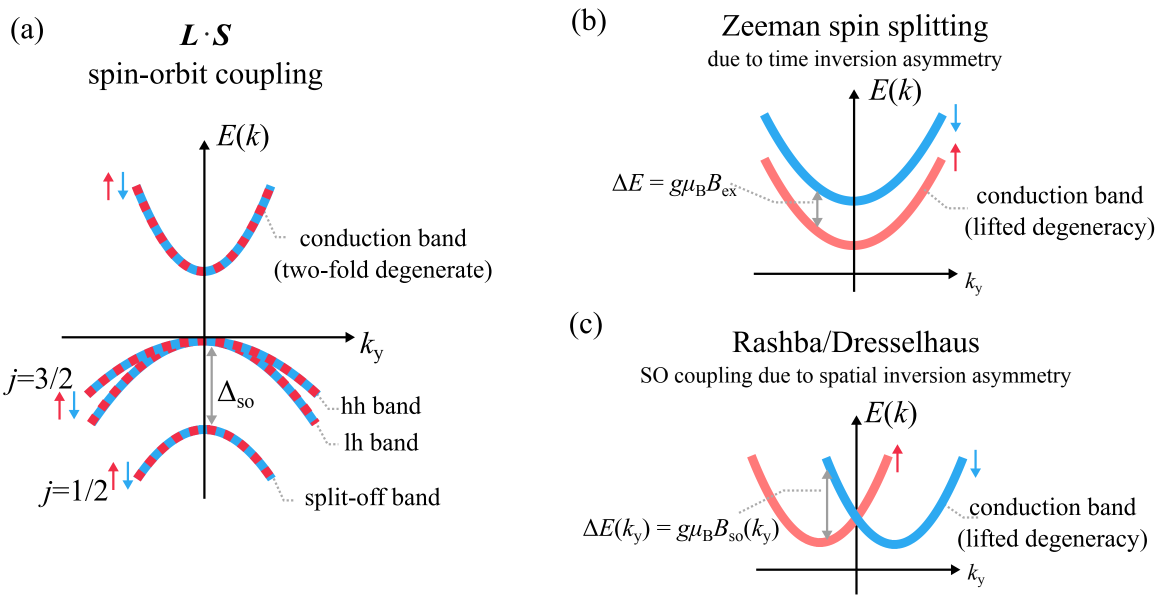

Fig. 1.4: Variants of spin splitting in the band structure. **(a)** According to Kramer's theorem the conduction band as well as the valence band are spin degenerate. The split-off band is vertically shifted due to atomic SO coupling. **(b)** Zeeman splitting due to a broken time inversion symmetry in the presence of external magnetic fields. **(c)** Momentum-dependent spin splitting due to Rashba and Dresselhaus SO coupling.

band structures effective magnetic fields evolve from the coupling of the electron momentum in form of the wave vector $\boldsymbol{k}$ with electric fields that are present due to the crystal nuclei (Dresselhaus) or imposed by an asymmetric heterostructure with a drop of potential across the QW (Rashba). This section is devoted to a detailed overview of these two contributions, as they form the basis not only for the persistent spin helix, but also for a variety of spintronic phenomena [29; 41].

A general approach to SO coupling is based on symmetry considerations and the Kramer's theorem [98; 99]. It is an important feature of effective magnetic fields to maintain time symmetry while this symmetry is generally broken by external magnetic fields. For external magnetic fields $\boldsymbol{B}$ the time reversal operator $\hat{\boldsymbol{T}}$ reverses the sign of these fields $\hat{\boldsymbol{T}}(\boldsymbol{B}) = -\boldsymbol{B}$ since $\boldsymbol{B}$ is generated from electric currents which are reversed if time propagates backwards. The same argument applies to the angular momentum $\boldsymbol{L}$ which is inverted by time-reversal. However, this effect is canceled for effective magnetic fields where two angular momenta appear in combination and thus $\hat{\boldsymbol{T}}(\boldsymbol{B}) = \hat{\boldsymbol{T}}(\boldsymbol{L} \cdot \boldsymbol{S}) = \hat{\boldsymbol{T}}(\boldsymbol{L}) \cdot \hat{\boldsymbol{T}}(\boldsymbol{S}) = \text{-}\boldsymbol{L} \cdot \text{-}\boldsymbol{S} = \boldsymbol{B}$.

For systems with half-integer spin that exhibit time reversal symmetry the Kramer theorem can be applied. This theorem states that in such a regime every eigenstate is at least doubly degenerate (exactly twofold for spin $1/2$). Accordingly, the energy of an electron remains unchanged during time reversal while spin and wave vector flip the sign and hence $E(\boldsymbol{k})_\uparrow = E(-\boldsymbol{k})_\downarrow$ holds for any wave vector of the Brillouin zone. Additionally, it can be shown that $E(\boldsymbol{k})_\uparrow = E(-\boldsymbol{k})_\uparrow$ applies if the system exhibits an inversions center, keeping the lattice unaffected by flipping the lattice vector in real space $\boldsymbol{R} \rightarrow -\boldsymbol{R}$. From the combination of Kramer's theorem with the center of inversion the relation $E(\boldsymbol{k})_{\uparrow} = E(\boldsymbol{k})_{\downarrow}$ is found. This expression shows that the energy for spin up and down states with the same wave vector are equal, being often times referred to as Kramer's degeneracy. This statement is in contradiction with the Zeeman-like spin splitting generated from effective magnetic fields. Therefore, the class of systems in which spin splitting of the conduction and valence bands can be observed in the absence of external magnetic fields is restricted to lattices without a center of inversion. This requirement is met, among other materials, in GaAs and CdTe zincblende structures which belong to the T_{d} point group. Here, the total six-fold degeneracy of the $\Gamma_6(2)$ and $\Gamma_8(4)$ band is lifted for all wave vectors away from the Γ-point.

For QWs grown along the [001] high symmetry direction the Dresselhaus and Rashba SO couplings are discussed consecutively in the subsequent paragraphs, following the formalism of [48; 97] by choosing the coordinate system $x \parallel [1\bar{1}0]$ and $y \parallel [110]$ for convenience.

Dresselhaus spin-orbit coupling

The Hamiltonian that describes the Dresselhaus contribution to the effective conduction band structure arises from bulk inversion asymmetry (BIA) in the crystal and takes the form

$$H_{\mathrm{BIA}} = \gamma_{\mathrm{D}} \left[\sigma_{\mathrm{x}} k_{\mathrm{x}}(k_{\mathrm{y}}^2 - k_{\mathrm{z}}^2) + \sigma_{\mathrm{y}} k_{\mathrm{y}}(k_{\mathrm{z}}^2 - k_{\mathrm{x}}^2) + \sigma_{\mathrm{z}} k_{\mathrm{z}}(k_{\mathrm{x}}^2 - k_{\mathrm{y}}^2)\right] \tag{1.27}$$

where γ_{D} is the material-dependent bulk Dresselhaus parameter. For a QW confined along the z-direction the expectation value $\langle k_{\mathrm{z}} \rangle = 0$ is zero[††] for the out-of-plane component. On the contrary, the in-plane components can be conveniently written in polar coordinates $\boldsymbol{k} = k[\cos(\theta), \sin(\theta)]$ where θ is the angle between the wave vector and the x-axis. As a result, the Hamiltonian in Eq. (1.27) takes the form

$$H_{\mathrm{BIA}} = \beta k \left[\sigma_{\mathrm{y}} \sin(\theta) - \sigma_{\mathrm{x}} \cos(\theta)\right] + \beta_3 k \left[\sigma_{\mathrm{x}} \cos(3\theta) - \sigma_{\mathrm{y}} \sin(3\theta)\right] \tag{1.28}$$

with the Dresselhaus parameter $\beta = \beta_1 - \beta_3$ which combines

$$\beta_1 = \gamma_{\mathrm{D}} \langle k_{\mathrm{z}}^2 \rangle \qquad \text{and} \qquad \beta_3 = \gamma_{\mathrm{D}} \frac{k^2}{4} \tag{1.29}$$

where k can be replaced by the Fermi wave vector if the Fermi-Dirac statistic is applicable. In first approximation and in accordance with literature the higher angular harmonics are neglected for the beginning as they are cubic contributions of k [48; 51]. This approximation enables a simplification of Eq. (1.28) where the second term is neglected and the remaining Hamiltonian reads

$$H'_{\mathrm{BIA}} = \beta k \left[\sigma_{\mathrm{y}} \sin(\theta) - \sigma_{\mathrm{x}} \cos(\theta)\right] \tag{1.30}$$

[††] Assuming a sufficiently narrow QW and cryogenic temperatures it is reasonable to restrict calculations for the growth direction to the lowest conduction subband $e1$ such that $\langle k_{\mathrm{z}}^2 \rangle = \int \langle e1 | \boldsymbol{k}_{\mathrm{z}}^2 | e1 \rangle$ [97]. The symbol $\boldsymbol{k}_{\mathrm{z}} = -\mathrm{i}d/dz$ denotes the wave vector operator.

with a linear dependence on k.

Rashba spin-orbit coupling

The SIA term arises from structural inversion asymmetry (SIA) of the confining potential. The Rashba SO coupling Hamiltonian is given by

$$H_{\mathrm{SIA}} = \alpha(\sigma_{\mathrm{x}} k_{\mathrm{y}} - \sigma_{\mathrm{y}} k_{\mathrm{x}}) \tag{1.31}$$

if the electric field $\mathcal{E}_{\mathrm{QW}}$, which stems from the confining potential, is applied along the z-direction. The Rashba parameter $\alpha = \gamma_{\mathrm{R}} \mathcal{E}_{\mathrm{QW}}$ is calculated from the external or built-in electric field in the QW and the material specific Rashba coupling parameter γ_{R}. The latter can be derived by perturbation theory from the effective band structure, using the Löwdin partitioning technique [97; 100]. With this approach a value of $5.206\,e\text{Å}^2$ is found for the Γ_6 conduction band in GaAs and $6.930\,e\text{Å}^2$ in CdTe [100].

Aiming at a more practical understanding of Rashba and Dresselhaus SO coupling, the combined Hamiltonian $H_{\mathrm{SIA}} + H_{\mathrm{BIA}}$ is compared with the original SO Hamiltonian $H_{\mathrm{so}} = -\frac{\mu_{\mathrm{B}}}{2} \boldsymbol{\sigma} \cdot \boldsymbol{B}_{\mathrm{so}}$. Due to this comparison a definition of the combined Rashba and Dresselhaus induced effective magnetic field is found as

$$\boldsymbol{B}_{\mathrm{so}}(\boldsymbol{k}) = \frac{2}{g\mu_{\mathrm{B}}} \begin{bmatrix} \left(\alpha + \beta_1 + 2\beta_3 \frac{k_{\mathrm{x}}^2 - k_{\mathrm{y}}^2}{k^2}\right) k_{\mathrm{y}} \\ \left(\beta_1 - \alpha - 2\beta_3 \frac{k_{\mathrm{x}}^2 - k_{\mathrm{y}}^2}{k^2}\right) k_{\mathrm{x}} \end{bmatrix} \tag{1.32}$$

if the coordinate system $x \parallel [1\bar{1}0]$ and $y \parallel [110]$ is chosen. This combination includes k-linear terms proportional to β_1 (linear Dresselhaus parameter) and k-cubic terms proportional to β_3 (cubic Dresselhaus parameter). The cubic and linear notation related to the Dresselhaus parameter is commonly seen in literature but might be confusing at first glance as neither β_1 nor β_3 itself exhibit cubic or linear contributions in k. Remarkably, the momentum-dependent effective magnetic field is anisotropic in k-space. This is crucial for the PSH evolution and it will be a main task of this thesis to investigate how the Rashba and Dresselhaus parameters can be extracted and manipulated by indirectly monitoring $\boldsymbol{B}_{\mathrm{so}}$. With the polar coordinates introduced for the Hamiltonian in Eq. (1.28) the effective field can be separated by splitting off higher harmonics, resulting in

$$\boldsymbol{B}_{\mathrm{so}}(\boldsymbol{k}) = \underbrace{\frac{2k}{g\mu_{\mathrm{B}}} \begin{bmatrix} (\alpha + \beta_1 - \beta_3) \sin(\theta) \\ (-\alpha + \beta_1 - \beta_3) \cos(\theta) \end{bmatrix}}_{\boldsymbol{B}_{\mathrm{so}}^{(1)}} + \underbrace{\frac{2k}{g\mu_{\mathrm{B}}} \begin{bmatrix} \beta_3 \sin(3\theta) \\ -\beta_3 \cos(3\theta) \end{bmatrix}}_{\boldsymbol{B}_{\mathrm{so}}^{(3)}} \tag{1.33}$$

with two effective field components $\boldsymbol{B}_{\mathrm{so}}^{(1)}$ and $\boldsymbol{B}_{\mathrm{so}}^{(3)}$.

For the moment, the third harmonics terms are neglected as they contain cubic k contributions. In the following section which deals with the persistent spin helix it is shown that $\boldsymbol{B}_{\mathrm{so}}^{(3)}$ anyway has solely negligible influence on the PSH evolution. Therefore, the band splitting predicted in the beginning of this section is now underpinned with a dispersion extracted from the SO Hamiltonian

$$H = \frac{\hbar k^2}{2m^*} + H_{\mathrm{SIA}} + H'_{\mathrm{BIA}} \tag{1.34}$$

which combines SO coupling with the usual parabolic dispersion of free electrons. It is derived that this Hamiltonian indeed implies a lifting of the Kramer's degeneracy as predicted earlier. This manifests as a twofold dispersion

$$E_{\uparrow\downarrow}(\boldsymbol{k}) = \frac{\hbar k^2}{2m^*} \pm k\sqrt{\alpha^2 + \beta^2 + 2\alpha\beta \sin(2\theta)} \tag{1.35}$$

which reveals a linear dependence of the spin splitting on an increasing electron momentum and an anisotropy in the case where $\alpha = \beta$ [101].

The dispersion of the conduction band, given by Eq. (1.35), is depicted schematically in Fig. 1.4 (c) where the relation is compared with the dispersion in the degenerate case (a) and in a case where the band exhibits Zeeman splitting (b). The dispersion for Rashba and Dresselhaus SO coupling induced spin splitting implies a lateral shift of the spin up and down band to opposite directions of the wave vector while they maintain a parabolic-like shape. It is noteworthy that the dispersion exhibits an anisotropy in k-space due to the θ dependence in the second term if both α and β are non-zero. The lateral separation of the parabolas indicates the linear increase of the splitting energy with the wave vector and represents a peculiar characteristic of Rashba and Dresselhaus SO coupling. From here, various phenomena such as the spin galvanic effect or the spin hall effect can be deduced [29; 44]. Zeeman induced spin splitting, on the contrary, leads to spin branches that are vertically separated as depicted in (b) and predicted by Kramer's theorem. The vertical shift represents a constant splitting energy which is not momentum-dependent. In 1.4 (a) the band structure is shown in the absence of external magnetic fields and without Rashba and Dresselhaus SO coupling. In this case, the conduction band as well as the valence band are spin degenerate. However, spin-orbit coupling on the atomic level plays an important role for the energetic separation of the split-off band from the hh and lh band. This is explained by the coupling of the total angular momentum j to the spin, resulting in a different SO contribution for the split-off band ($j = 1/2$) than for the hole bands ($j = 3/2$).

1.3.5 The Persistent Spin Helix

The last section of this chapter brings together the previously introduced spin dynamics in space and time with Rashba and Dresselhaus SO coupling mechanisms in order to characterize the persistent spin helix.

The persistent spin helix evolves in two-dimensional heterostructures made from a crystal that lacks a center of inversion. It appears as a unidirectional wave of electron spin polarization under the specific condition that the Rashba and Dresselhaus parameters are equal in strength ($\alpha = \beta$). An optical injected electron distribution in the 2DEG results in an isotropic k-space occupation closely around the Γ-point, leading to diffusion as described in Section 1.3.1. Using the polarization of the optical pulse, this locally injected distribution can be spin polarized as explained in Section 1.2.2. Consequently, a coupling of the coherent spin polarization to the effective magnetic fields which arise from non-zero k-values during diffusion is observed. Thus, the diffusing spins undergo precession while they spread in the QW. Remarkably, each electron sees a series of individual effective magnetic fields in dependence on its individual diffusion path. Nevertheless, the overall spin coherence is maintained in the special regime of the PSH (cf. figure 1.5 (b)). This manifests in the characteristic spin texture which emerges due to the combined precession and diffusion. From this observation the question is raised of how the spin coherence is stabilized, although, every spin is affected by different effective magnetic fields during its random walk.

For a thorough understanding of the spin helix pattern, the effective magnetic field $\boldsymbol{B}_{\mathrm{so}}$ in Eq. (1.33) has to be examined carefully. Firstly, the regime of $\alpha = \beta_1 - \beta_3$ will cause the y-component of the $\boldsymbol{B}_{\mathrm{so}}^{(1)}$ vector to disappear, yielding a SU(2) symmetry in the k-space distribution of the SO field. As a consequence, only a momentum along the y-axis will result in precession while a propagation along the x-axis does not create any effective magnetic field and thus leaves the spin unaffected. A schematic distribution of the effective magnetic field in k-space is depicted in Fig. 1.5 (a-d) for different combinations of α and β. While the effective magnetic fields for pure Rashba SO coupling is isotropic (b), a purely Dresselhaus induced field exhibits a less ordered distribution (a). Only in the perfectly balanced regime the field along the k_{x}-axis is entirely gone (c) while a mixed regime with $\beta/\alpha = 0.45$ results in a slightly distorted yet still recognizable SU(2) symmetry (d).

Next to the $\boldsymbol{B}_{\mathrm{so}}^{(1)}$ distribution, the precession around the $\boldsymbol{B}_{\mathrm{so}}^{(3)}$ contribution has to be elucidated further to evaluate its impact on the PSH. This is realized by calculating the cross-correlations $\langle B_{\mathrm{so,x}} k_{\mathrm{y}} \rangle$ and $\langle B_{\mathrm{so,y}} k_{\mathrm{x}} \rangle$ from which it can be deduced whether an accumulated precession angle of all possible paths in an isotropic random walk averages out or results in a net spin polarization. In summary, it is found that only the $\boldsymbol{B}_{\mathrm{so}}^{(1)}$ term generates the precession responsible for the PSH[‡‡]. Furthermore, it is shown that the additional velocity component, induced by an externally applied electric field, can change the spatial dynamics in such a way that the $\boldsymbol{B}_{\mathrm{so}}^{(3)}$ component cannot be neglected anymore. However, this case occurs only if the drift velocity approaches the Fermi velocity which requires significant electric field strength and therefore $\boldsymbol{B}_{\mathrm{so}}^{(3)}$ is neglected in this thesis unless stated otherwise. Due to the linear dependence of the remaining effective magnetic field on k the spin coherence is maintained regardless of the individual spin precession. Moreover, independent on the individual spin orientation in time, the polarization at every position in the QW plane is fixed. This spatially fixed polarization is detected as a unidirectional wave patter with a spatial wavelength along the y-axis. Figure 1.5 (e) shows a schematic distribution of electron spins within the PSH pattern and the according appearance in a false-color map where the colors red and blue

---

[‡‡] Reviving the notation $k_{\mathrm{y}} = k \sin\theta$, $k_{\mathrm{x}} = k \cos\theta$ and the effective field given in Eq. (1.33). The cross-correlations can be reduced to integrals of the type $\int_0^{2\pi} \sin(\theta)^2 \mathrm{d}\theta \neq 0$ for $\boldsymbol{B}_{\mathrm{so}}^{(1)}$ and $\int_0^{2\pi} sin(\theta) sin(3\theta) \mathrm{d}\theta = 0$ for $\boldsymbol{B}_{\mathrm{so}}^{(3)}$ [48].

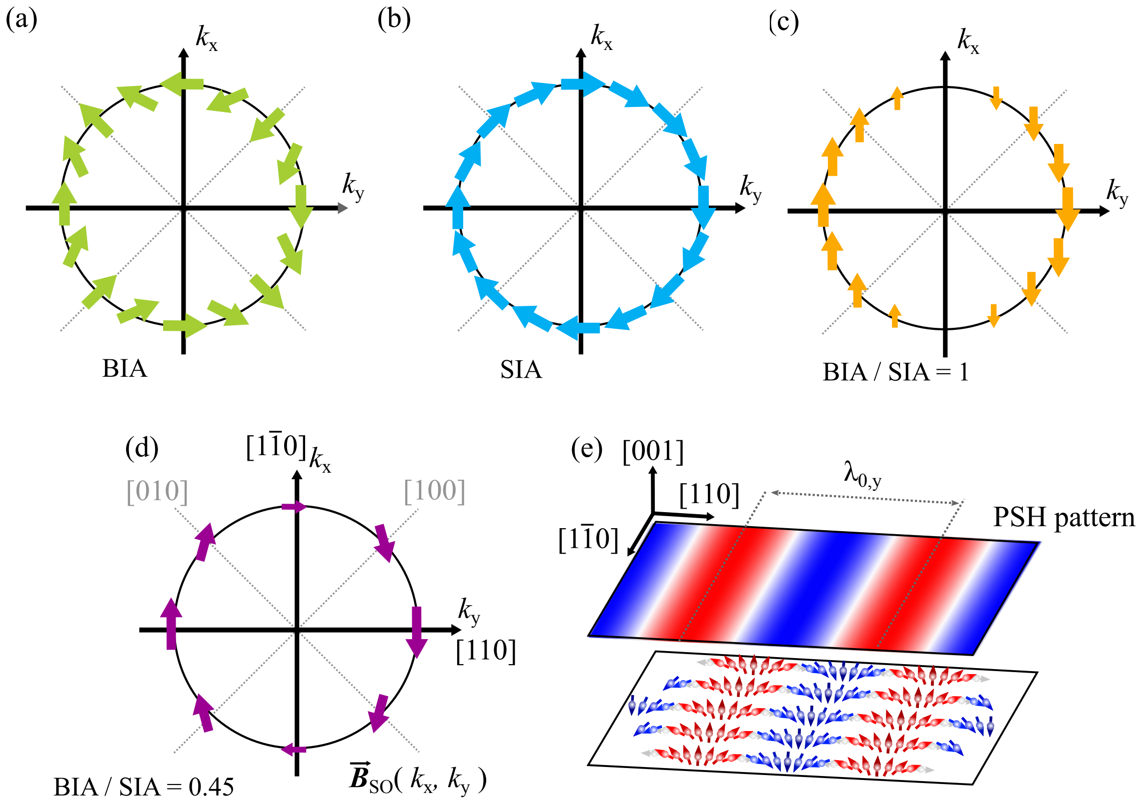

Fig. 1.5: Schematic distribution of B_{so} in k-space, showing orientation and magnitude of the effective field on the Fermi circle. **(a-d)** The plots reassemble pure Dresselhaus SO coupling (a), pure Rashba SO coupling (b) and ratios of BIA/SIA= 1 (c) as well as BIA/SIA= 0.45 (d). **(e)** Appearance of the PSH as unidirectional spin wave indicated by colored arrows (bottom layer). False-color representation of the spin orientation in a two dimensional map (top layer), adaped in part from [48].

resemble the two opposite orientations of the polarization. The spatial precession length $\lambda_{0,\mathrm{y}}$ can be experimentally determined and allows for the extraction of the Rashba and Dresselhaus parameters from the measurement. The precession length $\lambda_{0,\mathrm{y}}$ can be quantified by merging the basic relation $\omega = 2\pi v/\lambda_{0,\mathrm{y}}$ with the electron velocity $v_{\mathrm{y}} = \hbar k_{\mathrm{y}}/m^*$ into the equation for the Larmor frequency

$$\hbar\omega = g\mu_{\mathrm{B}} B_{\mathrm{so,x}} \quad \Rightarrow \quad \lambda_{0,\mathrm{y}} = \frac{\pi\hbar^2}{m^*}(\alpha+\beta)^{-1}, \tag{1.36}$$

resulting in a fixed relation of $\lambda_{0,\mathrm{y}}$ and $(\alpha+\beta)$.

Another important consequence of the SU(2) k-space symmetry for the balanced Rashba and Dresselhaus regime is a significant enhancement of the spin-lifetime [47; 102]. In Section 1.3.2, the Dyaknonv-Perel (DP) mechanism is introduced as the dominant spin relaxation mechanism based on fluctuating effective magnetic fields [101]. This mechanism is suppressed in the PSH regime where the SU(2) symmetry prevents locally detected electrons spins from having an accumulated precession phase difference. This remains valid even when the spins travel on completely different pathways towards the point of detection. Due to the symmetry of the effective field distribution the randomization of spins is avoided, leading to $T_\mathrm{s} \to \infty$. Nevertheless, infinite lifetimes can only be obtained in a perfect PSH regime and if $\boldsymbol{B}_\mathrm{so}^{(3)}$ is neglected. While the cubic terms are usually not contributing to the PSH they still have influence, acting as the remaining fluctuating field in the sense of the DP mechanism. This allows to predict the lifetime of the PSH as

$$(T_\mathrm{s})^{-1} = \frac{2D_\mathrm{s}(m^*)^2}{\hbar^4}\left[3\beta_3^2 + (\alpha - \beta_1 + \beta_3)^2\right] \tag{1.37}$$

where other decay mechanisms than DP are not taken into account. Interestingly, this lifetime can only be achieved if the initially excited width of the spin polarization is spatially smaller than λ_0, since otherwise the evolution of a structured spin texture is disabled.

Chapter 2

Experimental Techniques

Subsequent to the theoretical background, this overview of experimental aspects serves as a link between the abstract theoretical predictions in Chapter 1 and the measured results in Chapter 3. Here, the main focus is on the experimental techniques and the ultrafast spectroscopy setup used to uncover the persistent spin helix and to manipulate its unique properties. The chapter is completed by a discussion of the investigated heterostructure samples and their features. Establishing a first set of sample properties, including Fermi energy, mobility and sheet density, allows for the prediction of the resulting PSH parameters and their tunability.

The PSH is a phenomenon which appears as a texture of spin polarization that evolves simultaneously in time and space. Therefore, it is a central requirement to develop a threefold experimental approach that allows for the detection of spin polarization in a time- and space-resolved fashion. (i) The theoretical background already elaborated on the fact that light is an advantageous tool for the creation and orientation of coherent spin polarization in semiconductor samples. Furthermore, the interaction of polarized light and matter is a mutual process which can be harnessed not only to manipulate but also to sense the electronic state and the spin polarization in solids. One especially useful effect is the magneto-optic Kerr rotation which transfers information about the macroscopic sample magnetization into the polarization axis of a linearly polarized light beam. This enables an optical read out of the spin polarization from which the macroscopic magnetization originated. (ii) Moreover, this effect is integrated into a pump-probe approach which adds temporal resolution on picosecond timescales to the experiment. (iii) Finally, the optical spectroscopy with ultrashort laser pulses is carried out with a spatially displaceable pump beam spot on the sample surface, resulting in the desired spatial resolution.

2.1 The Magneto-Optic Kerr Effect

As the first evidence for the interaction of light and magnetization, the Faraday effect describes a rotating polarization plane of a linearly polarized, monochromatic light beam which propagates through a transparent medium exposed to an external magnetic field [103; 104]. Faraday could further show a linear dependence of the rotation angle on the applied field strength. An

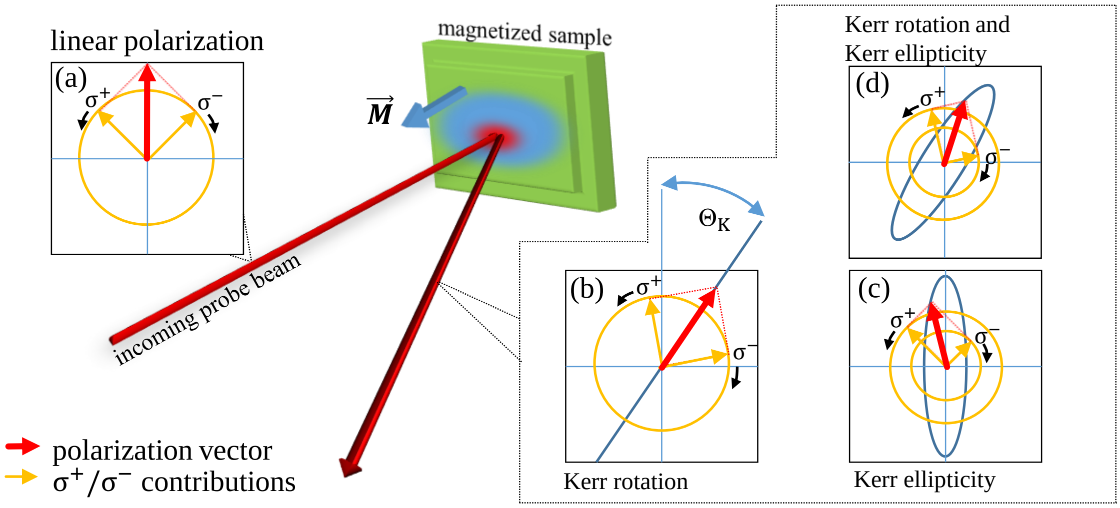

Fig. 2.1: Magneto-optic Kerr Effect in a magnetized sample partly adapted from [106]. **(a)** The incoming probe beam features a linear polarization (red arrow) assembled from equally strong right and left circular contributions (orange arrows and circles). **(b)** Reflected polarization in the case of pure Kerr rotation with maintained linear polarization, however, rotated by Θ_{K} due to circular birefringence. **(c)** Appearance of Kerr ellipticity due to circular dichroism, resulting in unbalanced σ^+/σ^- amplitudes indicated by orange circles with different diameter. **(d)** Combination of Kerr rotation and ellipticity with tilted main axis of the elliptic polarization.

equivalent effect was observed in reflection geometry by Kerr and is, therefore, referred to as magneto-optic Kerr effect (MOKE) schematically depicted in Fig. 2.1 [104; 105]. Following the approach of [106], the role of the external magnetic field can be taken over by any macroscopic magnetization $\boldsymbol{M}$ within the sample, e.g., by a coherent orientation of magnetic spin moments μ_{s}. The resulting interaction of magnetization and the electromagnetic light wave is described by Maxwell's equations. From this interaction the following discussion covers a brief derivation of the spectral dependence of the Kerr rotation (KR) angle Θ_{K} in spectral vicinity to a two-state resonance. This regime is then used as a model for the detection of electron spin polarization in the conduction band of semiconductors.

The MOKE relies on a medium which mediates the interaction of magnetic field and light. In such a medium the Maxwell equations in matter must be applied and the usually small effect of the permeability tensor $\boldsymbol{\mu}(\omega) \approx \mu_0 \mathbf{1}_3$ is neglected where μ_0 is the vacuum permeability. Thus, only the dielectric permittivity tensor $\boldsymbol{\epsilon}(\omega)$ remains for the light-matter interaction, representing a proportionality factor between electric displacement vector and field $\boldsymbol{D} = \epsilon_0 \boldsymbol{\epsilon}(\omega) \cdot \boldsymbol{\mathcal{E}}$ where ϵ_0 is the vacuum permittivity. If the magnetization and the propagation direction of the light is oriented along the z-axis, $\boldsymbol{\epsilon}$ becomes an asymmetric tensor with complex components ϵ_{ij}, reading

$$\boldsymbol{\epsilon}(\omega, \boldsymbol{M}) = \begin{pmatrix} \epsilon_{\mathrm{xx}} & \epsilon_{\mathrm{xy}} & 0 \\ -\epsilon_{\mathrm{xy}} & \epsilon_{\mathrm{yy}} & 0 \\ 0 & 0 & \epsilon_{\mathrm{zz}} \end{pmatrix} \qquad \text{with} \qquad \epsilon_{\mathrm{ij}} = \epsilon'_{\mathrm{ij}} + i\, \epsilon''_{\mathrm{ij}} \tag{2.1}$$

if the medium is otherwise isotropic. From inserting Eq. (2.1) into the general electromagnetic, differential wave equation it is possible to obtain two normal modes of the light wave as solutions which are identified as σ^+ and σ^- polarized lights. Remarkably, from the same wave equation these modes can be shown to obey a different complex refractive index $N_\pm^2 = \epsilon_{\mathrm{xx}} \pm i\,\epsilon_{\mathrm{xy}}$ where $+$ $(-)$ indicates the refractive index for σ^+ (σ^-) polarization. From Fresnel's formulas it is known that a difference in the refractive index will result in different complex reflection coefficients given by $r_\pm = (N_\pm - 1)/(N_\pm + 1)$. The complex reflection coefficient determines the amplitude and phase change for a reflected wave compared to the incident one. Consequently, amplitude and phase changes will not be equivalent for right and left circular light waves that are reflected on a magnetized sample. This is because, $r_+ \neq r_-$ manifests either as circular birefringence for a phase difference, as a circular dichroism for an amplitude difference or as a combination of both. All three cases are visualized in Fig. 2.1 (b-d). This figure shows the σ^+/σ^- constituents of a linear polarization before and after the reflection from a magnetized sample. After the reflection the light beam will have undergone Kerr rotation and exhibit Kerr ellipticity as shown in Fig 2.1 (d). The former one refers to a rotated plane of polarization, resulting from a phase difference of the two reflected circular polarized waves (Kerr rotation). The latter one describes the emergence of an elliptical polarization (Kerr ellipticity) in the case where the amplitudes of the two circular components are unbalanced after the reflection. The angle of Kerr rotation (KR) Θ_{K} as well as the ratio of major and minor axis η_{K} in the elliptical polarization is quantified from the off-diagonal elements of the permittivity tensor (2.1), reading

$$\Theta_{\mathrm{K}} = -\frac{\epsilon'_{\mathrm{xy}}}{n(n^2-1)} \qquad \text{and} \qquad \eta_{\mathrm{K}} = -\frac{\epsilon''_{\mathrm{xy}}}{n(n^2-1)} \tag{2.2}$$

where $n = [\Re(N_+) + \Re(N_-)]/2$ is the averaged real part of the refractive indices $N_\pm$. As the real and the imaginary part of $\boldsymbol{\epsilon}$ can be expected to scale linearly with the magnetization the Kerr rotation and ellipticity are reasonable measures for $\boldsymbol{M}$ and thus for the related spin polarization.

Since the experiments within this work are based on the detection of Θ_{K} this entity shall be discussed in more detail. In particular, the expression in Eq. (2.2) suggests that more detailed knowledge of ϵ'_{xy} is required in order to understand the spectral dependence of Θ_{K} around an optical resonance. Here, an isolated energy level with transition energy $\hbar\omega_0$ from the ground level $|0\rangle$ acts as a toy-model for the resonance. Spin degeneracy is assumed to be lifted, implying two sub-levels $|1\rangle$ and $|2\rangle$. The energy splitting Δ of the spin up and down sub-levels is assumed to be small compared to the transition energy. Recalling the selection rules from Section 1.2.2, the $|1\rangle$ and $|2\rangle$ states are accessible from $|0\rangle$ only with left or right circular light respectively. This corresponds to the phenomenological approach of circular dichroism, being responsible for the MOKE. Furthermore, the Kubo formalism which is not further discussed here but can be found in literature [106; 107] allows for the derivation of the expression

$$\epsilon'_{\mathrm{xy}} = Cf_{12}\Delta \cdot f'(\omega_0) \quad \text{with} \quad f'(x) = \frac{\partial}{\partial x}\left[\frac{2\gamma_{\mathrm{hw}} x^2}{(x^2 - \omega^2 + \gamma_{\mathrm{hw}}^2)^2 + (2\omega\gamma_{\mathrm{hw}})^2}\right] \tag{2.3}$$

that enables to calculate Θ_{K} in dependence on the angular light frequency ω. For this purpose, it has to be assumed that both sub-levels have the same transition strength f_{12}. Additionally, γ_{hw} is the spectral half-width of the transition and basically related to the lifetime of the excited state by Heisenberg's uncertainty. The line shape of Eq. 2.3 is shown in inset Fig. 2.2 (c) where it is visible that the KR has to be measured with the probe tuned slightly away from the resonance frequency where the signal is zero. Furthermore, the direction of rotation and therefore the sign of Θ_{K} has an opposite sign for frequencies below and above the resonance respectively.

2.2 The Kerr Rotation Microscope Setup

Having introduced the MOKE as highly advantageous for the extraction of spin information from semiconductor 2DEGs, this section describes an experimental setup for measurements of Kerr rotation in a time and space resolved fashion.

Generally, by employing a pulsed laser source it is possible to make use of coherent ultrashort light pulses to achieve a temporal resolution in the picosecond time domain with the pump-probe technique. For this method, the output of a pulsed coherent light source is split into two separated pulse trains referred to as the pump and the probe beam. Subsequently, the pump and probe are recombined on the sample. Here, the probe is influenced by changes in the reflection $\mathrm{d}R$ caused by the pump beam. Such changes can, e.g., arise through a variation of the material permittivity, due to an elevated Fermi energy or a coherent magnetization generated by injected spins [108]. Afterwards, the probe beam is finally separated from the pump and directed in a detection scheme which extracts $\mathrm{d}R$ as signal. This detection is often supported by lock-in amplifiers that are fed with a frequency that is used to modulate the influence of the pump beam on the probe. Lock-in amplifiers allow for the detection of the transient reflection $\mathrm{d}R/R$, benefiting from a significantly improved signal to noise ratio. Since the time between two pulses (laser repetition rate: kHz - MHz) is usually long compared to the length of the pulses (fs - ps) the probe pulses can be set to arrive before the pump pulse at the sample. The delay time t_{d} can be realized by a mechanical stage which is placed in one of the two beam paths, allowing for a detuning of the path length from the laser to the sample. The obtained difference in the travel time of pulses enables the detection of a time-resolved signal $\mathrm{d}R/R(t_{\mathrm{d}})$ in dependence on the delay time in between the excitation via the pulse and the detection via the probe.

The experimental setup utilized for the present work combines the MOKE with a pump-probe scheme in a so-called Kerr rotation microscope which is depicted schematically in Fig. 2.1 (a). Within this scheme the output of a mode-locked, femtosecond Ti-sapphire laser with 60 MHz repetition rate is used to provide the pump and probe pulse trains. For spectrally

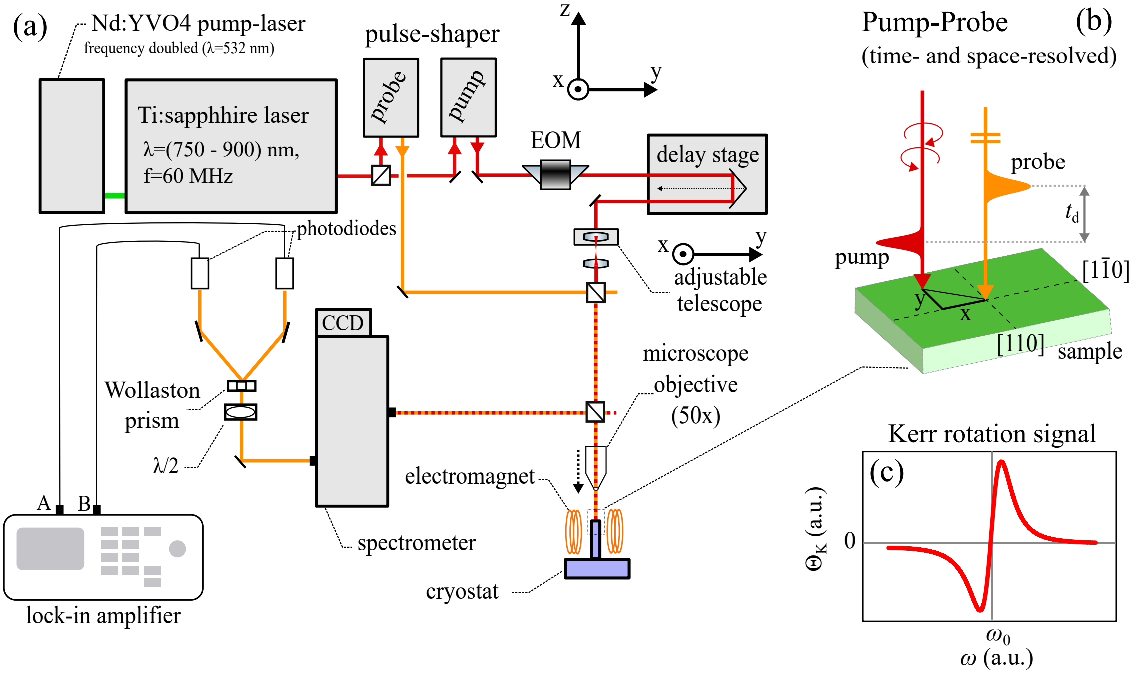

Fig. 2.2: (a) Scheme of the non-degenerate Kerr rotation microscope employed as a pump-probe experiment, allowing for spin sensitive measurements with spatial and temporal resolution. The pump (probe) is indicated by the color orange (light red). **(b)** Magnified visualization of the spatial resolution realized on the sample surface where the pump beam can be laterally shifted on the xy-plane. Temporal delay in between two pulses of pump and probe is schematically indicated. **(c)** Spectral dependence of the Kerr rotation around a resonance ω_0 in accordance with Eq. (2.3).

resolved measurements each pulse train is send through a grating-based 4f-pulse-shaper where the pump and probe are individually cut out from the spectrally broad output $(750-950)$ nm of the mode-locked laser [109]. After the non-degenerate wavelength selection for the pump and probe respectively, the temporal resolution of the system is ~ 1 ps, limited by the chosen spectral width of ~ 0.7 nm. Further, the pump train is send through a mechanical delay stage and its polarization state is modulated between σ^+ and σ^- helicities, using an electro-optical modulator (EOM) (QioptiqLM 0202P). The probe is set to linear polarization. In order to record spatially resolved spin dynamics, the pump arm is complemented by a controllable telescope scheme. Lateral motion of the second lens in this telescope enables movement of the pump spot along the x- and y- direction relative to the probe position (cf. Fig. 2.2 (b)). Afterwards, both beams are collinearly focused onto the sample, using a 50× objective (Mitutoyo M-Plan APO NIR) which provides a focused spot size for the probe (pump) beam of $1\,(3)\ \mu$m. In order to minimize spatial fluctuations the sample is nested in a stabilized helium flow cryostat (Oxford Microstat HiRes2) and cooled to ~ 3.5 K. Such cryogenic temperatures suppress phonon scattering as a possible dephasing mechanism and thus help to conserve the coherence within the spin-ensemble. Being installed in Voigt geometry, an electromagnet positioned around the sample provides variable magnetic fields up to 230 mT.

The reflected, non-degenerate pump and probe pulse trains pass through a spectrometer (Oxford Shamrock 500i) adjusted to the probe beam wavelength where the pump beam is filtered out. The subsequent detection of KR is based on a Wollaston prism which splits the probe train into two beams with perpendicular linear polarization. These two beams are detected independently by two photodiodes, converting the KR into an electrical signal. In this standard, balanced detection scheme the difference signal of both diodes is read out by a lock-in amplifier. Detecting a difference signal effectively reduces noise that originates from fluctuations of the laser power. In this way, the probe signal can be set to zero with the help of a polarization rotating $\lambda/2$-plate in front of the Wollaston prism if the pump beam is temporally blocked. Subsequently, the KR signal due to the magnetization generated by the pump pulse, is detected as a deviation from zero signal. This is due to the fact that a rotation of the linear polarization unbalances the detection scheme.

Remarkably, the detected KR signal depends on the direction of magnetization in the sample. Due to excitation with σ^+ (σ^-) polarized light the spin magnetization becomes oriented parallel (anti-parallel) to the light propagation direction. The direction of magnetization determines the sense of rotation of the KR and thus the detection of negative or positive signal on the lock-in amplifier. Accordingly, the EOM can be used to impose a temporal modulation on the circular polarization direction of the pump and thus the sign of the probe signal. The corresponding modulation frequency can then be passed to the lock-in detection, enabling the measurement of small KR angles up to tens of microradians.

2.3 Sample Characteristics of CdTe and GaAs Quantum Wells

Earlier in this manuscript, it is mentioned that the sample structures investigated in this thesis are semiconductor QWs. The present work about PSH structures is independently conducted in two distinct materials from the III/V and the II/VI group of semiconductors namely in GaAs and CdTe QWs. This twofold material choice is of great scientific interest as it allows for a comparison of the PSH characteristics in GaAs and CdTe. Especially, the latter system has not been intensively studied with regard to the PSH [56; 101].

The III/V and II/VI semiconductor classes are both formed from compounds of element pairs taken from the respective main-groups. Their convenient optical properties, as for instance the possibility for band gap engineering within or close to the visible spectrum, make them highly relevant for technology applications. However, difficulties in achieving high conductivity is a major drawback in particular for II/VI compounds [110]. As a common ground, both crystals are usually grown as zincblende crystals by the molecular beam epitaxy technique. The zincblende structure lacks a center of inversion, making it potentially interesting for the study of SO interaction. For the SO coupling driven PSH a difference in the SO interaction strength is a promising feature for a comparative study of both materials.

In general, the strength of the atomic SO coupling is given by the SO coupling constant $a \propto Z/r_{\mathrm{B}}^3$ where the Bohr radius itself has an inverse proportionality to the atomic number. As a result, the coupling constant can be assumed to scale with the fourth power of the atomic number $a \propto Z^4$ [111]. From this relation a significantly stronger SO coupling behavior is

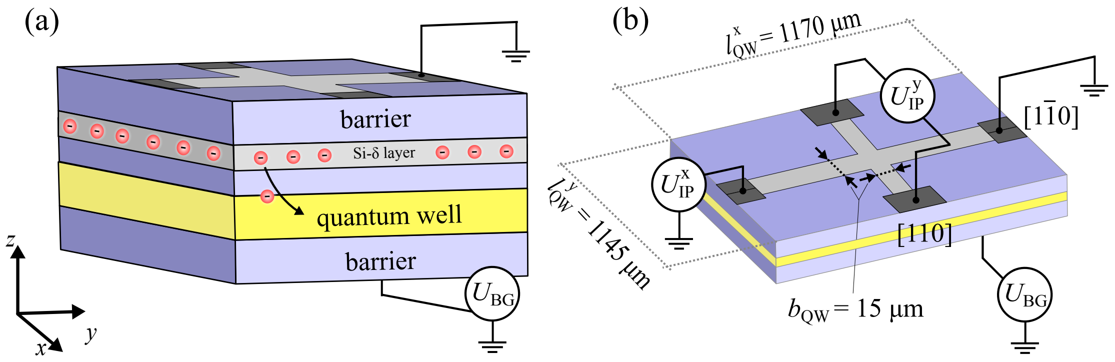

Fig. 2.3: **(a)** Scheme of a quantum well heterostructure in real space. Additional electrons can be transferred from the Si-δ layer into the QW by the application of back gate voltage. **(b)** Schematic diagram to illustrate the possible applications of in-plane and back gate voltages to the Hall bar geometry of the sample.

expected in the CdTe system where the involved atoms are of higher atomic number than in GaAs:

$$Z_{\mathrm{Ga}} = 31 < Z_{\mathrm{As}} = 33 < Z_{\mathrm{Cd}} = 48 < Z_{\mathrm{Te}} = 52$$

The extrinsic Rashba SO coupling mechanism is not directly affected by the involved atoms as it originates from potential gradients imposed by the neighboring layers of the QW. On the contrary, the Dresselhaus SO coupling arises from asymmetrically ordered lattice atoms and is thus influenced by the atomic number. However, this dependence is not equivalent with that of the atomic SO coupling constant but manifests more indirectly via the band structure. A material specific impact becomes present foremost in the Dresselhaus coupling constant γ_D which can be expected to differ noticeably from GaAs to CdTe. This difference is backed by theoretical predictions [112] which take into account the individual band structure of the materials.

Both samples are fabricated as two-dimensional QWs embedded in multilayered heterostructures. The restriction to two dimensions yields a variety of advantages, e.g., a strongly enhanced optical absorption due to an increased oscillator strength of the electron hole pairs [83]. Moreover, QWs enable a higher degree of spin-polarization due to a split of the lh- and hh-bands at the Γ-point (cf. Section 1.2.2) [113]. The term quantum well denotes a spatially narrow sandwich of one material layer with lower band gap in between two layers with elevated band gap. A schematic layer composition is displayed in Fig. 2.3 (a). The spatially modulated potential along the growth direction (z-axis) leaves the electrons in the QW with reduced mobility.

In order to create a 2DEG with free resident carriers it is required to lift the Fermi energy above the conduction band edge, resulting in an occupation of conduction band states in compliance with the Fermi-Dirac statistic. A common approach to achieve such a regime is the incorporation of dopants into the crystal. These dopants act as electron donors which is referred to as n-doping. However, in this case a strongly diminished electron mobility is inevitable due to an enhanced scattering rate of electrons and dopants. This unwanted effect can be avoided by a technique called modulation doping [73]. The explanation of this technique is based on a classical QW with type-I band alignment, featuring two distinct Fermi energies at the interface of the n-doped barrier and the QW layer. In order to satisfy the Poisson equation in the thermodynamic equilibrium the bands at the interface are bent to allow for a continuous transition of the Fermi energies. A migration of electrons from the n-doped barrier material into the QW layer smooths the gap in E_F and enables the formation of a 2DEG in the QW layer. As a consequence, the so formed 2DEG is not affected by scattering with dopants anymore since it is spatially detached from the donors that are located within the barriers. Subsequently to the brief general introduction of quantum well structures, the individual samples used for this thesis will be discussed in more details.

The GaAs quantum well: A $d_\mathrm{QW} = 15\,\mathrm{nm}$ wide layer of GaAs is sandwiched between two barrier layers made from the ternary alloy $\mathrm{Al_{0.33}Ga_{0.67}As}$. The sample was fabricated in the group of G. Yusa*. In the alloy a certain fraction of Ga atoms, given by the subscript of the molecular formula, is replaced by Al atoms. This partial incorporation of Al atoms allows for engineering of the band gap. By tuning the Al content in the alloy the band gap is changed from a value of 1.42 eV in bulk GaAs (0%) towards 2.16 eV in pure AlAs (100%). This tuning is related to a transition from a direct semiconductor to an indirect one when the Al concentration exceeds $\sim 40\,\%$ and the conduction band minimum shifts from the Γ- to the X-point (cf. Fig. 1.1) [73]. At the same time, the lattice constant is only slightly changed and thus GaAs/AlGaAs layer structures can be fabricated almost strain-free, making this material class highly important for science and industry [110]. In this case, the QW is grown on a strongly n-doped GaAs substrate with [001] orientation by molecular beam epitaxy (MBE) which is favored by the aforementioned match of lattice constants.

The QW is modulation doped and exhibits a high electron mobility of $\mu_\mathrm{e} = 2.5\times10^5\,\mathrm{cm^2/Vs}$ determined from magneto-transport measurements at cryogenic temperatures ($\sim 4\,\mathrm{K}$). From the same measurement an electron sheet density of $n_0 = 1.3 \times 10^{11}\,\mathrm{cm^{-2}}$ is found for the 2DEG. Furthermore, the GaAs QW sample is processed into a back gated Hall geometry similar to the drawing in Figure 2.3 (b) which schematically depicts the Ohmic AuGeNi top contacts utilized for the application of voltage. On the one hand, the application of a gate voltage U_BG is a tuning knob for the transverse potential that drops along the QW, enabling a direct manipulation of the Rashba SO coupling via the field $\mathcal{E}_\mathrm{QW}$. On the other hand, the gate voltage can be used to tune the electron density within the QW since it drags electrons from an atomically thin delta layer of silicon (Si-δ) into the QW as visualized in Figure 2.3 (a) . Tuning n_e has a complementary effect on the β_3 Dresselhaus parameter via changes of E_F, however, this alteration can be expected to be small compared with the simultaneously occurring change of α. The highly n-doped Si-δ exhibits an electron concentration of $1.9 \times 10^{11}\,\mathrm{cm^{-2}}$ and is positioned on top of the QW in growth direction. Additionally, in the intersection point of the Hall bar electric drift fields can be generated along the x- ($[1\bar{1}0]$) and y-direction ([110])

---

[*] Department of Physics, Tohoku University, Sendai 980–8578, Japan

Table 2.1: List of sample parameters provided by the groups responsible for the growth or assembled from literature if otherwise indicated. The values for the Dresselhaus parameter are calculated by means of Eq. (1.29).

	d_{QW} (nm)	μ_{e} (cm^2/Vs)	n_0 (cm^{-2})	γ_{D} (eVÅ^3)	m^* (m)	β_1 (meVÅ)	β_3 (meVÅ)
GaAs	15	2.5×10^5	1.3×10^{11}	$(9 - 11)^*$	$0.067^{\dagger}$	4.82	0.22
CdTe	20	4.2×10^5	3.4×10^{11}	$9.10 \pm 0.84^{**}$	0.094^{***}	2.2	0.5

*[48; 54], **[56], ***[116]

by application of the in-plane voltages $U_{\mathrm{IP}}^{\mathrm{x}}$ and $U_{\mathrm{IP}}^{\mathrm{y}}$, according to the wiring in Fig. 2.3 (b). The dimensions of the $b_{\mathrm{QW}} = 15\,\mu$m wide Hall bar are given in the same panel, allowing for the calculation of the applied field by $E_{\mathrm{IP}}^{\mathrm{x/y}} = U_{\mathrm{IP}}^{\mathrm{x/y}}/l_{\mathrm{QW}}$ where l_{QW} denotes the length of the Hall bar arms. For the present sample, an influence of the contact resistance on the in-plane field calculation is neglected. This is because, the total measured resistance in between the Hall bar contacts is $\sim 5\,\mathrm{k}\Omega$ which is much higher than the usual contact resistance of AuGeNi Ohmic contacts in GaAs heterostructures [114].

The CdTe quantum well: This sample consists of a $d_{\mathrm{QW}} = 20\,\mathrm{nm}$ wide CdTe QW embedded in between ternary barriers made of $\mathrm{Cd_{0.74}Mg_{0.26}Te}$. The sample is grown by the group of T. Wojtowicz and G. Karczewski[†] by MBE on a [001] oriented GaAs substrate. The structure exhibits an exceptionally high quality, enabling the observation of the fractional quantum Hall effect [115]. Post growth, digital modulation doping with Iodine far towards the surface prevents donors from migrating into the QW. This warrants a particularly high electron mobility of $\mu_{\mathrm{e}} = 4.2 \times 10^5\,\mathrm{cm^2/Vs}$ and a 2DEG concentration of $n_0 = 3.4 \times 10^{11}\mathrm{cm^{-2}}$ obtained from Hall and conductivity measurements at cryogenic temperatures ($\sim 4\,\mathrm{K}$). Other than the GaAs sample, the present CdTe QW does not have electrical contacts. Therefore, it is neither possible to access the electron density or $\mathcal{E}_{\mathrm{QW}}$ nor to apply drift fields due to the application of voltage. Nevertheless, the results in this thesis show that the electron density n_{e} in the QW is strongly affected by photocarriers that can be optically injected into the conduction band enabled by high absorption.

[†] Institute of Physics, Polish Academy of Science, Aleja Lotników 32/46, PL-02668 Warsaw, Poland

Chapter 3

Experimental Results

The Experimental Results Chapter is designed to provide a review of the experimental findings obtained during the work on this thesis, expanding and completing the results presented in [47; 51; 56]. A main focus is on the SO coupling parameters and their dependences. Experimental measurements are supported by simulations based on the Monte Carlo (MC) method and the drift-diffusion equation respectively. In order to facilitate the access to PSH research, the results are organized in three main parts and an introductory section that covers a characterization of the investigated samples based on photoluminescence (PL).

(i) Initially, the PSH is characterized, reporting on its general appearance which is monitored as spin texture that evolves in space and time. The section examines primarily the measurement configurations employed to visualize the PSH by means of false-color spin polarization micrographs. Subsequently, the PSH is characterized by certain parameters, e.g., wavelength, lifetime and diffusion coefficient. These parameters are linked with the Rashba and Dresselhaus SO coupling, following the models given in the Theoretical Background 1.3.4. (ii) In the next step, the PSH is actively manipulated in order to gain control over the Rashba and Dresselhaus parameters, this is achieved by means of in- and out-of-plane electric fields within the GaAs QW, optical doping of the CdTe QW and the application of in-plane magnetic fields in both structures. Here, a variety of highly interesting tuning knobs is determined and quantified. (iii) Building on the developed understanding of PSH control, the last section of this chapter describes a novel approach towards coherent spin transport in the regime of momentum-dependent SO coupling. The proposed technique is based on a combined application of magnetic and electric fields, tailored precisely to the sample-specific PSH parameters. This regime minimizes the effective fields that arise from SO coupling and thus yields a possibility for polarization conserving spin transport. This peculiar type of spin helix is described for the first time as the so called traveling persistent spin helix (TPSH).

Aiming at an in-depth, comparative study of the persistent spin helix in GaAs and CdTe QWs, the chapter takes a mainly parallel approach. As the PSH emerges generally similar in both materials its characterization is presented for both samples at the same time. For this purpose, the raw data are shown exemplarily only for one material but the individually derived quantitative results are given for both samples respectively. The subsequent section about PSH manipulation is organized in subsections that account for independent tuning mechanisms in the two samples. While in-plane magnetic fields can be applied to both structures, optical doping is limited to the CdTe sample whereas only the GaAs sample allows for an application of electric fields.

3.1 Sample Characterization by Photoluminescence

For the conducted measurements the spin-sensitive MOKE, which is harnessed to extract the spin polarization, is integrated into a non-degenerate pump probe experiment. In order to set the spectral positions of pump and probe beam it is crucial to know the energy range of the investigated QW band structure. For this purpose, both samples are studied under illumination with the 1.962 eV (632.8 nm) emission line of a helium-neon laser (HeNe). This excitation above the band gap of both GaAs and CdTe reveals the photoluminescence spectra of the electronic band structure. The signal is detected by means of the setup introduced in Section 2.2, applying only slight modifications to the alignment. The continuous-wave output of the HeNe laser is coupled into the probe arm of the setup shown in Fig. 2.2 while the Ti:sapphire laser is blocked. After the excitation under cryogenic temperatures the reflected light beam is blocked by a spectral longpass filter for 632.8 nm whereas the lower-exegetical PL emission of the sample is passed into the spectrometer. While the spectrometer is foremost operated as a monochromator for MOKE measurements it can as well be used to monitor the incident spectrum with a charge-coupled device (CCD) sensor. This operation mode facilitates the detection of the PL spectra shown in Fig. 3.1 from which information about the Fermi energy and thus the carrier density of the excited 2DEG is extracted. Furthermore, the detected energy range of the PL dictates the spectral adjustment of the pump beam which has to be tuned to a photon energy above the band gap.

The PL obtained from the GaAs sample for an applied gate voltage of $U_{\mathrm{BG}} = -1.00\,\mathrm{V}$ and a HeNe irradiance of $28.2\,\mathrm{W/cm^2}$ is depicted in Fig. 3.1 (a) as black line. Two peaks can be determined by visual inspection of the spectrum and a multiple peak fit reveals even three contributing Lorentz peaks. The fit reassembles the data with high accuracy and is shown as red transient in the plot. Remarkably, the two Lorentz peaks colored in dark and light grey remain visible even if the laser spot is spatially tuned away from the QW Hall bar structure, indicating an origin from the bulk GaAs substrate of the sample. This is further supported by the position of the dark grey peak which matches well with the band gap energy of bulk GaAs $E_{\mathrm{g}} = 1.519\,\mathrm{eV}$ at 3 K [116]. Consequently, only the remaining blue Lorentz peak in Fig. 3.1 (a) can be attributed to the QW. The spectral blue shift of this peak in respect to the bulk PL can be readily explained by the confinement energy introduced in Section 1.2. The related PL signal emerges directly from the conduction band of the QW due to recombination of free Fermi sea electrons with valence band holes [117]. Accordingly, the peak width is a good measure for the Fermi energy which is defined as the energy gap in between the surface of the Fermi sea and the bottom of the conduction band. Moreover, by extracting the FWHM

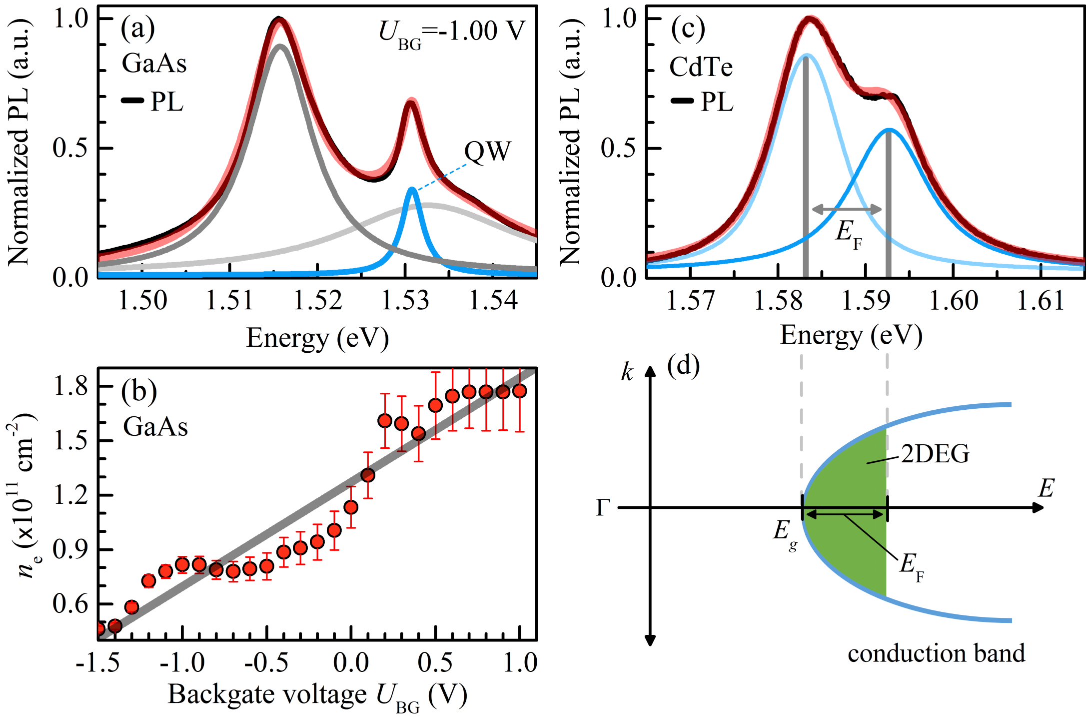

Fig. 3.1: Photoluminescence spectra taken for sample characterization. **(a)** PL spectrum of the GaAs sample with a multiple peak fit (red) that reassembles two substrate contributions (light and dark grey) and the 2DEG PL (blue) for $U_{\mathrm{BG}} = -1.00\,\mathrm{V}$. **(b)** Electron density n_{e} of the GaAs QW in dependence on U_{BG} extracted from the FWHM of the respective 2DEG PL peak as shown exemplarily for $-1.00\,\mathrm{V}$ in panel (a). **(c)** PL spectrum of the CdTe sample and corresponding multiple peak fit (red), revealing the Fermi energy as the energy difference of Fermi edge (dark blue) and the conduction band minimum (light blue) as illustrated schematically in **(d)**.

of the QW PL peak it is possible to estimate the carrier density of the 2DEG. This is because, the Fermi energy represents the energy spectrum of the 2DEG and is therefore directly related to the density of states in a two-dimensional system by $E_{\mathrm{F}} = \hbar\pi n_{\mathrm{e}}/m^*$ [48; 74]. From the peak fit $E_{\mathrm{F}} = 3.05\,\mathrm{meV}$ and a corresponding carrier density of $n_{\mathrm{e}} = 0.82 \times 10^{11}\,\mathrm{cm}^{-2}$ is found.

The value for n_{e} is slightly smaller than the density of $1.3 \times 10^{11}\,\mathrm{cm}^{-2}$ given in Table 2.1 and obtained from magneto-transport measurements without applied back gate voltage. This discrepancy suggests a depleting of the QW with decreasing U_{BG}. Such a trend can indeed be confirmed by comparing the Fermi energies extracted from the FWHM of the 2DEG PL peak for a variety of gate voltages. The resulting change in n_{e} is depicted in Fig. 3.1 (b) where a value of $n_{\mathrm{e}} = 1.13 \times 10^{11}\,\mathrm{cm}^{-2}$ is given for zero back gate voltage. This coincides much better with the mentioned results from magneto-transport experiments. Moreover, a straight grey line is added to the plot as a guide to the eye, suggesting a linear relation in first approximation. Within this thesis, all measurements on GaAs are performed for $U_{\mathrm{BG}} = -1.00\,\mathrm{V}$ and the probe tuned to the low energy flank of the PL at $1.530\,\mathrm{eV}$ ($\sim 809\,\mathrm{nm}$) while the pump is set to $1.570\,\mathrm{eV}$ ($\sim 790\,\mathrm{nm}$). The exact pump and probe photon energies are chosen based on an optimal spectral response of the 2DEG at maximum spatial and temporal overlap similar to the approach in [51]. The corresponding pulse-peak intensities are set to

$3.53\,\mathrm{MW/cm^2}$ and $2.36\,\mathrm{MW/cm^2}$ respectively.

Utilizing the same excitation and detection scheme as introduced above, the PL of the CdTe sample illustrated in Fig. 3.1 (c) is obtained with a HeNe irradiance of $\sim 350\,\mathrm{W/cm^2}$. In order to locate the shown PL spectrum in the band structure, the well known band gap energy of 1.475 eV for bulk CdTe at room-temperature (RT) is used [116]. From this value the corresponding emission line at 3.5 K is estimated by employing the Varshni formula [73]

$$E_\mathrm{g}(0\,\mathrm{K}) = E_\mathrm{g}(T) + \frac{\alpha_\mathrm{v} T^2}{T + \Theta_\mathrm{D}} \tag{3.1}$$

and inserting the necessary parameters for the Debye temperature $\Theta_\mathrm{D} = 140\,\mathrm{K}$ and $\alpha_\mathrm{v} = 3 \times 10^{-4}\,\mathrm{eV/K}$ [116]. As a result, the bang gap energy for low temperatures can be stated to be 1.536 eV, indicating a blue shifted PL by some tens of meV due to confinement effects. The data shown in the (c) panel are fitted best by a multiple peak fit with two combined Lorentz contributions illustrated as red transient. The high 2DEG density provided by magneto-transport measurements (cf. table 2.1) points at a suppression of PL from excitonic or trionic resonances [118; 119]. Therefore, it is assumed that the two peaks in the PL, centered at 1.582 eV and 1.591 eV, correspond to recombination to the valence band, arising from the conduction band minimum and from the Fermi edge respectively as visualized in Fig. 3.1 (d). For these energies, singularities in the density of states lead to an enhanced emission. This finding is in agreement with results in similar structures where n_e is tunable [120–122]. Consequently, it can be seen from the dashed lines in panel (d) that the spectral separation of the two peaks represents the 2DEG Fermi energy given by $E_\mathrm{F} = (9.0 \pm 0.1)\,\mathrm{meV}$. This corresponds to $n_\mathrm{e} = (3.5 \pm 0.1) \times 10^{11}\,\mathrm{cm^{-2}}$ which is very comparable to the expected density of $3.4 \times 10^{11}\,\mathrm{cm^{-2}}$ provided in Table 2.1. All measurements presented for the CdTe sample are performed with the probe tuned to 1.589 eV (780 nm) and the pump set to 1.621 eV (765 nm). Pump and probe pulse-peak intensities are set to $3.53\,\mathrm{MW/cm^2}$ and $2.36\,\mathrm{MW/cm^2}$.

3.2 Emergence of the PSH - Parameterization

Following the thesis structure, the present section serves as an introduction to the PSH phenomenon. The section is meant to accustom the reader to the preparation of data developed to visualize the SO coupling mechanisms that drive the measured PSH texture. Furthermore, it is set out how the parameters that are relevant for the PSH are extracted from the data. The section is concluded with a first quantification of the Rashba and Dresselhaus parameters and their validation via simulations based on the MC method and kinetic theory respectively. Measurements of spin polarization are performed by means of the MOKE effect, allowing for the extraction of S_z from the angle of Kerr rotation which is discussed thoroughly in Section 2.1. Representing the space- and time-resolved spin polarization $S_\mathrm{z}(x, y, t)$ data as false-color plot has proven to be a very effective way for the visualization of the PSH. Especially, compared to other, more abstract, experimental techniques such as inelastic light-scattering and spin gratings [45; 123] false-color plots warrant a good overview of the data. Here, a red to

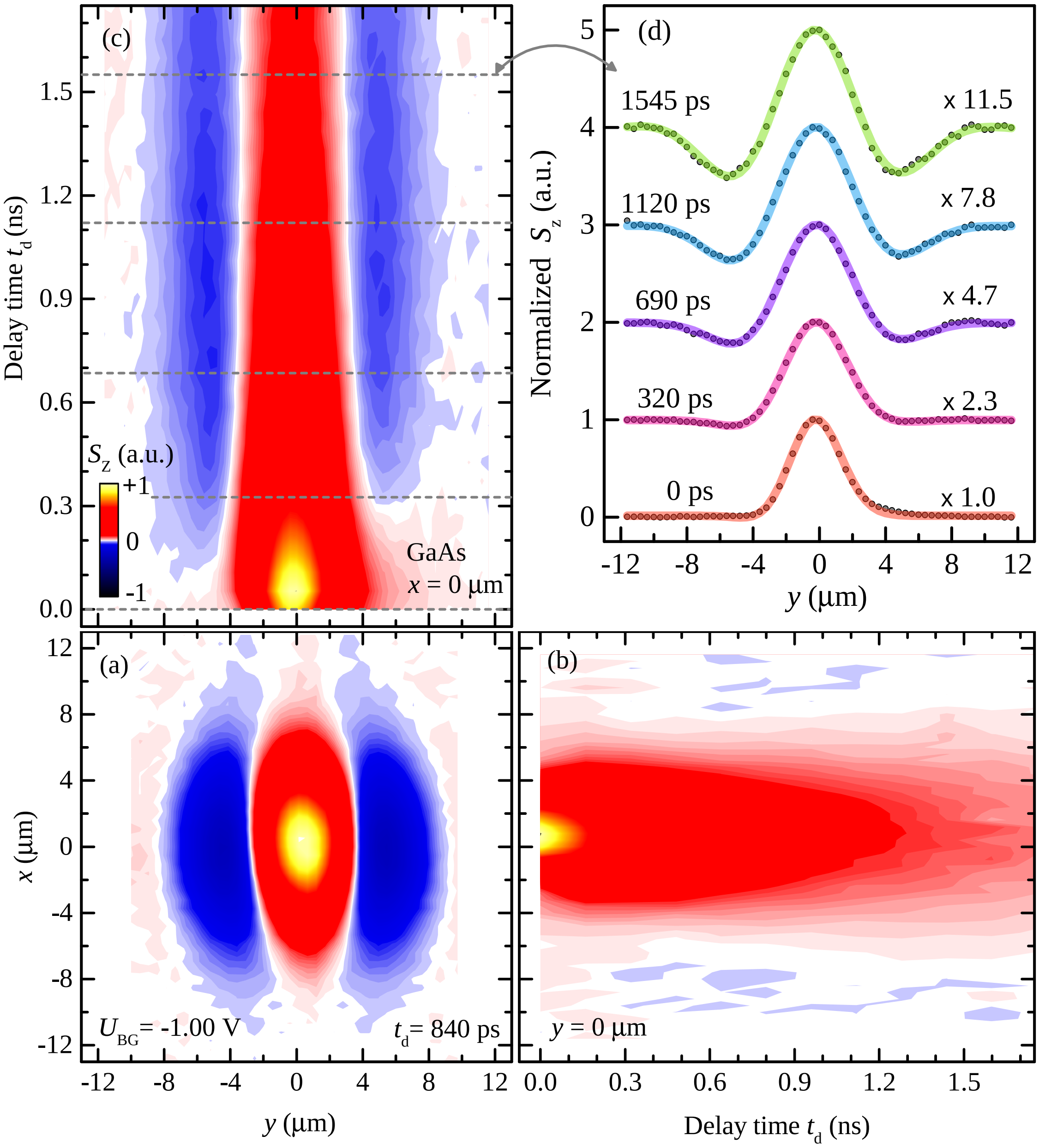

Fig. 3.2: Evolution of the spin polarization pattern in GaAs mapped out in space and time as false-color plots. **(a)** 2Dmap measurement of the PSH for a fixed delay time of 840 ps. **(b-c)** Spatiotemporal measurements for the x- and y-axis with the respective other spatial dimension fixed at zero. **(d)** Vertically shifted, exemplary line scans as normalized cutouts from the highlighted positions in panel (c), representing different delay times. The colored lines represent best fits to Eq. (3.3).

blue color scale indicates the two opposite orientations of S_z in relation to the QW plane and the coordinate system is given parallel to the crystal axes with $x \parallel [110]$ and $y \parallel [1\bar{1}0]$, complying with the equations of theory and other literature from the field.

Reviving Section 1.3.5, the PSH is expected to appear as a unidirectional wave of spin polarization driven by the diffusive expansion of electron spins in a balanced SIA and BIA regime. A first prediction of the resulting pattern was developed in Fig. 1.5 (e) where a parameterization with the spatial wavelength $\lambda_{0,y}$ was suggested. Additionally, it is discussed in Section 1.3.3 that the spatiotemporal dynamics of the electrons can be modeled with the spin diffusion equation. This equation implies a Gaussian distribution that undergoes an overall temporal decay and a simultaneous linear expansion in space. This behavior can indeed be observed in the experiments as shown in Fig. 3.2 for the GaAs sample.

The three false-color plots in this figure exemplify different ways of how the PSH can be observed, starting with a two-dimensional map (2Dmap) in space depicted in panel (a). This 2Dmap is taken for a constant back gate voltage of $-1.00\,\mathrm{V}$ and captures the diffusive state at a fixed delay time of 840 ps. In confirmation of the earlier introduced theory, the initially oriented spin polarization has not just expanded diffusively in space but has formed an oscillating pattern along the y-axis, indicating a rotation of S_z caused by effective fields. The temporal evolution of the PSH can be tracked by means of the spatiotemporal false-color plots in panel (b) and (c) along one of the two spatial axes respectively. Such spatiotemporal maps are composed from single line scans of S_z in dependence on the spatial position while the perpendicular position is fixed at zero. A subset of such line scans, taken for different delay times, are shown in panel (d) along the y-axis. Looking at the spatiotemporal x-axis data in panel (b), it becomes apparent that the spin polarization expands in space while an additional decay mechanism weakens the signal for long delay times. Moreover, the initial Gaussian shape is conserved over time and no oscillating features are present along the x-axis. However, along the y-axis the Gaussian spin distribution, shown in panel (d), reveals a more and more distinct oscillation in the micrometer range with proceeding t_d. This spatial anisotropy in the pattern is readily explained by the effective magnetic field distribution in k-space

$$\boldsymbol{B}_\mathrm{so}^{(1)}(\boldsymbol{k}) = \frac{2}{g\mu_\mathrm{B}} \begin{bmatrix} (\alpha+\beta)\cdot k_\mathrm{y} \\ (-\alpha+\beta)\cdot k_\mathrm{x} \end{bmatrix} \tag{3.2}$$

adapted from Eq. (1.33). This expression implies zero magnetic field for electrons that move along the x-axis in a regime of balanced Rashba and Dresselhaus SO coupling. This is because motion parallel to x-axis requires $k_\mathrm{y} = 0$ whereas $\alpha/\beta = 1$ results in $(-\alpha+\beta) = 0$. In combination both components of $\boldsymbol{B}_\mathrm{so}^{(1)}$ are set to zero and thus no precession takes place along the x-axis.

The observed PSH evolution in Fig. 3.2 is in excellent agreement with previous studies in similar structures and the individual line slices along the y-axis can be described by the fit function

$$S_\mathrm{z}(y) = A_0 \cdot e^{-4\ln(2)(y-y_\mathrm{c})^2/w^2} \cdot \cos\left[\frac{2\pi(y-y_1)}{\lambda_\mathrm{so,y}}\right] \tag{3.3}$$

which combines the Gaussian solution of the spin diffusion equation derived in Eq. (1.24) and a cosine modulation with the PSH wavelength $\lambda_\mathrm{so,y}$. This wavelength is also referred to as spin precession length and characterizes the distance over which a full spin precession is undergone. While the oscillation is centered around the cosine phase parameter y_1 the spatial parameter

y_c denotes the center of the Gaussian spin polarization in space. The fit function models line scans for a fixed delay time. Hence, all effects of decay and diffusion mechanisms which affect the amplitude of the spin distribution are integrated into the temporal change of the amplitude parameter A_0. The transparent color lines in Fig. 3.2 (d) represent best fits of the fit function in Eq. (3.3) to the individual cutout lines from the corresponding spatiotemporal map along the y-axis. The good agreement of the data with the fit stands as a qualitative justification for the chosen fit model based on the spin diffusion equation. Coming back to the 2Dmap in panel (a), it is remarkable that the blue colored PSH stripes exhibit a slight curvature. This is an indicator for a regime of BIA and SIA that is not entirely balanced and thus imposes a slow precessing contribution as well along x-axis. This feature will be further quantified and discussed below (cf. Fig. 3.10).

Having discussed the appearance and evolution of the PSH qualitatively, the focus shall now be shifted towards a more quantitative description of the phenomenon with a parameterization by means of the introduced fit function $S_z(y)$. In order to compare GaAs and CdTe based SO coupling, extracted fit parameters are given in parallel for both materials in Fig. 3.3 whereas the respective spatiotemporal measurement for CdTe is shown thereafter in Fig. 3.4. Figure 3.3 (a) depicts the precession length of the PSH in dependence on delay time. For both materials $\lambda_{\mathrm{so,y}}$ exhibits a reciprocal dependence on time which is not covered by the static expression in Eq. (1.36) found in the theoretical background. However, it has been shown in literature that a continuous change of the PSH Fourier spectrum occurs during the transformation from a Gaussian spin distribution at short delay times towards a single mode oscillation at long times [42; 124]. This so called finite-spot size effect results in a gradual approach of $\lambda_{\mathrm{so,y}}$ to the PSH mode $\lambda_{0,\mathrm{y}}$, following the relation

$$\lambda_{\mathrm{so,y}}(t_{\mathrm{d}}) = \lambda_{0,\mathrm{y}} \left[1 + \frac{w_0^2}{16\ln(2) D_{\mathrm{s}} t_{\mathrm{d}}}\right] \quad \text{with} \quad \lambda_{0,\mathrm{y}} = \frac{\pi\hbar^2}{m^*}(\alpha+\beta)^{-1} \tag{3.4}$$

that depends on the initial spot size w_0 and the diffusion coefficient [56]. The experimental data of $\lambda_{\mathrm{so,y}}$, extracted from spatiotemporal measurements, are shown together with a best fit that reveals the PSH wavelength to be $(5.6 \pm 0.1)\,\mu$m for CdTe and $(11.2 \pm 0.2)\,\mu$m for GaAs. This results can be made more comparable by the calculation of $(\alpha + \beta)$, resulting in (3.19 ± 0.05) meVÅ for GaAs and (4.55 ± 0.08) meVÅ for CdTe. At first glance the difference in between CdTe and GaAs is not very distinct, however, a general comparison should be performed on the level of the Dresselhaus coupling constant γ_{D} to rule out the dependence of α and β on sample-specific parameters such as the electron density and the QW thickness (cf. Eq. (1.29)). This discussion is postponed to Section 3.3.1 where the BIA and SIA parameters are determined individually.

Furthermore, the space- and time-resolved measurements allow for the extraction of the spin diffusion coefficient D_{s} by tracing the squared spatial width $w^2(t)$ of the Gaussian envelope function with time. Corresponding data for both samples are shown in the (b) panel of Fig. 3.3. Here, the linear time dependence $w^2(t) = w_0^2 + 16\ln(2)D_{\mathrm{s}}t$ of the squared FWHM,

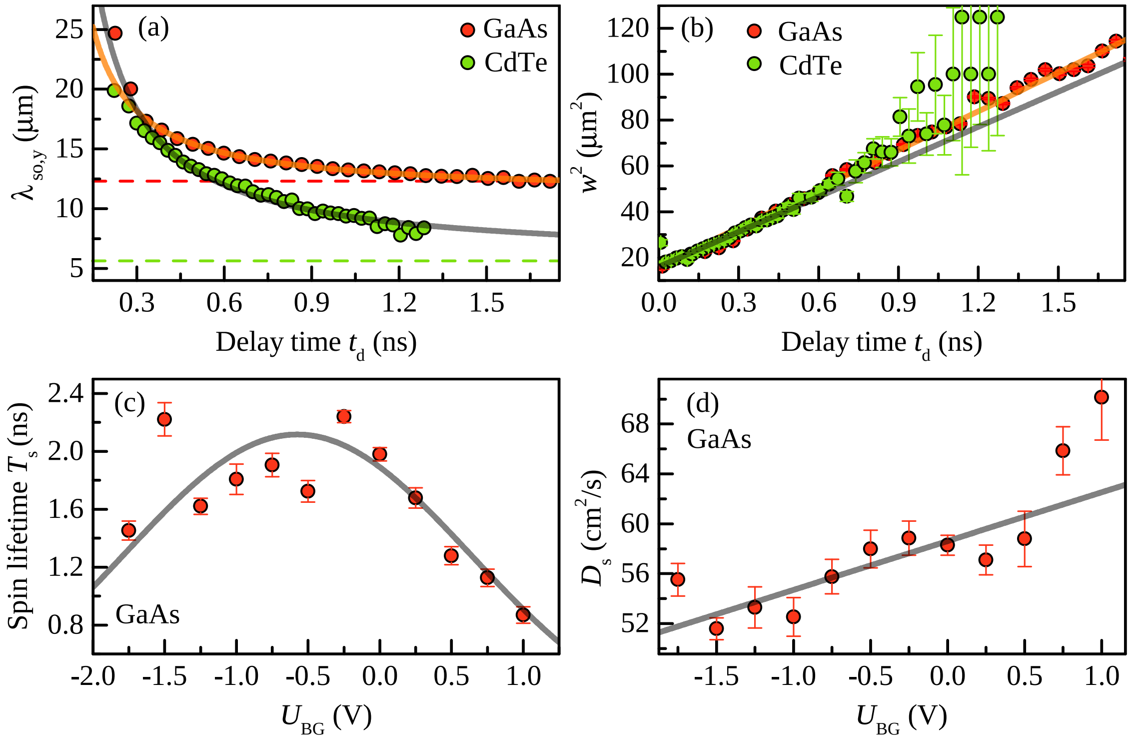

Fig. 3.3: Spatiotemporal PSH parameters extracted for varying delay times in both materials and in dependence on gate voltage for GaAs. **(a)** Temporal evolution of the spatial precession length together with best fits to the theory of finite-spot sizes. Prediction for $\lambda_{0,\mathrm{y}}$ is indicated by dashed lines for both materials respectively. **(b)** Diffusion induced spatial expansion of the Gaussian envelope function parameterized by the squared FWHM plotted versus delay time together with linear fits. The extracted diffusion coefficient for GaAs is shown in **(d)** for a variable gate voltage. **(c)** Peak-like trend of the spin lifetime induced by the level of balance in between α and β. Gaussian peak fit for comparison.

derived in Eq. (1.26), is utilized for the extraction of $D_\mathrm{s} = (50 \pm 10)\,\mathrm{cm}^2/\mathrm{s}$ in CdTe and $(54.0 \pm 0.8)\,\mathrm{cm}^2/\mathrm{s}$ in GaAs. Best fits are added to the plot as transparent lines. The elevated error of the CdTe diffusion coefficient results from averaging multiple fit results obtained from different measurements. A thorough discussion of the fit quality is given in Section 3.3.4 where deviations of fit and data are attributed to a complex spatial gradient of the SO coupling parameters. Considering the 2DEG to be degenerate at 3.5 K facilitates the calculation of the momentum relaxation time τ_ee from the theoretical relation

$$D_\mathrm{s} = \frac{\tau_\mathrm{ee} \cdot E_\mathrm{F}}{m^*} \tag{3.5}$$

where the Fermi energy is provided by the PL measurements in Fig. 3.1. The resulting values are documented in the overview Table 3.1 together with all other sample-specific parameters. In Fig. 3.1 it is studied how the carrier density is affected by tuning the back gate voltage in the GaAs sample, leading to a simultaneous variation of E_F. This changes by roughly a factor of three should result in a similar strong dependence of D_s on U_BG, taking into account Eq. (3.5). The experimentally observed change depicted in 3.3 (d), however, is much weaker since only a tuning by $\sim 30\,\%$ can be confirmed. This discrepancy is accounted for by the fact that the 2DEG cannot be treated as degenerate gas but is rather in an intermediate regime towards non-degenerate statistics. In addition, it is likely that an increased electron density is accompanied by a reduction in the scattering time, counteracting an increasing E_F in Eq. (3.5) [125].

Next to the already discussed spatial parameters $\lambda_\mathrm{so,y}$ and D_s, the investigation of spin lifetimes is of peculiar interest. It is expected that the SU(2) symmetry, which gives rise to the PSH, creates a regime that is extraordinarily robust against spin decoherence caused by the DP mechanism. The spin lifetime of the PSH is extracted from the temporal decay of the fit function amplitude parameter A_0 with time. Here, it is important to distinguish the exponential loss of spin coherence and the fact that the amplitude is decreased by spins that diffuse away from the spot of excitation. A combination of these two contributions results in the expression

$$A_0(t_\mathrm{d}) = A_0(0) \cdot \frac{\pi \ln(2) w_0^2}{w_0^2 + 16 \ln(2) D_\mathrm{s} t_\mathrm{d}} \cdot e^{-t_\mathrm{d}/T_\mathrm{s}} \tag{3.6}$$

taken from Eq. (1.25) in the theoretical background. Having the extracted values for D_s and w_0^2 available, the general spin lifetime T_s can be obtained from best fits of Eq. (3.6) to the delay time dependence of $A_0(t_\mathrm{d})$. The time dependence of $A_0(t_\mathrm{d})$ is extracted beforehand from a spatiotemporal map where every line scan of $S_\mathrm{z}(y)$ for a fixed delay time provides one value of A_0. Repeating the extraction of $A_0(t_\mathrm{d})$ from spatiotemporal maps with different applied U_BG leads to Fig. 3.3 (c) where T_s is shown in dependence on the gate voltage. The spin lifetimes of up to $\sim 2.2\,\mathrm{ns}$ can be demonstrated to follow a peak-like behavior centered at $U_\mathrm{BG} = -0.5\,\mathrm{V}$ and a best fit with a Gaussian peak, shown as grey transparent line, serves as guide to the eye. A peak-like tuning of lifetimes around a certain gate voltage has been forecasted and observed in literature for the PSH in different regimes [44; 51; 102; 126; 127]. This finding originates from the variation of the Rashba parameter α that depends on the electric field $\mathcal{E}_\mathrm{QW}$ along the growth direction of the QW heterostructure and thus is directly influenced by the electric field created by U_BG. The k-space distribution of the effective magnetic field in Fig. 1.5 shows a clear dependence of the SU(2) symmetry on the level of balance in between α and β. As this symmetry suppresses the DP mechanism and therefore leads to very long spin lifetimes the peak in T_s is assumed to appear for a voltage where α is tuned as close as possible towards β. Later studies of α/β in dependence on U_BG (cf. Fig. 3.12) do not confirm a peak in the ratio but rather suggest a gradual approach towards $\alpha = \beta$ for decreasing gate voltage. As a consequence, the decrease in lifetime for negative U_BG (low electron density) is attributed to an increased influence of the Bir-Aronov-Pikus effect. This decay mechanism is based on the scattering of electrons and holes, becoming more important when the resident electron gas is depleted. This finding justifies the choice of $U_\mathrm{BG} = -1.00\,\mathrm{V}$ for all following measurements since this voltage combines a preferably balanced PSH regime with strong Kerr rotation signals. The KR signal itself is altered by U_BG via a density dependent resonance shift,

Table 3.1: List of sample parameters extracted from the PSH characterization for both materials. For CdTe a short and a long decay time are observed.

Material	$\lambda_0\,(\mu\mathrm{m})$	$D_\mathrm{s}\,(\mathrm{cm}^2/\mathrm{s})$	$w_0\,(\mu\mathrm{m})$	$[\alpha+\beta]\,(\mathrm{eV\AA})$	T_s (ps)	E_F (meV)	τ_ee (ps)
GaAs	$(11,2\pm0.2)$	(54.0 ± 0.8)	3.62	(3.19 ± 0.05)	~ 2200	3.05	0.6
CdTe	(5.6 ± 0.1)	(50 ± 10)	3.87	(4.55 ± 0.08)	1350/170	(9.0 ± 0.1)	0.3

affecting the optical detection (cf. Fig. 2.2 (c)). In conclusion, the fundamental parameters of the PSH in GaAs and CdTe could be mapped out and are noted down in the parameter Table 3.1.

From the theory point of view, the PSH is fully described by the parameters extracted above. Aiming at a qualitative validation of the parameters they can be fed into a simulation and the obtained output can be compared with the experimental results, using false-color micrographs. The simulations presented in this thesis are generated by two different models and a more detailed explanation of the employed methods is discussed in the Appendices A.1 and A.2. The Monte Carlo (MC) simulation models a diffusive random walk in a regime of effective magnetic fields by means of stochastic probabilities. On the other side, the Kinetic Theory (KT) simulation is based on numerical solutions of the spin diffusion equation established in Section 1.3.3 [42; 51]. Figure 3.4 depicts three sets of a 2Dmap and spatiotemporal map along the y-axis each. The sets represent one measurement on the CdTe sample and two simulations that utilize the CdTe parameters from Table 3.1. Although, only the sum of Rashba and Dresselhaus parameter is known so far, the required individual parameters could in-principle be calculated since a theory value of β is given in Table 2.1. However, for the simulations given here the individual parameters are taken from a later section of this thesis (cf. Table 3.2) to obtain the highest accordance with the experiment. Panel (a) shows the state of the PSH after 770 ps delay characterized by the same unidirectional spin helix wave as in GaAs, however, with a shorter spin precession length if compared with the analogous measurement in GaAs that is depicted in Fig. 3.2. This finding of the Larmor precession pattern confirms the predominant appearance of $\boldsymbol{B}_\mathrm{so}$ for electrons that propagate along the y-direction, being validated by both simulated 2Dmaps. A similar strong agreement is found by visual comparison of the spatiotemporal maps that show the measurement (a) and simulations (b-c).

While the general reproduction is successful and thus suggests the model to be accurate some smaller deviations can be sought out. Firstly, the polarization stripes of the experimental 2Dmap are visibly curved which is not reassembled by neither of the two simulations. This curvature cannot be explained by an imbalance of α and β as such effects would appear in both simulations. It therefore seems more likely that the curvature is a feature that arises from spatially varying SO coupling which will be discussed in-depth later on in Section 3.3.4. Secondly, S_z at the spatial and temporal overlap appears much more striking in the measurement than in the simulations. This observation suggests a much faster decline of the

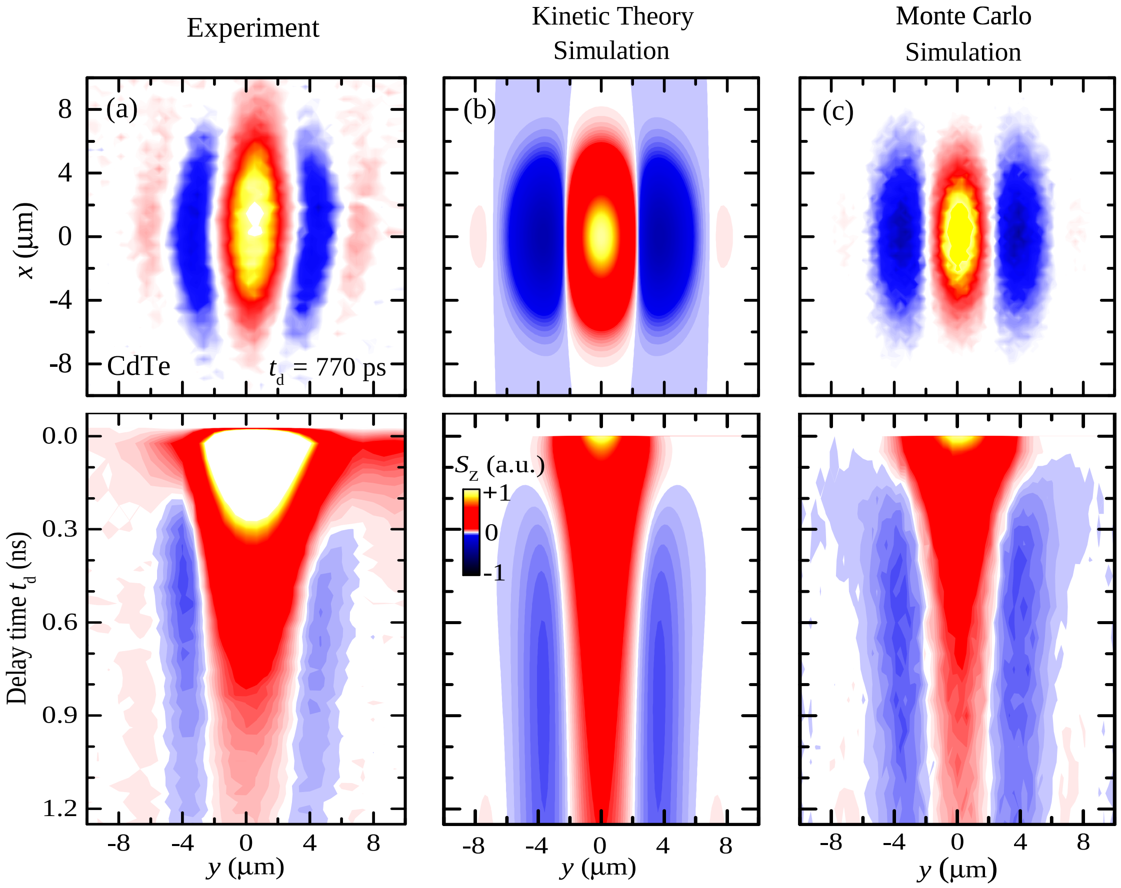

Fig. 3.4: 2Dmap of the PSH in CdTe for 770 ps and the corresponding spatiotemporal evolution along the y-axis assembled from **(a)** MOKE measurements of $S_z(x, y)$, **(b)** simulations based on numerical calculations of kinetic theory and **(c)** MC simulations conducted with 0.5×10^6 electrons and $\tau_{ee} = 0.3$ ps. The parameters used for the simulations are taken from Table 3.1 and the individual values of α and β are taken from Table 3.2.

spin polarization at the beginning of the experiment for $t_d < 300$ ps. Indeed, a secondary, fast exponential decay with a lifetime of 170 ps is seen in $A_0(t_d)$. This finding cannot be attributed to thermal effects due to the advanced time scale. However, a variety of effects can account for short-lived contributions in the present system. For instance, it cannot be ruled out that an unwanted spin polarization with short lifetime is injected into the substrate where it distorts the spin signal which comes from the QW. Another effect could arise from a high photocarrier density at the temporal overlap, increasing inelastic scattering rates and spin-spin interactions. Finally, a two-fold decay that is related to the finite-spot size effect is generally expected. Due to the initial transformation of a Gaussian spectrum into the single PSH mode an additional short decay arises at the beginning of the measurement. For longer delay times, the decay is dominated by the pure PSH lifetime which is discussed in the end of Section 1.3.5. Such effects for short delay times are not included in the simulations and thus are a reasonable explanation of the encountered differences.

Simulations performed with parameters for GaAs are available in [51] for a sample similar to the one used in this work and show remarkable success in reproducing the experimental data.

3.3 Manipulation of the PSH

In the previous section, the PSH is introduced and a visualization technique by means of false-color plots is established. In this section, the focus is now shifted from observational measurements towards manipulation and control of the spin polarization within the PSH. Therefore, a variety of different control knobs are consecutively investigated and their effects are quantified. Next to the application of magnetic fields, the influence of back gate voltage is studied and the PSH is exposed to in-plane electric fields in order to introduce spin drift. In particular, the latter case is of interest as peculiar effects on the SO coupling parameters have been reported in recent literature. However, the nature of the related changes, that are visible, e.g., in the spin precession length of the PSH, are not yet fully consistent. Hence, special attention is paid to the dependence of $\lambda_{0,\mathrm{y}}$ on the in-plane electric field strength for which contradicting trends are claimed in [51; 54; 55]. Besides the application of external magnetic and electric fields, the SO coupling is strongly affected by the injection of photo excited carriers into the 2DEG of the CdTe QW. This finding enables an all-optical approach towards PSH control in the CdTe sample.

3.3.1 In-plane Magnetic Fields

The characteristic spin wave texture of the PSH is shaped by effective magnetic fields oriented along the QW plane. From this fact arises the question how these effective magnetic fields can be influenced by external magnetic fields. Here, the external magnetic field $\boldsymbol{B}_{\mathrm{ex}} = (B_{\mathrm{ex,x}}, B_{\mathrm{ex,y}}, 0)$ is defined along the high symmetry coordinate system of the zincblende crystal defined by $x \parallel [1\bar{1}0]$ and $y \parallel [110]$. Since the applied external field strength can be precisely controlled it is possible to quantify the effective magnetic fields in certain configurations where they are annihilated by the chosen external fields. Accordingly, the Rashba and Dresselhaus parameters can be determined individually from measurements in external magnetic field and are shown below and in Table 3.2 for both materials.

The panels (a-c) of Fig. 3.5 illustrate the effect of different applied magnetic field strengths on the spatiotemporal evolution of the PSH in the GaAs sample. As observed above the spin helix without external manipulation, shown in (a), evolves symmetrically around the origin. This follows from the fact that spins detected at a constant y-position do not precess with time but keep a constant phase y_1 in the cosine argument of the fit function in Eq. (3.3). The position of constant phase is highlighted in panel (a) by a grey, dashed line. An additional external magnetic field $B_{\mathrm{ex,x}}$, however, imposes a temporal spin precession with a Larmor frequency of $\omega_{\mathrm{L}} = g\mu_{\mathrm{B}}B_{\mathrm{ex,x}}/\hbar$ induced by Zeeman splitting. This temporal precession at a fixed spatial position is referred to as spin beats in literature [96]. Such spin beats become visible in Fig. 3.6 (e) where the time dependence of S_{z} at position $(x, y) = (0, 0)$ is depicted

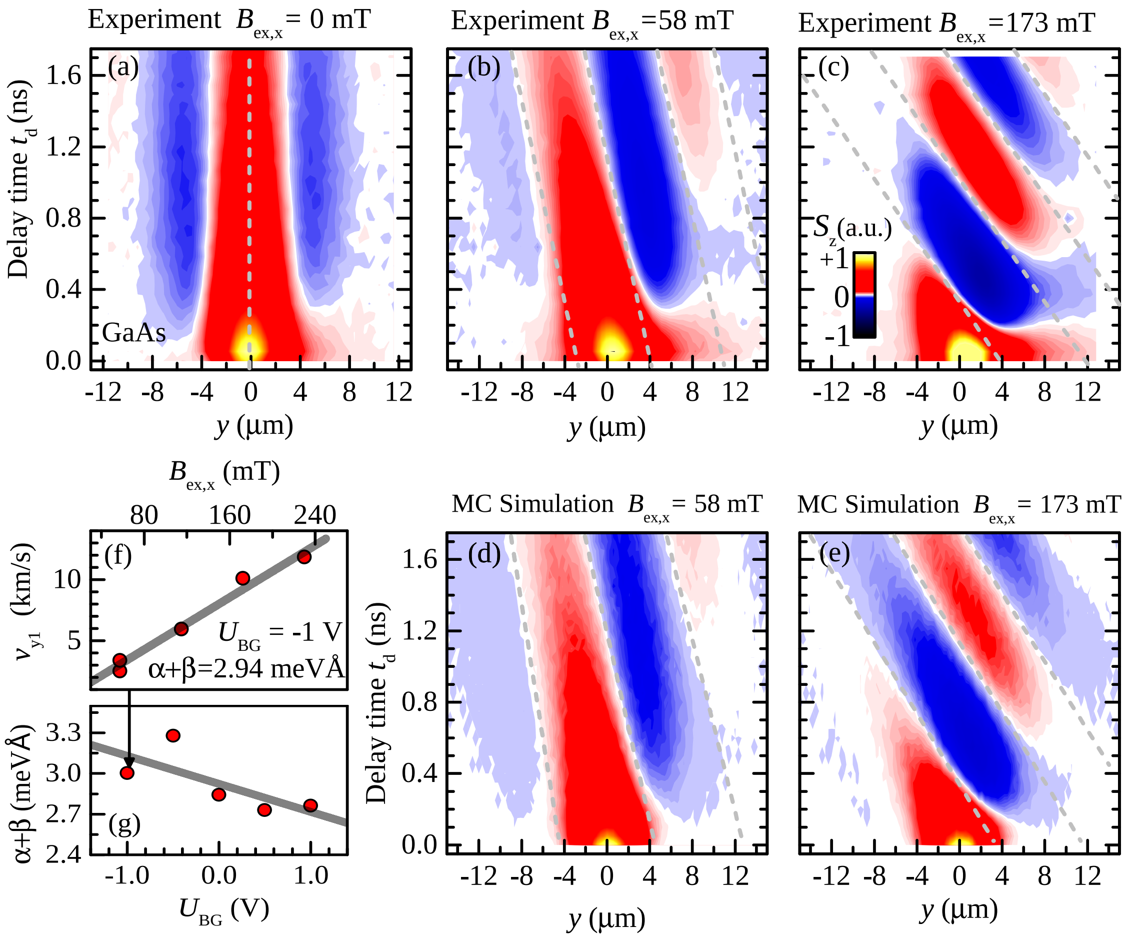

Fig. 3.5: Spatiotemporal evolution of the PSH in GaAs traced along the y-axis for different strengths of external magnetic field applied along the x-direction. **(a-c)** Field induced rotation of the PSH indicated by a tilted stripe pattern with y_1 illustrated as grey dashed line. **(d-e)** MC simulations reassemble the experimental data shown in (b,c) respectively. **(f)** Dependence of tilt on $B_{\mathrm{ex,x}}$, quantified by the phase velocity v_{y1}. **(g)** Summed Rashba and Dresselhaus parameters in dependence on U_{BG} extracted from linear fits for each data point as exemplarily shown for -1 V in (f).

for an applied magnetic field strength of 230 mT. A best fit to an oscillating, single exponential decay function reveals the Larmor frequency and thus the g-factor of the GaAs with $g = -0.29$. The g-factor in bulk GaAs is known to be -0.44 and a trend towards positive values in narrow QWs is observed [128–130]. Consequently, it is reasonable to assume a negative g-factor as well for the present 15 nm QW. Equivalent measurements in the CdTe sample yield a g-factor of 1.6 , coinciding with publications on the same structure [56; 131].

Coming back to the spatiotemporal measurements in Fig. 3.5 (b) and (c), the external magnetic field seems to tilt the PSH stripes in the false-color plot representation with time. As a guide to the eye this tilt is highlighted by grey, dashed lines in the plot, indicating the position of constant phase. From comparison of panel (b) and (c) a steepening of the tilt is observed with increasing field strength. Generally, the tilt represent an electron velocity v_{y1}

for which the spin precession phase is constant. This is equivalent to a fixed spin orientation for electrons that travel with the average momentum $\hbar k_{\mathrm{y1}} = m^* v_{\mathrm{y1}}$. As propagating spins are usually rotated by an effective magnetic field that is momentum-dependent (cf. $\boldsymbol{B}_{\mathrm{so}}^{(1)}$ in Eq. (3.2)) it must be assumed that the resulting effective field is canceled out by the external magnetic field. This is mathematically described by an equilibrium of the non-zero field components $B_{\mathrm{so,x}}^{(1)} = B_{\mathrm{ex,x}}$ that can be rewritten into the expression

$$v_{\mathrm{y1}} = \frac{\mathrm{d}y_1}{\mathrm{d}t} = \frac{g\hbar\mu_{\mathrm{B}}}{2m^*(\alpha+\beta)} \cdot B_{\mathrm{ex,x}} \tag{3.7}$$

by reformulating Eq.(3.2). Here, k_{y1} corresponds to the wave vector attributed to the fraction of electrons that travel along the grey dashed lines and in parallel to the PSH stripes of constant phase. The experimental values of $v_{\mathrm{y1}} = \mathrm{d}y_1/\mathrm{d}t$ range up to several kilometers per second and can be obtained from a linear fit to the delay time dependence of y_1. For this fit the individual cosine phase parameter y_1 for each delay time has to be determined from y-axis cutouts of the respective spatiotemporal map.

The concept of PSH manipulation by external magnetic fields is sketched in a more visual manner in Fig. 3.6 (f) where the magnetic field distribution in k-space is shown along the k_{y}-axis for the cases without (on the left) and with (on the right) external field. It can be seen that the linearly distributed effective field vectors are canceled for negative momenta and enhanced for positive momenta if the external magnetic field is oriented parallel to the x-axis. Accordingly, the position in k-space for which no field acts on the electron spins is shifted from the origin at $k_{\mathrm{y}} = 0$ to some finite momentum value. Diffusing electrons that exhibit this specific momentum will thus not precess and maintain their initial spin polarization. The application of different magnetic field strengths along the x-axis, exemplified by the two measurements in Fig. 3.5 (b) and (c), and the subsequent extraction of v_{y1} facilitates the determination of $(\alpha+\beta)$. More precisely, a linear regression based on Eq. (3.7) is used to obtain the summed Rashba and Dresselhaus parameter. The corresponding linear fit is depicted in Fig. 3.5 (f) together with the data which represent the phase velocity v_{y1} in dependence on $B_{\mathrm{ex,x}}$, yielding a value of $(\alpha+\beta) = 2.94\,\mathrm{meV\mathring{A}}$. This value is in good agreement with the value in Table 3.1 determined from the spin precession length.

Moreover, measurements in the presence of external magnetic field are used to study the influence of the gate voltage on α and β. For this reason, measurements of tilted stripes and the subsequent extraction of the Rashba and Dresselhaus parameters are performed for different back gate voltages. The acquired data are shown in Fig. 3.5 (g) and reveals a clear trend for a decrease of the summed SO coupling parameters with increasing U_{BG}. The back gate voltage has indirect impact on both β_3 via the carrier density and α via the electric field along the QW. Consequently, it must be concluded that a complex mutual dependence is present which is investigated in more detail in Section 3.3.3.

The proposed explanation for the observed tilt in the PSH stripes is confirmed by corresponding simulations based on the MC method. Similar to the simulations presented in the preceding section the spatiotemporal emergence of the PSH in the presence of in-plane magnetic fields can be modeled with the Monte Carlo approach outlined in A.2. For this purpose, all electron spins are collectively rotated with the same frequency around the chosen external field vector, adding up to the effective field precession. As a result, the false-color plots in Fig. 3.5 (d) and (e) are created. These simulations reassemble the experimental observations with good precision, confirming the MC model as a suitable tool to describe the PSH even if the pattern is tilted by external magnetic fields. The whole set of measurements presented for GaAs in Fig. 3.5 can be repeated for the CdTe sample and the value for $(\alpha+\beta)$, which is close to the value given by the spin precession length, is incorporated in Table 3.2. However, for CdTe the simulations based on the MC method show significant dissimilarities with the corresponding experimental data due to the influence of optical induced photo carriers. For this reason, the false-color plot representations of experiment and simulation are shown in the later Section 3.3.4 where a thorough discussion is given.

The data discussed so far dealt with the application of external magnetic fields along the x-axis. This orientation allows for canceling or enhancing the effective magnetic fields seen by the electron spins that propagate along the y-axis, revealing the summed SO coupling parameters. On the contrary, by a rotation of the magnetic field to the y-direction it is possible to access the difference of Rashba and Dresselhaus parameter $(\alpha-\beta)$ from spatiotemporal maps recorded along the x-axis. Such data are shown in the panels (a-c) of Fig. 3.6 where a visual inspection suggests a stronger tilt of the PSH stripes compared with the analogous maps of the previous figure. By adapting the fit function (3.3) for the spin distribution along the y-axis, a similar formula can be stated for the distribution of spin polarization along the x-axis as

$$S_{\mathrm{z}}(x)=A_0\cdot e^{-4\ln(2)(x-x_{\mathrm{c}})^2/w^2}\cdot\cos\left[\frac{2\pi(x-x_1)}{\lambda_{\mathrm{so,x}}}\right]\tag{3.8}$$

with the Gaussian envelope centered around x_{c} and the cosine phase parameter x_1. Other than for the fit function used along the y-axis the spin precession length along the x-axis reads

$$\lambda_{\mathrm{so,x}}(t_{\mathrm{d}})=\lambda_{0,\mathrm{x}}\left[1+\frac{w_0^2}{16\ln(2)D_{\mathrm{s}}t_{\mathrm{d}}}\right]\quad\text{with}\quad\lambda_{0,\mathrm{x}}=\frac{\pi\hbar^2}{m^*}(-\alpha+\beta)^{-1}\tag{3.9}$$

and is determined by the difference of Rashba and Dresselhaus parameter. Accordingly, a much longer wavelength has to be expected since the difference of the two balanced entities is supposed to approach zero for a perfectly balanced PSH regime. Extracting the temporal dependence of the x_1 parameter from the spatiotemporal measurement by means of Eq. (3.8), the difference $(-\alpha+\beta)$ is obtained from the x-axis phase velocity that takes the form

$$v_{\mathrm{x1}}=\frac{\mathrm{d}x_1}{\mathrm{d}t}=\frac{g\hbar\mu_{\mathrm{B}}}{2m^*(-\alpha+\beta)}\cdot B_{\mathrm{ex,y}}\tag{3.10}$$

and is derived analogously to $\mathrm{d}y_1/\mathrm{d}t$. Panel (d) of Fig. 3.6 confirms this linear dependence on the external magnetic field. Moreover, the significantly higher velocities compared to v_{y1}

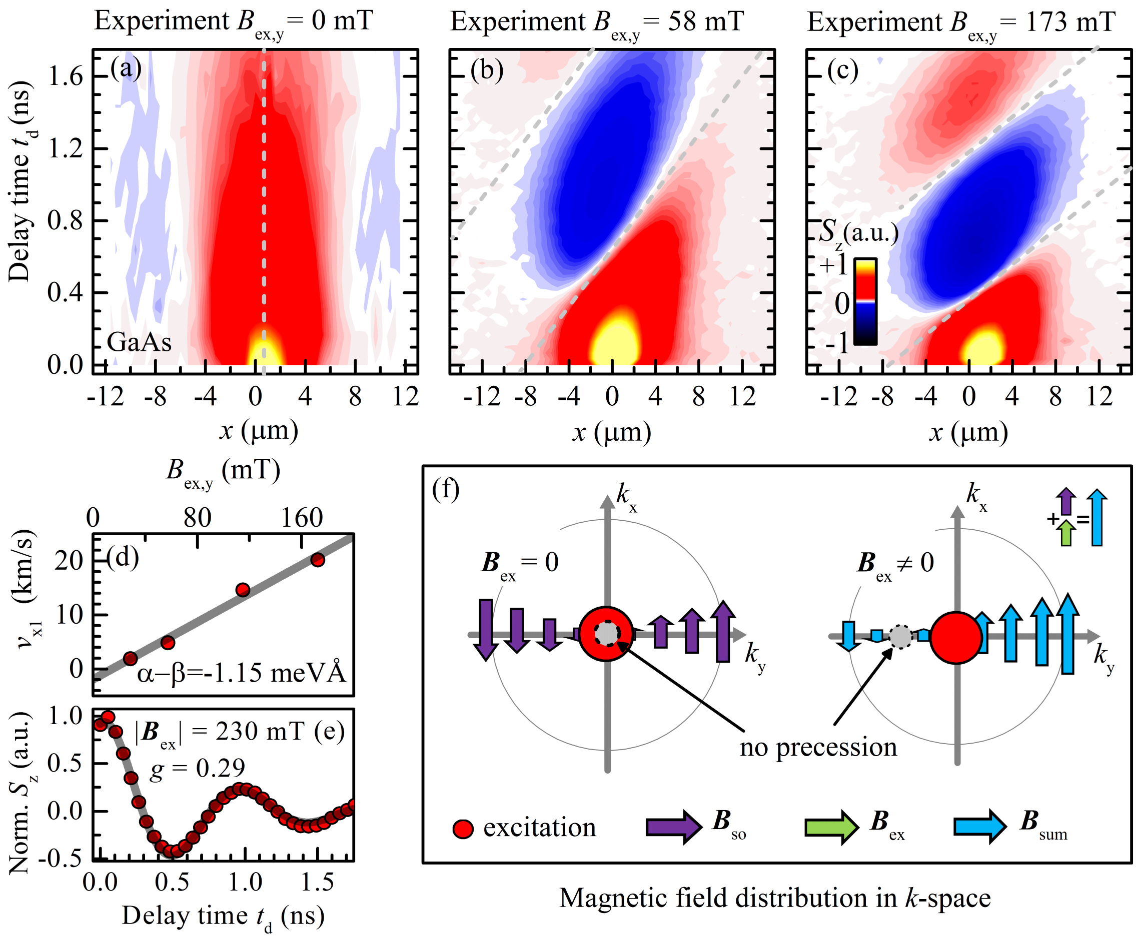

Fig. 3.6: **(a-c)** Spatiotemporal evolution of the PSH in GaAs traced along the x-axis for different strengths of external magnetic field applied along the y-direction. Field induced rotation of the PSH indicated by a tilted stripe pattern where grey, dashed line illustrate the phase velocity $v_{\mathrm{x},1}$. **(d)** Dependence of $v_{\mathrm{x},1}$ on $B_{\mathrm{ex,y}}$. **(e)** Exemplary line scan with magnetic field induced spin beats for a fixed spatial position at $(x, y) = (0\,\mu\mathrm{m}, 0\,\mu\mathrm{m})$. **(f)** Schematic concept of PSH manipulation by means of external magnetic fields with the corresponding field distribution illustrated in k-space. The scheme describes the situation for fields applied along the x-axis but can be qualitatively adapted to the y-axis by simply flipping the axis labeling.

are in agreement with the assumption of a PSH regime where the SO coupling parameters are similar and the difference therefore small. From a best linear fit it is possible to extract $(-\alpha + \beta) = 1.15\,\mathrm{meV\AA}$ and calculate the individual parameters $\alpha = 0.90\,\mathrm{meV\AA}$ and $\beta = 2.05\,\mathrm{meV\AA}$.

The ratio of $\alpha/\beta \sim 0.5$ points at a strongly unbalanced PSH regime but theoretical calculations and the so far presented simulations show that the SU(2) symmetry is still distinct enough to observe typical PSH characteristics. In retrospect, this imbalance can be made responsible for the convex curvature in the 2Dmap of Fig. 3.2 [42]. Values for the CdTe sample are incorporated as well in Table 3.2 and exhibit a ratio of $\alpha/\beta \sim 1.35$. In summary, the level of balance in the CdTe sample is slightly higher than in GaAs, however, both samples do not exhibit an optimal PSH regime.

Table 3.2: Overview about the Rashba and Dresselhaus parameters extracted by means of magnetic fields in sum, difference and individual.

Material	$[\alpha+\beta]$ (meVÅ)	$[-\alpha+\beta]$ (meVÅ)	α (meVÅ)	β (meVÅ)	g
GaAs	(2.94 ± 0.11)	(1.15 ± 0.09)	(0.90 ± 0.14)	(2.05 ± 0.14)	0.29
CdTe	(4.08 ± 0.33)	(0.63 ± 0.01)	(2.35 ± 0.33)	(1.73 ± 0.33)	1.6

3.3.2 In-plane Electric Fields

While the application of magnetic fields affects foremost the spin magnetic moments due to rotation of the spin polarization, the diffusive motion of the spin carriers remains unperturbed. Within this section, it is discussed how the electrons in the 2DEG of the GaAs QW can be controlled by in-plane electric fields along the x- and y-axis of the sample. These fields are created by applying bias to the sample in accordance with the wiring diagram shown in Fig. 2.3 in the Experimental Techniques Section. Recently, the effect of electric fields on the PSH evolution has raised special interest due to contradicting observation in regard to the dependence of $\lambda_{0,\mathrm{y}}$ on the field strength. While earlier investigations of Altmann *et al.* (2016) report an unchanged spin precession length it has been seen by Kunihashi *et al.* (2017) and Anghel *et al.* (2018) that $\lambda_{0,\mathrm{y}}$ varies with electron drift, however, with opposite dependences on the field strength [51; 54; 55]. The work discussed in the following section proposes an increased 2DEG temperature due to bias induced heating as tuning mechanism for the PSH. The suggested approach is based on the temperature dependence of the Fermi-Dirac statistic discussed similarly by Kunihashi *et al.* and attempts to connect the diametrical observations. In the same context, this thesis reports on a peculiar tunability of the diffusion coefficient and the consequences for the PSH. Furthermore, the use of sufficiently high voltages reveals contributions of varying strength for momentum-dependent spin precession due to diffusive transport on the one hand and due to ballistic drift on the other. It could be shown by Altmann *et al.* (2016) that the spin precession angle that stems from the cubic Dresselhaus parameter is bigger by a factor of two for drifting electrons than for diffusing ones. As a consequence, in this regime a temporal spin precession appears even in the absence of external magnetic fields. From the related precession frequency the cubic Dresselhaus parameter β_3 becomes accessible. Here, the underlying theory is further validated and used to complete the parameterization of the GaAs sample with the β_3 parameter.

Generally, it is assumed that the spin polarization is bound to a Gaussian distribution of photocarriers which immediately start to drift in an applied electric field after excitation at the $\mathbf{\Gamma}$-point. Since the utilized electric fields of up to $\sim 15\,\mathrm{V/cm}$ are homogeneous it is reasonable to assume a uniform movement of the Gaussian distributed electron package. This package undergoes an unperturbed simultaneous diffusion in the rest-frame of the package. A time sequence of 2Dmaps, capturing the temporal evolution of such a drifting persistent spin helix (DPSH), is depicted in Fig. 3.7. Each of the 2Dmaps shows the appearance of

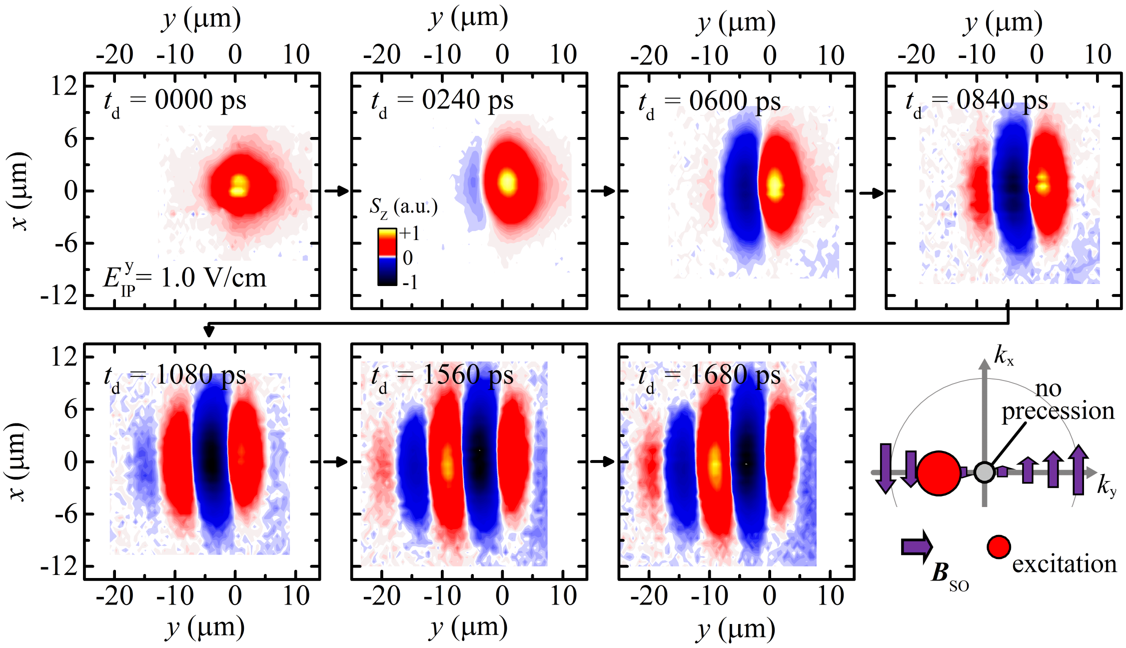

Fig. 3.7: Appearance of the DPSH (drifting persistent spin helix). Series of false-color 2Dmaps, tracing the spatial expansion of a Gaussian distributed spin polarization into a PSH pattern while the entire spin package drifts in an electric field along the y-axis. Black arrows indicate the chronological order of the micrographs. The color scale is individually adapted in each map to increase visibility. In the bottom right corner, the effective magnetic field distribution in k-space is schematically shown.

the DPSH at a certain point in delay time. The formation of the characteristic PSH stripe pattern is clearly visible while the center of spin polarization drifts towards negative y-values due to a positive electric field of $E_{\mathrm{IP}}^{\mathrm{y}} = 0.91\,\mathrm{V/cm}$. Comparing the DPSH series with the stationary PSH in Fig. 3.2 (a), it is apparent that the DPSH features a higher number of oscillations. In the plots up to five red or blue stripes for high delay times are visible while only three distinct stripes can be identified in the purely diffusive PSH. This observation points at an enhanced diffusion coefficient which spreads the Gaussian envelope further in the DPSH case. This presumption is, indeed, confirmed by the data analysis conducted below where the quality of fitting is substantially enhanced due to the elevated number of detectable oscillations along the y-axis.

The DPSH along the y-axis: The time evolution of the DPSH is mapped out as spatiotemporal false-color plot in Fig. 3.8 (a) for a constant electric field of $E_{\mathrm{IP}}^{\mathrm{y}} = 1.51\,\mathrm{V/cm}$. The plot shows the formation of oscillations induced by effective magnetic fields and a continuous shift of the spin package towards negative y-values with delay time. The center position of the spin distribution, given by the y_{c} parameter of the fit function, is marked by a black, dashed line and suggests a shift of $\sim 17\,\mu\mathrm{m}$ over the time of measurement.

Furthermore, there is a clearly visible tilt of the individual stripes highlighted by five parallel dashed lines in grey color. Such a tilt implies a slowly rotating spin orientation with a temporal, angular frequency ω_c for a fixed spatial position. This is noteworthy, as a fundamental feature of the PSH is its constant precession phase for a certain point in space, being responsible for the formation of the unidirectional spin wave pattern. The tilt is preserved even for large delay times and thus the decrease of the spin precession length as a consequence of the finite-spot size effect can be ruled out as possible explanation (cf. Eq. (1.36)). In the following it will be confirmed that the tilt can be modeled as a temporal precession frequency in addition to the already described spatial precession. For this purpose, the introduction of a slightly changed fit function is favorable in order to quantify the qualitatively described effect. For this purpose, the cosine argument of the former fit function is rearranged to read

$$S_z(y) = A_0 \cdot e^{-4\ln(2)(y-y_c)^2/w^2} \cdot \cos\left(\frac{2\pi}{\lambda_{\mathrm{so,y}}} \cdot y + y_1'\right) \tag{3.11}$$

which allows for the study of the cosine phase y_1' independently from $\lambda_{\mathrm{so,y}}$ while all other parameter maintain their original meaning. Figure 3.8 (e) shows an exemplary cutout line from the spatiotemporal micrograph in panel (a) at $t_d = 1758\,\mathrm{ps}$ together with a best fit to Eq. 3.11. Employing the fit function results in an excellent coincidence of the theory transient and the experimental data points.

Individual analysis of all available line scans in panel (a) assembles the data depicted in panel (c) where the center position y_c of the Gaussian envelope reveals a linear dependence on time. This trend is readily explained by a constant drift velocity $v_{\mathrm{dr,y}} = \mathrm{d}y_c/\mathrm{d}t$ enforced on all spin carrying electrons by the electric field. The slope, extracted by a best linear fit to the data, implies a drift velocity of 9860 m/s which is a minute contribution to the kinetic energy of the electrons when compared to the Fermi velocity of 128.4 km/s. Given the applied electric field strength electron mobility $\mu_e = 6.5 \times 10^5\,\mathrm{cm}^2/\mathrm{Vs}$ is calculated, exceeding the value provided from magneto-transport measurements by a factor ~ 2.6 (cf. Table 2.1). This discrepancy is accounted for by the strong influence of the back gate voltage that is discussed in [51]. Later in this section the mobility is extracted from measurements with variable fields, allowing for a more detailed discussion.

The focus shall now be redirected to the aforementioned tilt of the DPSH stripes in the spatiotemporal map. For a thorough understanding of this effect the electron transport due to diffusion and due to drift has to be distinguished. The following considerations are based on a publication of Altmann *et al.* [54]. To begin with, it is favorable to calculate the average, effective magnetic field $\langle \boldsymbol{B}_{\mathrm{so}} \rangle$ seen by a propagating electron spin, starting from $t_d = 0\,\mathrm{ps}$ and $(x, y) = (0, 0)\,\mu\mathrm{m}$. This effective field yields the angle of precession accumulated during the diffusive propagation of the electron towards a point in space given by $\hbar \boldsymbol{k}_{\mathrm{dif}}/m^* \cdot t_d$. Here, the virtual wave vector $\boldsymbol{k}_{\mathrm{dif}} = k_{\mathrm{dif}}[\cos(\phi_0), \sin(\phi_0)]$ represents an average over all sampled wave vectors along the diffusive random walk. Such a random walk is shown schematically in Fig. 3.8 (c) as an inset where ϕ_0 is the angle between the wave vector and the x-axis. In order to achieve a net movement, spins need to sample $\boldsymbol{k}_{\mathrm{dif}}$ with an increased probability compared to

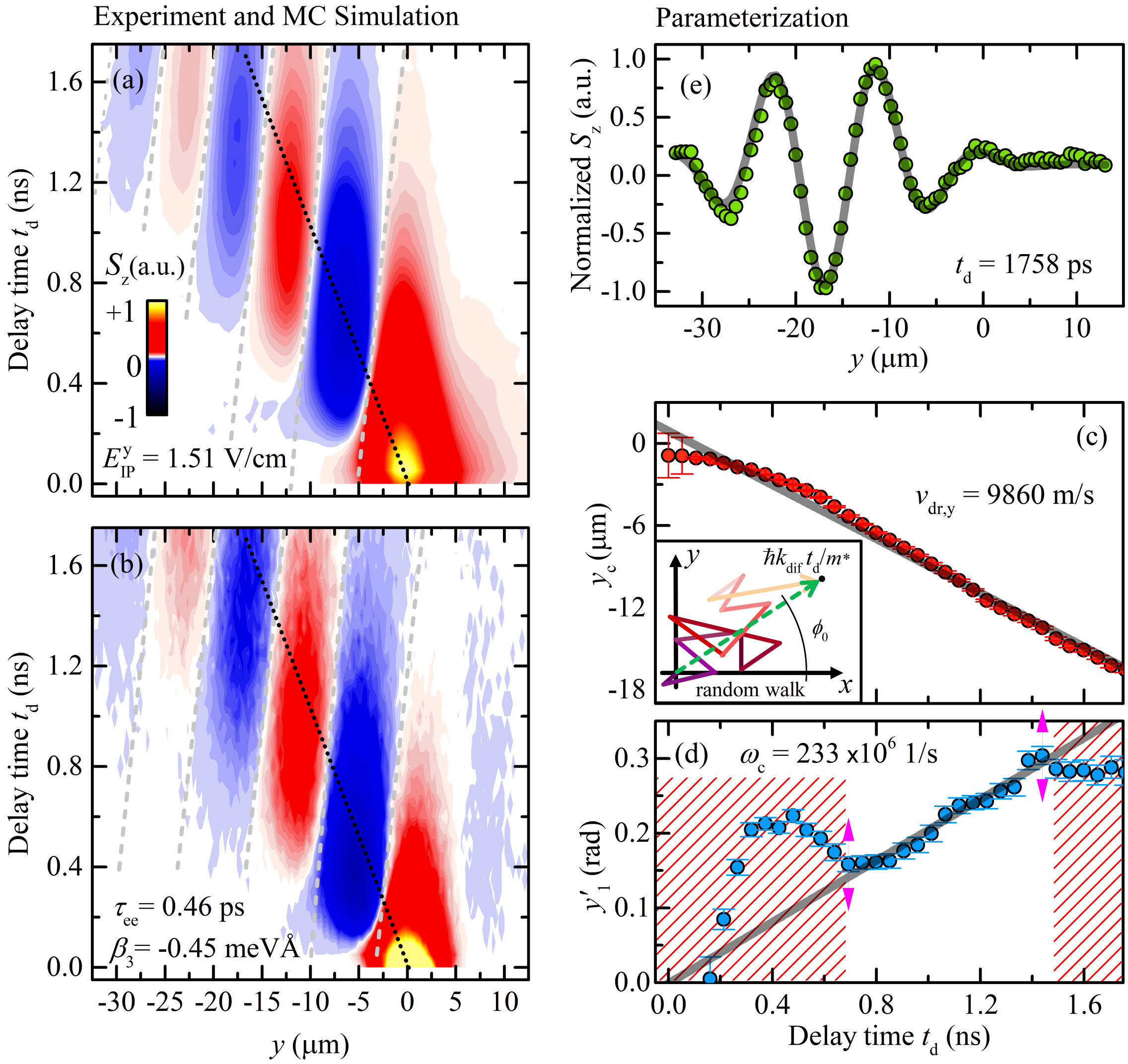

Fig. 3.8: Spatiotemporal appearance and parameterization of the drifting PSH for an applied field of $E^{y}_{\mathrm{IP}} = 1.51\,\mathrm{V/cm}$. **(a)** False-color representation of a DPSH transported along the black dashed line, exhibiting a drift induced tilting of stripes indicated by grey dashed lines. **(b)** Simulation based on the MC method. **(c)** Center position y_c of the Gaussian envelope and respective best linear fit. All data points result from independent fits of the spatiotemporal data in (a) exemplified by the single line scan depicted in panel **(e)**. An inset illustrates a diffusive random walk of an electron in two dimensions. **(d)** Time-dependent cosine phase parameter of the fit function, exhibiting a linear trend in the area which is not hatched. A best linear fit reveals the temporal precession frequency ω_c.

other wave vectors which occur along the random walk. The corresponding weighting function $f(\theta)$ is approximated by

$$f(\theta) = \frac{2k_{\mathrm{dif}}}{k_{\mathrm{F}}} \cos(\theta - \phi_0) + 1 \tag{3.12}$$

where θ represents the angle in between x-axis and $\boldsymbol{k} = k[\cos(\theta), \sin(\theta)]$, following the notation introduced in the Theoretical Background Chapter 1.3.4. The weighting function is justified by the fact that it fulfills the relation

$$\frac{1}{2\pi}\int_0^{2\pi} \boldsymbol{k}\cdot f(\theta)\mathrm{d}\theta = \boldsymbol{k}_{\mathrm{dif}} \tag{3.13}$$

which confirms $\boldsymbol{k}_{\mathrm{dif}}$ as the desired expectation value. In a next step, the correlation of $\boldsymbol{k}$ with the effective magnetic field $B_{\mathrm{so}}(\boldsymbol{k})$ given in Eq. (1.32) is calculated to learn about the averaged effective magnetic field seen by a diffusing electron spin. This calculation reads

$$\langle \boldsymbol{B}_{\mathrm{so}}\rangle = \frac{1}{2\pi}\int_0^{2\pi} \boldsymbol{B}_{\mathrm{so}}(\boldsymbol{k}+\boldsymbol{k}_{\mathrm{dr}})\cdot f(\theta)\mathrm{d}\theta \tag{3.14}$$

and includes the additional wave vector contribution $\boldsymbol{k}_{\mathrm{dr}}$ that arises from drift in an external electric field. If drift and diffusion are taken into account only along the y-axis, the components $k_{\mathrm{dr,x}} = 0$ and $k_{\mathrm{dif,x}} = 0$ are set to zero for simplicity (cf. [54] for a more general case). Subsequently, Eq. (3.14) can be calculated and the result is given by

$$\langle \boldsymbol{B}_{\mathrm{so}}\rangle = \frac{2(\alpha+\beta_1)}{g\mu_{\mathrm{B}}}(k_{\mathrm{dif,y}}+k_{\mathrm{dr,y}}) - \frac{2\beta_3}{g\mu_{\mathrm{B}}}(k_{\mathrm{dif,y}}+2k_{\mathrm{dr,y}}) \tag{3.15}$$

in an almost identical shape as presented for $\boldsymbol{B}_{\mathrm{so}}^{(1)}$ before in Eq. (3.2) provided

$$\begin{pmatrix} k_{\mathrm{x}} \\ k_{\mathrm{y}} \end{pmatrix} = \begin{pmatrix} k_{\mathrm{dif,x}}+k_{\mathrm{dr,x}} \\ k_{\mathrm{dif,y}}+k_{\mathrm{dr,y}} \end{pmatrix}. \tag{3.16}$$

A closer look to the second term of Eq. (3.15) reveals that the drift contribution of β_3 to the effective magnetic field is twice as high as the contribution from diffusion. This difference in between drift and diffusion is at the origin of the tilted stripes observed in Fig. 3.8 (a) and can be explained as follows. The spatiotemporal map shows the DPSH as the result of a spin distribution which spreads out in space due to simultaneous diffusion and drift. Accordingly, the expected center position of spin polarization is given by the drift velocity and the delay time. Electrons which arrive at this center position earlier (later) must have additionally diffused parallel (anti-parallel) to the direction of drift. This considerations lead to the fact that the ratio of the drift and the diffusion momentum depends explicitly on the moment in time when an electron arrives at a fixed position. Due to Eq. (3.15) it has to be assumed that this temporal difference in the ratio of drift and diffusion wave vectors translates into a temporal difference of the average effective magnetic field seen by the electron. This is equivalent to a temporal variation of the spin precession angle at any fixed position. Such a variation manifests as a tilt of the stripes that indicates a temporal spin precession similar to the case where magnetic fields are applied externally. As a result, the effective magnetic field given in Eq. (3.15) can be transferred into a position- and time-dependent precession angle that can be set equal to the cosine argument of the fit function in Eq. (3.11). Accordingly, the expression

$$y_1' = -\frac{2m^* v_{\mathrm{dr,y}}}{\hbar^2}\beta_3\cdot t_{\mathrm{d}} \tag{3.17}$$

is found and enables the direct extraction of β_3 from the fit parameter y_1' given that the drift velocity is known. The linear time dependence of y_1' predicted in Eq. (3.17) is equivalent to a temporal precession frequency $\omega_\mathrm{c} = -2m^* v_\mathrm{dr}\beta_3/\hbar^2$ that can be extracted from the experimental data.

By analyzing the spatiotemporal data presented in Fig. 3.8 with the fit function in Eq. (3.11), the time-dependent data for y_1' in panel (d) are obtained. A clear linear trend of the data is given only for a limited time period around 1 ns and a linear fit is performed to this data, leaving out the hatched data points. The non-linear behavior of the data in the hatched region is attributed to poor fitting quality that arise from insufficient oscillations at short delay times. As a result of the linear fit, a frequency of $\omega_\mathrm{c} = 0.233 \times 10^9\,\mathrm{s}^{-1}$ is obtained, implying a value of $\beta_3 = 0.140\,\mathrm{meV\AA}$. This number is in good agreement with the predicted theory value $0.135\,\mathrm{meV\AA}$ obtained by inserting the electron density of $0.8 \times 10^{11}\,\mathrm{cm}^{-2}$, taken from PL measurements at $-1.00\,\mathrm{V}$ back gate voltage, into formula (1.29).

Having gathered a full set of parameters, a MC simulation can be created and compared to the experiment. For this purpose, Fig. 3.8 (b) depicts MC data created for a diffusion coefficient of $D_\mathrm{s} = 100\,\mathrm{cm}^2/\mathrm{s}$, implying a scattering time of $\tau_\mathrm{ee} = 0.46\,\mathrm{ps}$. This value of D_s can be extracted from the linear expansion of $w^2(t_\mathrm{d})$ in the spatiotemporal experiment analogous to Fig. 3.3 (b). It is noteworthy, that this spatial spreading proceeds about two times faster than observed in measurements without electric field. Indeed, further experiments with a variable electric field strength, discussed below, confirm such a tuning of the diffusion coefficient and an in-depth discussion follows later in this section around Fig. 3.11. There the trend is attributed to a combination of heating and a novel mechanism called convectional diffusion. The tilted stripes are discussed above as the result of different contributions of β_3 to the electron movement due to either diffusion or drift. The MC simulation provides a remarkable prove of this theoretical model as the tilt of stripes is well reproduced. However, the value of β_3 which gives the best possible match with the experiment is $0.45\,\mathrm{meV\AA}$ which is approximately four times higher than the experimental value. Considering the limited data range of panel (d) that was used to extract β_3, the discrepancy arises possibly due to a high uncertainty in the fitting. This observation is addressed further in the next paragraph where variable electric fields are investigated.

The DPSH along the y-axis, variable fields: The results presented for the DPSH so far are obtained from experiments with constant electric field. In contrast, the following data are supposed to resolve the dependence of the PSH on variable electric fields. In this context, special attention is paid to the behavior of the diffusion coefficient and the SO coupling parameters. For this purpose, the false-color plot in Fig. 3.9 (a) illustrates a set of $S_\mathrm{z}(y)$ line scans taken along the y-axis for a variety of electric fields E_IP^y. All measurements are performed with a fixed delay time of 1525 ps, allowing for the best trade-off between signal strength and an advanced PSH evolution. The plot reveals a clearly increasing spatial shift of the spin distribution towards negative (positive) y-values with raising the positive (negative) electric field strength. This shift is explained by the linear dependence of the drift velocity $v_{\mathrm{dr,y}} = -\mu_{\mathrm{e}} E_{\mathrm{IP}}^{\mathrm{y}}$ on the applied field. The false-color plot appears to exhibit central inversion symmetry. This is confirmed by extracting the y_{c} parameter for each line-scan from fits to Eq. (3.11) as exemplified in panel (b) for a cutout line from (a) at $E_{\mathrm{IP}}^{\mathrm{y}} = -2.0\,\mathrm{V/cm}$. Here, the y_{c} parameter represents the center of the spin ensemble and can be translated into the drift velocity via $v_{\mathrm{dr,y}} = y_{\mathrm{c}}/(1525\,\mathrm{ps})$. The resulting data on $v_{\mathrm{dr}}(E_{\mathrm{IP}}^{\mathrm{y}})$ are depicted in panel (e) and a best linear fit yields a mobility of $0.38 \times 10^6\,\mathrm{cm^2/Vs}$ comparable with the value $0.25 \times 10^6\,\mathrm{cm^2/Vs}$ that is given in Table 2.1 as a result of magneto-transport measurements for zero back gate voltage. The difference in both values is most likely assigned to a variation of mobility caused by the applied back gate voltage of $-1.00\,\mathrm{V}$. A strong influence of the gate on the mobility is reported in literature [51] for similar structures, however, with an opposite trend to the one seen here. Besides this, the mobility can be estimated from sample-specific parameters by employing the relation $\mu_{\mathrm{e}} = l_{\mathrm{QW}}/(n_{\mathrm{e}} R_{\mathrm{QW}} e b_{\mathrm{QW}})$ where $R_{\mathrm{QW}} \sim 5\,\mathrm{k\Omega}$ is the resistance of the QW [132]. This calculation estimates a value of $1.0 \times 10^6\,\mathrm{cm^2/Vs}$ which supports rather the high mobility extracted from tracing the spin polarization pattern.

In accordance with Eq. (3.17) the value of β_3 is accessible from the linear dependence of the cosine offset parameter y_1' on the drift velocity if the delay time is fixed. Panel (g) of Fig. 3.9 presents the field dependence of y_1' for which the field strength is converted into drift velocity, using the results of panel (e). Taking into account the uncertainty of the cubic Dresselhaus parameter, encountered in the spatiotemporal measurement and simulation (cf. Fig. 3.8: $\beta_3 = (0.1 - 0.45)\,\mathrm{meV\AA}$), the analysis of y_1' has to be executed with caution. The trend is linear on first sight, confirmed by a linear fit of the whole data set depicted in the panel. However, more accurately two linear regimes can be distinguished in the plot and evolve symmetrically around zero velocity. One regime represents a strong increase in the range up to $1500\,\mathrm{m/s}$ while a second regime is identified for higher velocities with a comparably lower slope. Two separate fits allow for the estimation $\beta_3 = (0.15 \pm 0.08)\,\mathrm{meV\AA}$ with a high statistical error. Despite this quantification, the ambiguous behavior of y_1' and the strong dissimilarity of β_3 in the MC simulation and the experiment in Fig. 3.8 points at a deficiency of the applied fit model. It cannot be excluded that the limited number of oscillations causes errors in the extraction of the y_1' parameter. Additionally, it is expected that the application of current to the system induces heating of the electron gas, causing a transition to a non-degenerate gas. In this case, the Fermi energy has to be replaced by a higher, average kinetic energy $\langle E \rangle$ due to Fermi smearing. This effect is elaborated thoroughly around formula Eq. (3.19) from where it can be seen that heating results in an increase of β_3. This finding is in contradiction with the slope in panel (g) that rather suggests a decrease of β_3 for increasing voltages.

Fitting Eq. (3.11) to the field resolved data traces the width w of the drifting spin polarization over the time of measurement. Moreover, the width of the spin distribution at $0\,\mathrm{ps}$ is not affected by any electric fields and thus w_0 is known from Table 3.1 to be constant. Hence, the diffusion coefficient can be estimated from the expression $w^2 = 16\ln(2) D_{\mathrm{s}} \cdot 1525\,\mathrm{ps} + w_0^2$. The corresponding data for D_{s} are presented in panel (c) and a strong enhancement of the dif-

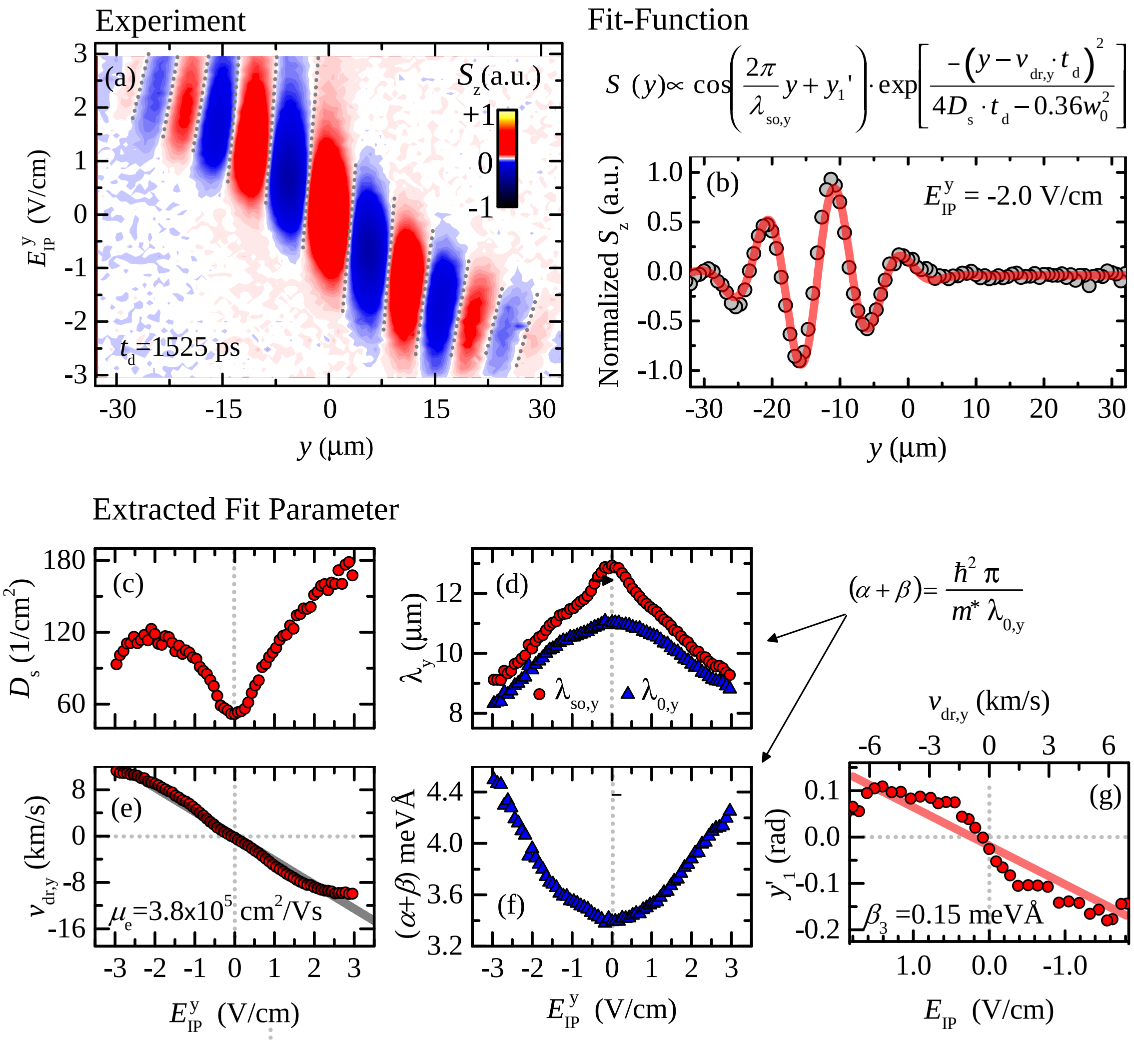

Fig. 3.9: Effect of variable in-plane electric fields on the PSH for a fixed delay time of 1525 ps. **(a)** False-color representation of line-scans along the y-axis for a variety of in-plane electric fields along the same axis. Dashed lines in grey color visualized a shortening of the precession length confirmed in (d). **(b)** Exemplary curve fit for a cutout line from (a) a $E^{\mathrm{y}}_{\mathrm{IP}} = -2.0\,\mathrm{V/cm}$. **(c-e,g)** Dependence of fit parameters on the applied electric field strength. **(f)** Tunability of summed Rashba and Dresselhaus parameters with electric field derived from the spin precession length given as blue data points in (d).

fusion with rising field strength is monitored for drift in both directions along the y-axis. For positive fields D_{s} increases monotonously to $180\,\mathrm{cm}^2/\mathrm{s}$ while negative fields raise the diffusion coefficient to a maximum and fields below $-2\,\mathrm{V/cm}$ lead to a decrease. The increased diffusion is in agreement with the value of $D_{\mathrm{s}} = 100\,\mathrm{cm}^2/\mathrm{s}$ that was needed in the MC simulation of Fig. 3.8 to reproduce the experiment at $1.51\,\mathrm{V/cm}$. The origin of this peculiar tunability of diffusion is further discussed in the end of this section around Fig. 3.11 where an in-depth explanation is developed.

Furthermore, the knowledge about the variability of D_{s} is important for the correct extraction of $(\alpha+\beta)$ from the precession length $\lambda_{\mathrm{so,y}}$ in panel (d). The experimental data reveal a clear, symmetric trend towards a shorter precession length $\lambda_{\mathrm{so,y}}$ for increasing field strength visible as well in the false-color plot where dashed grey lines are drawn for visual guidance. This finding is of peculiar interest as it suggests a variation of the Rashba and Dresselhaus parameters by in-plane electric fields. In the first place, the symmetry of the data around zero field implies that the trend is not an artifact that stems from short circuits in the sample, biasing the back gate voltage. This is crucial as the aforementioned Fig. 3.5 (g) has shown the impact of back gate voltage on the SO coupling parameters. An cross-coupling of U_{IP} and U_{IP} could result in a simultaneous detuning of the gate voltage with changing the in-plane electric field. However, in such a case the wiring of the sample would lead to a non-symmetrical behavior of $\lambda_{0,\mathrm{y}}$. Consequentially, the decrease of the precession length is claimed to emerge from real changes in the SO coupling parameters.

In a next step, it has to be differentiated in between $\lambda_{\mathrm{so,y}}$ and $\lambda_{0,\mathrm{y}}$. The former parameter states the transient wavelength of the spin polarization which still develops into a PSH and is therefore a time-dependent entity while the latter one describes the stationary PSH mode for $t_{\mathrm{d}} \to \infty$. The relation of both parameters is revived from Eq. (3.4) as

$$\lambda_{\mathrm{so,y}}(t) = \lambda_{0,\mathrm{y}} \left[1 + \frac{w_0^2}{16 \ln(2) D_{\mathrm{s}} t}\right] \tag{3.18}$$

where the diffusion coefficient strongly influences the temporal evolution of the precession length. As D_{s} itself is affected by the electric field it has to be ruled out that the observed change of $\lambda_{\mathrm{so,y}}$ is a secondary effect caused by variations of the diffusion. For this purpose, $\lambda_{0,\mathrm{y}}$ is calculated and plotted next to the experimental precession length $\lambda_{\mathrm{so,y}}$ in panel (d). It is apparent that the resulting λ_0 remains strongly field-dependent and subsequently the sum of Rashba and Dresselhaus parameters can be calculated with Eq. (3.4) and is depicted in panel (f). From this data a significant increase of $(\alpha + \beta)$ from 3.35 meVÅ up to $\sim$ 4.4 meVÅ at an absolute field strength of about 3 V/cm is monitored. As an unwanted tuning of the gate voltage is ruled out, it is assumed that the out-of-plane field and thereby α is constant. Consequently, it is concluded that the remaining parameters β_1 and β_3 are affected indirectly by the applied in-plane bias. The Theoretical Background Section of this thesis elaborates on the origin of β_1 from the band structure alignment which is unlikely altered by the utilized fields. On the contrary, the cubic Dresselhaus parameter β_3 is known to depend on the Fermi energy (cf. Eq. (1.29)), that might undergo a significant change if the 2DEG is transitioned from a degenerate to a non-degenerate gas. In this case, the Fermi energy must be replaced by an averaged energy $\langle E \rangle$ which takes into account a smearing of the Fermi edge and includes a temperature dependence that reads

$$\beta_3 = \gamma_{\mathrm{D}} \frac{m^* E_{\mathrm{F}}}{2\hbar} \quad \text{with} \quad E_{\mathrm{F}} \quad \rightarrow \quad \langle E \rangle (T_{\mathrm{e}}) = E_{\mathrm{F}} \cdot \frac{1}{1 - e^{-E_{\mathrm{F}}/k_{\mathrm{b}} T_{\mathrm{e}}}} \tag{3.19}$$

analogous to the dependence of the Fermi-Dirac statistic on the electron temperature T_{e}. Such an approach has been successfully applied in literature [55], however, is incapable to explain an increase of $(\alpha + \beta)$. From Eq. (3.19) it is obvious that heating will inevitably go together with an increase of $\langle E \rangle$, resulting in a growth of β_3. At the same time, an increased β_3 will always decrease the Dresselhaus parameter $\beta = \beta_1 - \beta_3$ and must lead to a reduced $(\alpha + \beta)$ in contrast to the data of Fig. 3.9 (f). Besides this, the absolute change of β_3, needed to reproduced the variation of $\Delta(\alpha + \beta) \approx 1\mathrm{meV\AA}$, would require a temperature variation of several hundreds of Kelvin. Later in this chapter around Fig. 3.11, the possibility of electron gas heating up to 350 K is discussed, implying a heat induced change of $\Delta\beta_3 \approx 1.5\,\mathrm{meV\AA}$.

The DPSH along the X-axis, constant and variable fields: Until here, in-plane electric fields have been established as a powerful control knob for the PSH. The presented experiments are conducted foremost with fields applied along the y-axis where $\lambda_{0,\mathrm{y}}$ is small enough to detect multiple spin oscillations within the spatial window of measurement. The Hall bar geometry of the sample (cf. Fig. 2.3) facilitates the application of in-plane bias as well along the x-axis. This is of particular interest since in this direction, so far, no significant precession of the spin is observed due to a much longer $\lambda_{\mathrm{so,x}}$. An example for this is the spatiotemporal false-color plot in Fig. 3.2 (b). However, signatures of the effective magnetic field can be revealed by the application of magnetic fields, yielding $(-\alpha + \beta) = 1.15\,\mathrm{meV\AA}$ which corresponds to a spin precession length of $\lambda_{0,x} = 32.5\mu\mathrm{m}$ for the x-axis. Therefore, the absence of oscillating features is not surprising as the spin diffusion length $L_\mathrm{s} = 3.3\,\mu\mathrm{m}$ is smaller by an order of magnitude. In order to, nevertheless, access information about the PSH from the x-axis it is highly beneficial to transport the spins by in-plane fields and thus cover the distances needed to observe oscillations.

In Fig. 3.10 (a) it is shown that this approach indeed reveals a spin polarization wave. In this measurement the spin ensemble is dragged towards negative x-values due to a positive field of strength $E_{\mathrm{IP}}^{\mathrm{x}} = 6.95\,\mathrm{V/cm}$, imposing a drift velocity of $v_{\mathrm{dr,x}} = -22.6\,\mathrm{km/s}$. Analogous to previous y-axis measurements, $v_{\mathrm{dr,x}}$ is extracted from the dependence of the Gaussian center parameter x_c on delay time. This linear dependence is indicated as black dashed line in panel (a). The employed fit function for x-axis line scans is motivated from Eq. (3.11) and reads

$$S_\mathrm{z}(x) = A_0 \cdot e^{-4\ln(2)(x-x_\mathrm{c})^2/w^2} \cdot \cos\left(\frac{2\pi}{\lambda_{\mathrm{so,x}}} \cdot x + x_1'\right) \tag{3.20}$$

where the cosine argument has been slightly rearranged compared to Eq. (3.8). Remarkably, the trend of an enhanced diffusion coefficient, previously seen to increase significantly with the applied field strength along the y-axis, is confirmed in panel (a). Due to the relatively high fields, needed to induce spin oscillation along the x-axis, the dependence of D_s shown in Fig. 3.9 can be extended. For an applied field of 6.95 V/cm a diffusion coefficient of $D_\mathrm{s} = 374\,\mathrm{cm}^2/\mathrm{s}$ is observed, corresponding to a seven-fold higher value than in the absence of field. The diffusion coefficient together with all other parameters extracted from 3.10 (a) are confirmed when used to create a MC simulation. In panel (b) the resulting plot is depicted where a striking match with the experiment is achieved.

On the right hand of Fig. 3.10, a selection of measurements and extracted parameter in

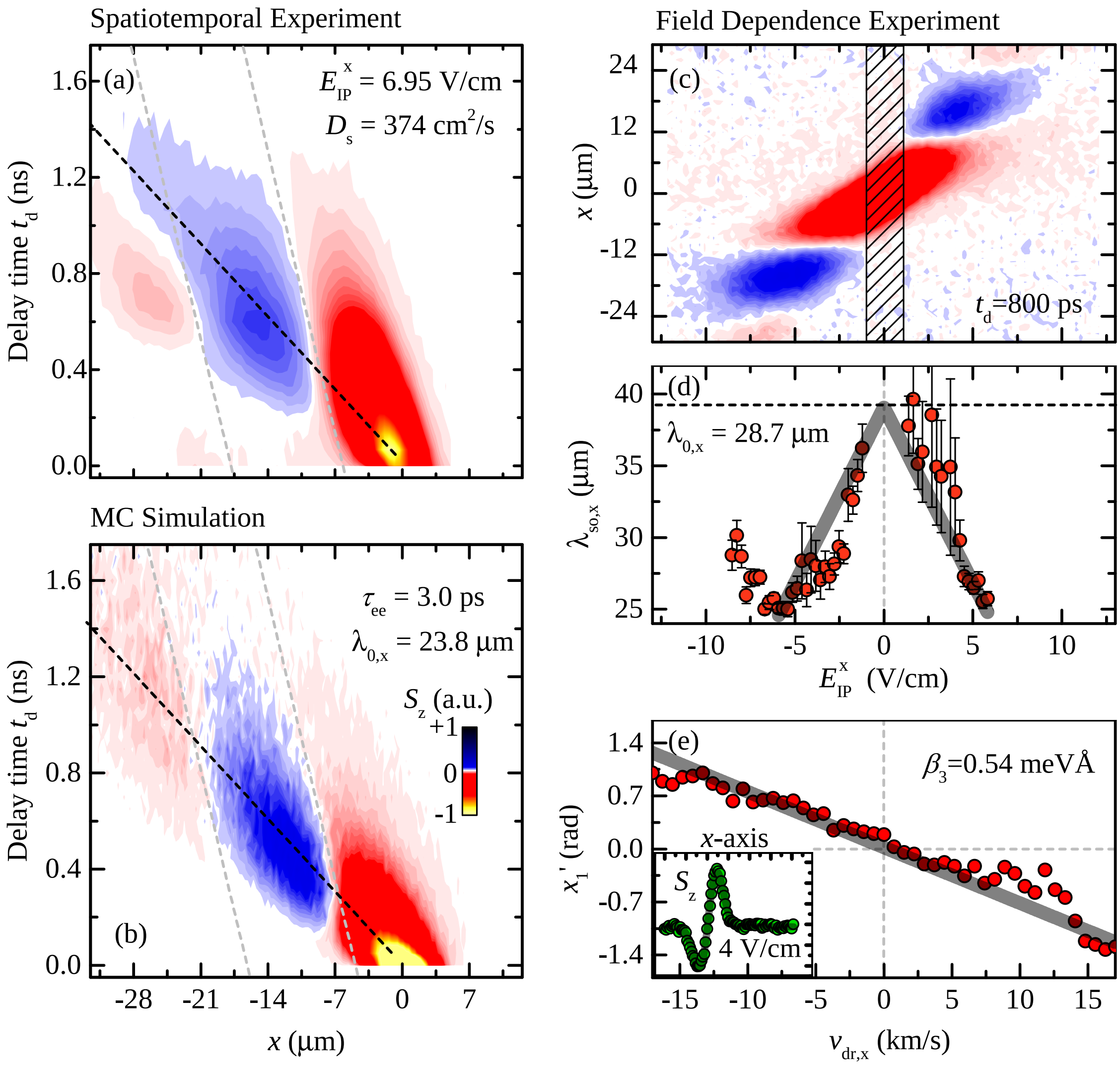

Fig. 3.10: Analysis of the DPSH evolution recorded along the x-axis. **(a)** Spatiotemporal measurement as false-color representation for field applied along the x-axis and **(b)** corresponding MC simulation. (c) Field dependence of the DPSH at fixed delay time and for $y = 0\,\mu$m depicted as false-color plot. Fitting within the hatched area yields insufficient results due to a lack of oscillating signal. (d-e) Parameter extracted from the false-color map above, representing the spin precession length caused by the difference of Rashba and Dresselhaus parameter $(-\alpha + \beta)$ in (d) and the cosine offset parameter in (e). The inset in (e) shows an exemplary fit of a cutout line from (c).

dependence of a variable field $E^{\mathrm{x}}_{\mathrm{IP}}$ is compiled. Panel (c) represents a false-color plot that depicts the temporary state of the PSH at $t_{\mathrm{d}} = 800\,\mathrm{ps}$ for a field range of $\pm 12\,\mathrm{V/cm}$ plotted along the x-axis. The plot can be understood as an equivalent to the y-axis measurement in the foregoing figure. For the chosen delay time, oscillations do not become visible for fields lower than $|E^{\mathrm{x}}_{\mathrm{x}}| = 1.35\,\mathrm{V/cm}$. This limit is imposed by the fixed delay time which cannot be arbitrarily increased because at some point the electrons starts to drift beyond the spatial window of measurement. By fitting function Eq. (3.20) to $S_{\mathrm{z}}(x)$ the field dependence of the spatial precession length $\lambda_{\mathrm{so,x}}$ is revealed. Here, the lack of oscillating signal in the hatched region in panel (c) prevents reasonable fitting for the concerned fields. An example of successful fitting is given in the inset of panel (e). The generally good agreement of fit and data warrants a reasonable extraction of the fit parameters. Nevertheless, the fitting error of the extracted parameters suffers from less pronounced oscillations when compared to y-axis data.

Similar to the observed behavior of $\lambda_{\mathrm{so,y}}$ (cf. Fig. 3.9) a downward trend of $\lambda_{\mathrm{so,x}}$ can be reported for rising field strengths. The finding of a decreasing precession length along both axes supports the assumption that a change in α can be ruled out as it enters into $(-\alpha+\beta)$ along the x-axis with negative sign. This negative sign would imply an opposite trend for $\lambda_{\mathrm{so,x}}$ when compared to the y-axis where $\lambda_{\mathrm{so,y}}$ is determined by $(\alpha+\beta)$. Along the y-axis a symmetric and linear decrease of $\lambda_{\mathrm{so,y}}$ with absolute field strength is visible, starting from a maximum at zero field (cf. Fig. 3.9 (d)). Accordingly, the corresponding trend along the x-axis is modeled with an absolute value function $\lambda_{\mathrm{so,x}}(E_{\mathrm{IP}}^{\mathrm{x}}) = A_1 \cdot E_{\mathrm{IP}}^{\mathrm{x}} + \lambda_{\mathrm{so,x}}(0\,\mathrm{V/cm})$, allowing for an indirect approximation of $\lambda_{\mathrm{so,x}}(0\,\mathrm{V/cm})$ which cannot be directly accessed. The best fit which is plotted on top of the data points in (d) poses $\lambda_{\mathrm{so,x}}(0\,\mathrm{V/cm}) = 39.08\,\mu\mathrm{m}$ which transforms into $\lambda_{0,\mathrm{x}} = 28.7\,\mu\mathrm{m}$, taking into account the diffusion coefficient for $E_{\mathrm{IP}}^{\mathrm{x}} = 0\,\mathrm{V/cm}$ that is contained in Table 3.1. This estimation of $\lambda_{0,\mathrm{x}}$ is in good agreement with $(-\alpha+\beta) = 1.15\,\mathrm{meV\AA}$ determined from measurements with in-plane magnetic fields where a value of $\lambda_0 = 32.5\,\mu\mathrm{m}$ is found. Another parameter that provides valuable information about the SO coupling is the cosine offset parameter for the x-axis presented in panel (e). In order to show x_1' in dependence of drift velocity, $v_{\mathrm{dr,x}}$ is extracted from the linear dependence of the Gaussian center position x_{c} on delay time, suggesting a constant mobility throughout the field range (data not shown). Here, the $E_{\mathrm{IP}}^{\mathrm{x}}$, i.e., drift velocity dependence of x_1' enables the extraction of β_3. For this purpose, the same model is used that was previously developed for the tilted stripes in spatiotemporal maps along the y-axis. As discussed around Fig. 3.8 this tilt is caused by an imbalance in precession due to drift and diffusion. In the preceding analysis the drift velocity dependence of the cosine offset parameter, given in Eq. (3.17) was discussed. As a result, a significant discrepancy of experiment $\beta_3 \sim 0.14\,\mathrm{meV\AA}$ and MC simulation $\beta_3 \sim 0.45\,\mathrm{meV\AA}$ is found for the y-axis. The analogous data along the x-axis show a clearly linear behavior and, indeed, the extracted value of $\beta_3 = 0.54\,\mathrm{meV\AA}$ is closer to the MC simulation. This improvement at the $x-$axis where the fit procedure is more challenging is attributed to a weak influence of the finite-spot size effect. This effect causes a strong alteration of λ_{so} with delay time while the broad eigenmode spectrum of the Gaussian distribution develops into a single mode PSH (cf. discussion below Eq. (3.4)). Due to the wider precession length this effect is not so distinct along the x-axis. Therefore, the extraction of the cosine offset is not strongly perturbed by changes of the cosine frequency which is namely $\lambda_{\mathrm{so,x}}$. In conclusion, the cubic Dresselhaus parameter remains a degree of uncertainty. A combination of values generated from both axis, the MC simulation and the theoretically calculated values provide a range of $(0.29 \pm 0.20)\,\mathrm{meV\AA}$ for β_3. In the corresponding error calculation a stronger weighting

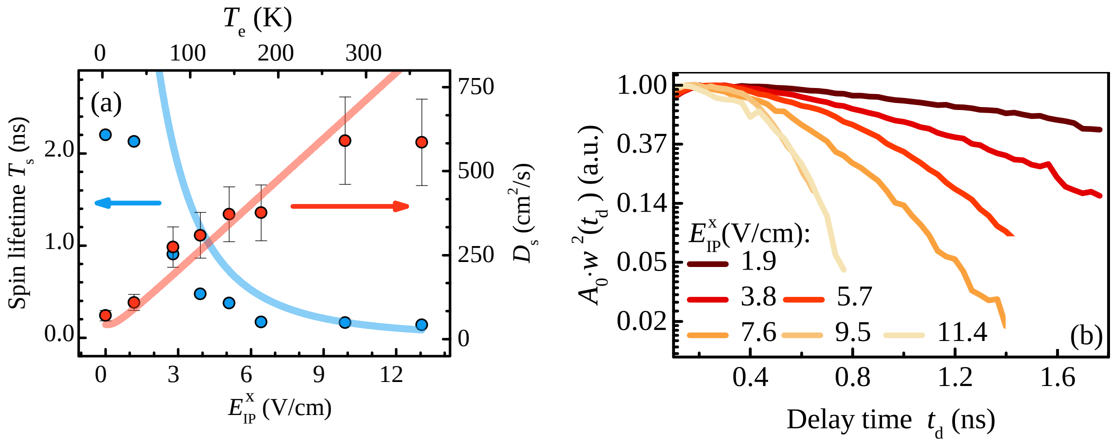

Fig. 3.11: **(a)** In-plane electric field induced enhancement of the diffusion coefficient. Experimental data points in red color are extracted from spatiotemporal measurements and plotted along with a theoretical prediction for D_s based on Eq. (3.21) and an increasing electron temperature as indicated on the top axis. The same panel shows the experimentally obtained PSH lifetime as blue data points extracted from the decaying lines in (b) together with the theory model of Eq. (1.37) which integrates the dependence on the diffusion coefficient. **(b)** Temporal decrease of the amplitude multiplied with the squared FWHM, both obtained as fit parameters from individual spatiotemporal measurements with varying E^x_{IP}.

of the higher values from the x-axis and MC simulation might be worth considering.

In the last part of this section, the observed monotonic increase of the diffusion coefficient caused by raising in-plane electric fields shall be elucidated in more detail. Starting from the spatiotemporal experiment displayed in Fig. 3.8, a diffusion of $D_s = 100\,\mathrm{cm}^2/\mathrm{s}$ is found for measurements with $E^y_{IP} = 1.51\,\mathrm{V/cm}$. This values corresponds to a two-fold enhancement if compared to experiments without in-plane fields. In addition, this effect of electric fields is confirmed by the corresponding MC simulation shown in the same figure. Advanced experiments with a variation of the electric field strength yield a broad tunability of the diffusion coefficient. Here, the diffusive spread can be accelerated by a factor of four as shown in Fig. 3.9 (c). Furthermore, Fig. 3.11 (a) studies the behavior of D_s along the x-axis where stronger fields are required to detect spin precession and consequently the dependence of D_s on the field strength can be extended. The increase of D_s, identified firstly along the y-axis, appears as well in perpendicular direction along the x-axis, excluding the sample geometry as a possible origin of the effect. In panel (a) a non-linear increase of D_s is shown to reach up to $600\,\mathrm{cm}^2/\mathrm{s}$, scaling almost an order of magnitude higher than for the unperturbed PSH if a field of strength $13.3\,\mathrm{V/cm}$ is applied. This effect is not covered by the discussed theory and points at a peculiar, indirect influence of in-plane bias on the diffusion. In the following, an explanation of this effect is based on three independent phenomena that can potentially be responsible for this severe change.

(i) It was discussed already in the context of the cubic Dresselhaus parameter β_3 and Eq. (3.19) that heating of the electron gas has significant impact on the average kinetic energy of the electrons. Such an impact is explained by the transition from Fermi-Dirac statistic to

Boltzmann statistic as the gas becomes non-degenerate. The raising trend of D_s in panel (a) of Fig. 3.11 is compared with a model where the Fermi energy in the expression $D_\mathrm{s} = \tau E_\mathrm{F}/m^*$ is replaced by a temperature-dependent, average kinetic energy. By using Eq. (3.19) the diffusion coefficient can be rewritten as

$$D_\mathrm{s}(T_\mathrm{e}) = \frac{\tau}{m^*} E_\mathrm{F} \cdot \frac{1}{1 - e^{-E_\mathrm{F}/k_\mathrm{B}T_\mathrm{e}}} \tag{3.21}$$

where T_e denotes the electron temperature. In order to connect this model with the experimental data for D_s the electric field given by the x-axis at the bottom of panel (a) is projected on a temperature scale. Subsequently, this temperature scale is added to the top x-axis of the same plot, assuming a linear conversion from field to T_e. The conversion factor is chosen to best reproduce the red colored experimental data points with the resulting model curve depicted in the same color. From this approach, it is estimated that the temperature needs to be raised by $\sim 300\,K$. Such strong heating exceeds observations in similar systems [55; 133–136] and would require elevated energy relaxation times to avoid equilibration with the helium cooled lattice. Since the GaAs sample is a high mobility sample, this is within the range of the possible. A direct estimation of T_e from changes in the PL due to a variation of E_IP, as performed by Kunihashi *et al.* [55], has not been successful. In the present sample such PL measurements are challenging due to data distortion, coming from unwanted PL background of the GaAs substrate. In an alternative approach the electron temperature can be derived from the momentum relaxation time. This time scale is estimated to be $\tau = \mu_\mathrm{e} m^*/e = 13.8\,\mathrm{ps}$, making use of the field independent (cf. Fig. 3.9 (e)) mobility. In a next step, this allows for an estimation of the corresponding energy relaxation time $\tau_\mathrm{E} \sim 138\,\mathrm{ps}$ which is usually an order of magnitude longer than τ [137; 138]. Moreover, the energy relaxation rate can be combined with the acting Coulomb force of the field to estimate the energy deposition into the system. For an exemplary field of $E^\mathrm{x}_\mathrm{IP} = 10\,\mathrm{V/cm}$ this energy is given by $(eE^\mathrm{x}_\mathrm{IP}\tau_\mathrm{E})^2/2m^* = 29\,\mathrm{meV}$ which is equivalent to a temperature of 336 K. This claim is supported by the finding that the energy deposition into the 2DEG during τ_E does not exceed the longitudinal optical (LO) phonon energy $\hbar\omega_\mathrm{LO} = 36.6\,\mathrm{meV}$ [136]. Reaching this energy would lead to a fast transfer of energy from the 2DEG to the lattice and a corresponding drop in the electron temperature.

The relation in between the diffusion coefficient and the spin lifetime $T_\mathrm{s} \propto (D_\mathrm{s})^{-1}$ is known from Section 1.3.5. Therefore, a strong decay of the PSH lifetime with ascending electric field has to be expected as a result of the increasing diffusion coefficient. This trend is, indeed, confirmed by the experiment. In the same plot that shows D_s the lifetime is depicted as blue data points and follows the theoretical prediction shown as blue model curve. The blue curve is derived by inserting the empirically found dependency of D_s on the in-plane electric field into Eq. (1.37). By closer examination the experimental lifetime is found to be even shorter than suggested by the model and the discrepancy is attributed to a simultaneous unbalancing of the Rashba and Dresselhaus SO parameter which have already been shown to be affected by electric field. The lifetime is extracted from the data sets in Fig. 3.11 (b) which represent a measure for the entire degree of coherent spin polarization. The time-dependent lines are obtained from fits of spatiotemporal maps and a subsequent multiplication of each extracted amplitude parameter A_0 with the corresponding squared ensemble width w^2. This method removes the unwanted effect of diffusion from the extracted temporal dependence of A_0 and reveals the pure spin decay that imposes a finite lifetime on the PSH pattern.

Returning to the considerations related to the temperature dependence of D_s it has not been taken into account yet that heating is likely followed by a decrease of the momentum relaxation time τ [125]. Accordingly this decrease must be expected to antagonize the increase in D_s. Hence, contributions beyond heating must be considered in the following to fully explain the substantially enhanced diffusion.

(ii) As discussed in the appendix of this work diffusion is a process triggered by stochastic events of scattering and thus relies on random sampling of different k-states on the Fermi circle. A similar statistical process is expected to occur due to randomly oriented intrinsic electric fields present in the QW sample. These fields add randomly distributed velocity contributions to the Fermi velocity vector of each electron. Such electric fields are caused by spatial inhomogeneities of the QW that locally bend the internal potential. Possible examples are screening due to disordered dopants in the Si-δ of the heterostructure- or growth-dependent variations of the QW thickness, resulting in a local modulation of the band structure. The former proposal can be approximated by an electric field that has a modulation length comparable to the distance in between Si-δ and QW. In the growth protocol this distance is quantified to be $d_\mathrm{si} \approx 100\,\mathrm{nm}$. The choice of this specific dimension is justified by the fact that the near-field order of point-like Coulomb fields is known to decay exponentially in space. The remaining ordering exhibits a similar scale as the distance in between the delta and QW since this length is substantially larger than the average distance in between two dopants. In the case of no in-plane electric fields, the random field seen by the electrons are static which is changed by drift. Drifting electrons feel a varying field as they propagate over the modulation distance of 100 nm. Assuming a drift velocity of $\sim 10\,\mathrm{km/s}$ for moderate applied field strength the corresponding relaxation time can be estimated to be some 10 ps. As a consequence, the influence of randomized fields can be modeled as a convectional diffusion process for clusters of electrons with size $d_\mathrm{si} \times d_\mathrm{si}$, acting in addition to the classical electron diffusion. To get some idea about the extent of this effect the standard equation for two-dimensional diffusion $D'_\mathrm{s} = \tau\bar{v}^2/2$ where τ denotes the time of flight an $\bar{v}$ an average velocity is utilized. The equation is equipped with the discussed relaxation time of 10 ps and a careful estimation of the average velocity by 10% of the Fermi velocity. The result of $D'_\mathrm{s} = 13.4\,\mathrm{cm}^2/\mathrm{s}$, taking into account $\sim v_\mathrm{F} = 163.5\,\mathrm{km/s}$ for $n_0 = 1.3 \times 10^{11}\,\mathrm{cm}^2$, is small compared to the classical diffusion. Hence, a minute contribution to the overall diffusion is likely, however, the observed drastic increase of D_s suggests a different effect to be dominant.

(iii) In the process of photoexcitation an equal number of electrons and holes are added to the intrinsic 2DEG of the QW, granting a plasma-like charge neutrality. Whereas holes are comparably heavy and thus stationary the photo electrons are separated by the applied voltage as they drift away. Knowing about the excitation spot size and the moderate drift velocity, it is reasonable to assume that the two types of carriers are isolated already after some hundreds of picoseconds. This time span corresponds to a typical time of measurement. As direct consequence of this continuous charge separation, three independent mechanisms can potentially influence the broadening of the spin package. Firstly, the loss of charge neutrality due to the absence of holes is followed by a Coulomb repulsion of the spin carrying photo electrons. This repulsion accelerates the spread of the ensemble and would be conceived as an enhanced diffusion. Secondly, another effect is expected for photo carrier densities comparable to the intrinsic doping. In this regime, the momentum relaxation time τ is strongly reduced by the fact that holes are potential partners for scattering. In the presence of electric field this holes would get separated and an increase in τ would enhance the diffusion coefficient. Thirdly, a similar effect is expected for the electron mobility. The effect of mutual Coulomb attraction and inelastic scattering in between holes and electrons on the mobility diminishes due to charge separation. Accordingly, electrons would accelerate to higher drift velocity the further they propagate away from the excitation spot. This effect would lead to a stretching of the spin package along the direction of applied field. However, in all three mechanisms the broadening would not be completely equivalent to diffusion as the Gaussian distribution of the electrons is not maintained. Regardless of this distortion, the obtained signal could probably still be described by the Gaussian shaped fit-function. This is because, the pump-probe measurement goes along with a convolution of two Gaussian shaped beam profiles, imposing a Gaussian-like shape to the measured signal. Generally, these effects are hard to quantify since mutual and opposed dependences exist in between τ and the Fermi energy as both exhibit a density dependence [125].

Generally, the massive increase in the diffusion coefficient points towards an additional mechanism like Coulomb repulsion since a tenfold increase in the Fermi energy or the relaxation time only due to heating appears to be drastic changes. An additional contribution of convectional diffusion cannot be ruled out but is expected to be small.

3.3.3 Back Gate Voltage

Besides the Hall bar structure, the GaAs sample provides a gate on the back side that can be used to modulate the electric potential along the growth direction of the heterostructure. At the same time, the gate controls the electron density n_e in the modulation doped QW through injection or draining of electrons that stem from the Si-δ layer outside of the QW. The general dependence of n_e on U_BG is discussed in the context of PL measurements in Section 3.1. So far the impact of the back gate voltage is briefly touched in Fig. 3.3 (c) where a peak-like tunability of the PSH lifetime is shown and attributed to a changing degree of the SU(2) symmetry. In the same figure a slight modification of the diffusion coefficient is reported that can be neglected in the following. Concerning the SO coupling parameters α and β, Fig. 3.5 already points towards a scalability with the applied back gate voltage. While such effects where mostly avoided until now due to fixing $U_\mathrm{BG} = -1.00\,\mathrm{V}$, this section will further quantify the Rashba and Dresselhaus parameter in a regime with variable back gate

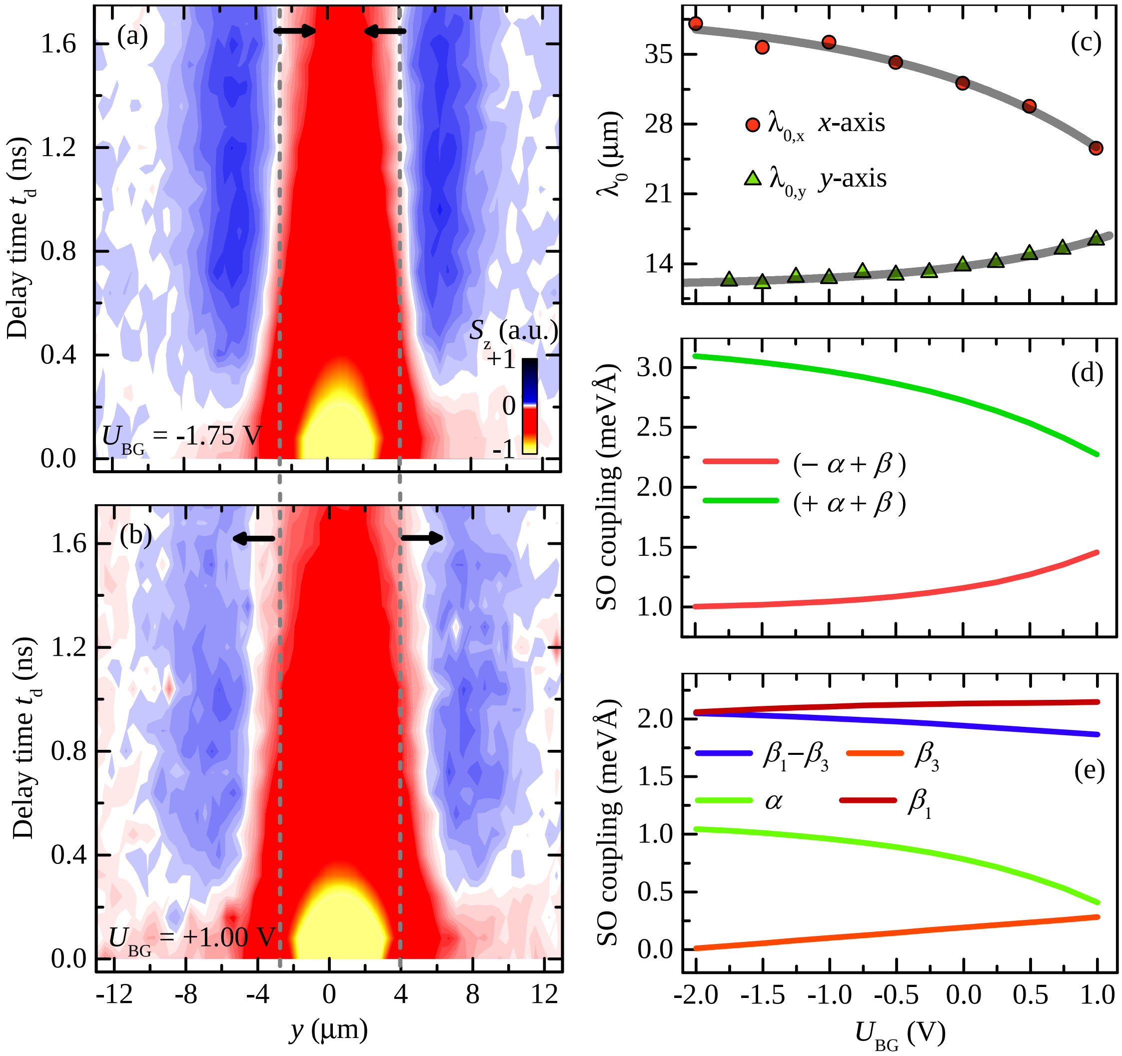

Fig. 3.12: Controlling the PSH with a back gate, allows for the simultaneous modification of the carrier density in the QW and the potential perpendicular to it. **(a-b)** False-color plot representations of spin polarization measurements that cover the spatiotemporal evolution of the PSH for two different gate voltages. **(c)** Effect of the back gate voltage on the spin-orbit coupling visible in the spin precession lengths $\lambda_{\mathrm{so,x}}$ and $\lambda_{\mathrm{so,y}}$ for the x- and y-axis respectively. **(d-e)** The individual Rashba and Dresselhaus parameters are extracted from (c) via their sum and difference in (d). Additionally, the β_3 contribution is added to (e) after calculation from the experimental carrier density which in turn is determined by PL measurements.

voltage. Here, it is expected that the Rashba parameter is directly affected by a change of the potential drop along the QW, entering into α. In between the two Dresselhaus contributions a differentiation must be made since β_1 is determined by the band structure and therefore expected to be unaffected by U_{BG}. On the other hand, β_3 exhibits a direct dependence on the carrier density and is thus sensitive to the density changes due to the gate.

Figure 3.12 (a) and (b) compare the spatiotemporal evolution of the PSH for both ends of the chosen voltage spectrum which is applicable to the sample without passing the damage threshold. The two false-color plots reveal the characteristic appearance of oscillations in the spin polarization during its diffusive expansion along the y-axis. It is noteworthy that a difference in the precession length of a PSH at $U_{\mathrm{BG}} = +1.0\,\mathrm{V}$ and $U_{\mathrm{BG}} = -1.75\,\mathrm{V}$ is visible by eye. In the figure, two parallel dashed lines in grey color are spanned along both maps and serve as a reference from which it can be seen that $\lambda_{\mathrm{so,y}}$ is shorter for negative U_{BG} as indicated by black arrows. This observation is confirmed by further measurements and an upward trend is extracted for $\lambda_{\mathrm{0,y}}$ along the y-axis. Each of the according data points, assembled in panel (c) as green triangles, is generated individually from a spatiotemporal measurement and the consecutive extraction of $\lambda_{\mathrm{so,y}}$ and $\lambda_{\mathrm{0,y}}$ (cf. Fig. 3.2). In the same panel (c) a decrease of $\lambda_{\mathrm{0,x}}$ is shown as red dots. This decreasing trend represents the spin precession length extracted along the x-axis. The procedure used to determine $\lambda_{\mathrm{0,x}}$ is established in the previous section where in-plane electric fields are harnessed to uncover the long ranged spin precession along the x-axis. For this axis smaller effective magnetic fields act on the electron spin.

Moreover, both trends in Fig. 3.12 (c) are modeled with an exponential function in order to facilitate further calculations based on the parameter dependence on U_{BG}. The opposite behavior of $\lambda_{\mathrm{0,y}}$ and $\lambda_{\mathrm{0,x}}$ is best understood from the fact that the former precession length is determined by the sum $(\alpha+\beta)$ whereas the latter one is dictated by the difference $(-\alpha+\beta)$ of the SO coupling parameters. Consequently, the sum and difference values can be calculated and are shown in panel (d) where a growing difference value and a diminishing summed value can be identified. This behavior agrees well with the previously made assumption that a variation of α is the dominating effect when the back gate voltage is changed. Knowing the sum and difference of α and β the individual values can be determined and are plotted in panel (e). From there it is evident that α undergoes a decline while the gate voltage is tuned upwards and β remains comparably constant even though a slight decrease in the blue line is visible. A 60 % change of α is stated by the data and is within the margins seen by other groups [102; 139]. Aiming at an even more detailed description, values for β_3 are added to the plot in panel (e) as orange line. These values are calculated by transforming the experimentally seen carrier density (smoothed by a linear fit as shown in Fig. 3.1) into the Fermi wave vector. This wave vector is given by the expression $k_{\mathrm{F}} = \sqrt{2\pi n_{\mathrm{e}}}$ and inserted into Eq. (1.29), yielding β_3. Subsequently, the blue line of data for $\beta = \beta_1 - \beta_3$ can be used to quantify the remaining β_1 contribution and the result is added to the plot. As a result, the trend for β_1 is almost constant, leaving the slight decrease of β to a strong contribution of β_3 caused by an enhanced carrier density in the case of higher back gate voltages. The strong variation of the cubic Dresselhaus contribution is remarkable as it offers a peculiar fine tuning knob for the PSH. Furthermore, this results are confirmed by similar findings of gate control based on β_3 [52].

3.3.4 Optical Doping

After having focused on the in-plane electric fields in the GaAs structure, the investigations of the CdTe sample are resumed within this section. As the available sample does not provide electrodes for the application of bias the spin helix in CdTe cannot be directly affected from the outside other than with in-plane magnetic fields. A full analysis for the magnetic field dependence in GaAs is given in Section 3.3.1 where the results for measurements in CdTe are stated in Table 3.2, however, an in-depth discussion was left out and will be made up for here. The succeeding discussion reveals a so far untouched tuning knob for the PSH, namely the locally induced carrier concentration. Here, it is discussed how local gradients in the concentration due to optical excitation affect the Rashba and Dresselhaus SO coupling. In addition, a similar impact on the diffusion coefficient of the spin distribution is found.

It is thoroughly discussed in Section 3.3.1 how the application of external magnetic fields in perpendicular direction to the measurements along x- or y-axis respectively is able to actively manipulate the PSH helix evolution. This effect becomes foremost visible in a tilting of the spin polarization stripes seen in spatiotemporal measurements. The detected tilting is attributed to a canceling of effective and external magnetic fields such that electrons with a specific momentum are locked in their spin polarization during travel (cf. scheme in Fig. 3.6). Moreover, the quantification of the corresponding momentum yields the individual α and β parameters if extracted for both axes from the respective expressions

$$v_{\mathrm{y1}} = \frac{\mathrm{d}y_1}{\mathrm{d}t} = \frac{g\hbar\mu_{\mathrm{B}}}{2m^*(\alpha+\beta)} \cdot B_{\mathrm{ex,x}} \qquad \text{and} \qquad v_{\mathrm{x1}} = \frac{\mathrm{d}x_1}{\mathrm{d}t} = \frac{g\hbar\mu_{\mathrm{B}}}{2m^*(-\alpha+\beta)} \cdot B_{\mathrm{ex,y}} \tag{3.22}$$

which predict a constant slope for the tilted stripes. The spatiotemporal maps of spin polarization depicted in Fig. 3.13 (a) and (d) represent measurements along both axes with a magnetic field of 231 mT applied in the perpendicular direction respectively. In comparison to the equivalent measurements in GaAs (cf. Figures 3.5 and 3.6) a significantly higher number of oscillations is observable even though the PSH lifetime appears comparable. At the same time, the tilt of the individual stripes is much more pronounced in CdTe. These observations are explained by a g-factor of 1.6 that can be determined by the spin beat frequency at position (x, y) =(0 μm,0 μm). The g-factor enters into Eq. (3.22), demanding a higher electron velocity to cancel the external magnetic field. Combining the sum and difference of Rashba and Dresselhaus parameter, gathered from panel (a) and (d), the individual values $\alpha = (2.35 \pm 0.30)\,\mathrm{meV\AA}$ and $\beta = (1.73 \pm 0.30)\,\mathrm{meV\AA}$ are determined.

The (c) panel of the same Figure shows a simulation based on kinetic theory. Generally, this simulation is in good agreement with the experiment shown on the opposite side of the figure since the increased tilt and the number of oscillating stripes are reproduced. However, by closer inspection the attention is drawn to a phenomenological feature of the experiment, missing in the simulation. This feature is the saddle-point-like appearance of the stripes in the experiment highlighted in the plot by a dotted line. While this behavior is striking along the y-axis it is much weaker yet present as well in the data along the x-axis. Even though, the s-shape is fairly pronounced in the experiment it is completely absent in the kinetic theory (KT) simulation as indicated by a straight, dashed line in the simulation panel (c). Generally, the feature is not forecasted by the theoretical model which predicts a constant tilt based on spatially constant SO coupling. The observed saddle-point-like shape, on the other hand, points rather to a deceleration of $\mathrm{d}y_1/\mathrm{d}t$ while the electrons spread away from the origin at

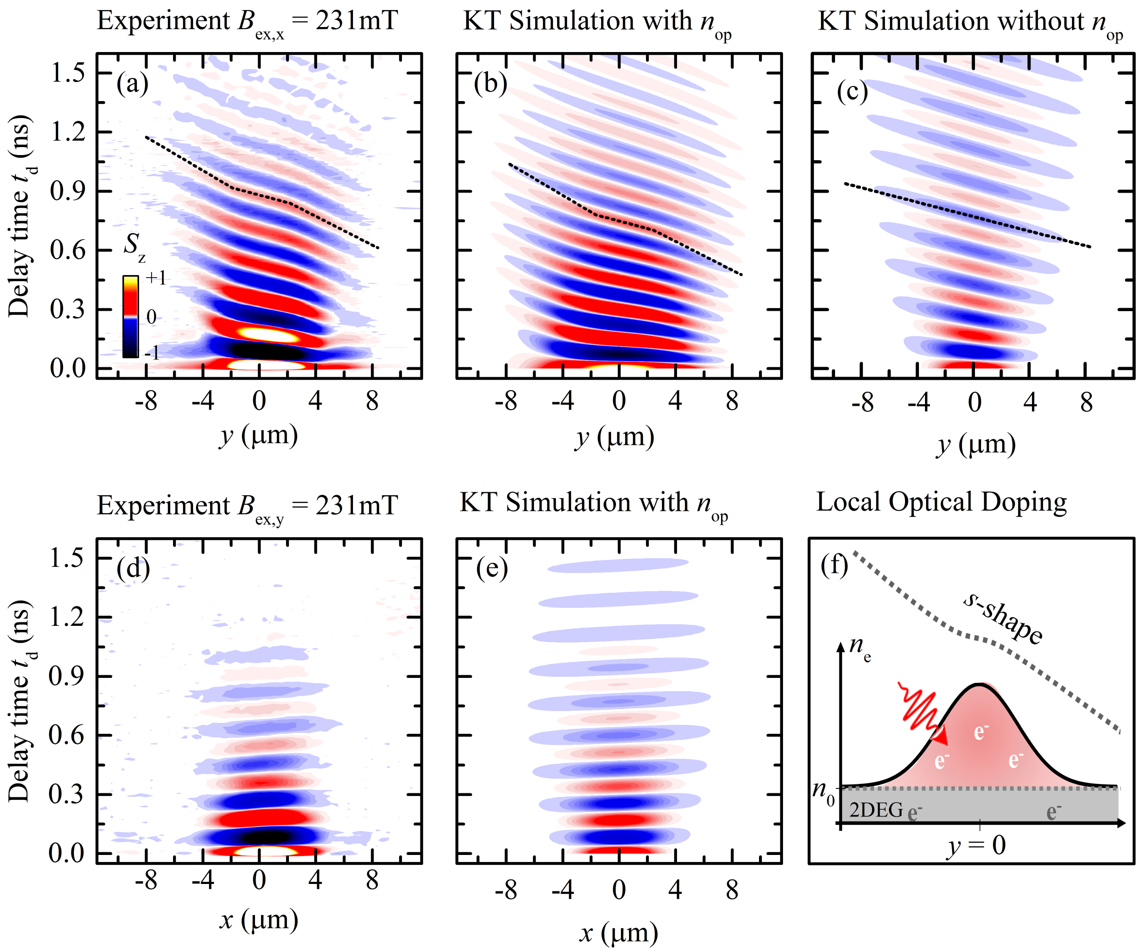

Fig. 3.13: Experimental and simulated spatiotemporal maps in false-color representation, displaying the tilt of the CdTe PSH in external magnetic fields. **(a-c)** Measurement along the y-axis (a), one KT simulation takes a local modulation of α and β into account (b) whereas the other does not (c). A saddle-point-like shape of the tilt is indicated by identical dashed lines in (a) and (b). **(d-e)** Measurement and KT simulation along the x-axis with n_{op} analogous to (a) and (b). **(f)** Schematic injection of a Gaussian photocarrier distribution in addition to the resident 2DEG in the QW, forming the origin of the saddle-point-like stripes seen in the measurements as black, dashed lines.

$y = 0\,\mu$m. Taking into account the formulae in Eq. (3.22) such a spatial modulation of the stripe slope can only arise from the α and β parameters being different in the center of the plot than at the edges provided all other entities in the theory are fixed constants. Attempting to explain a locally disturbed SO coupling, it is reasonable to consider an influence of the excitation process of the PSH during which photo excited carriers are injected from the valence band into the conduction band. It can, therefore, be assumed that the excitation creates a non-equilibrium regime which affects the PSH if sufficiently many photo electrons are involved.

Figure 3.13 (f) illustrates a schematic picture of photo electrons which form a Gaussian distributed density n_{op} in addition to the resident 2DEG electrons n_0. In the case that n_{op} and n_0 are of similar size it is expected that the SO coupling parameters are spatially modulated, following the spatial distribution of photo carriers. Such modulation takes place for to reasons.

First, screening of the electric field in the case of α and second, a direct renormalization of the Fermi wave vector $k_\mathrm{F} = \sqrt{2\pi(n_0 + n_\mathrm{op})}$ that determines β_3. Due to the multivariate influence of the carrier density on the system a direct quantification of the above introduced hypothesis turns out to be challenging. Therefore, measurements in dependence on the peak optical intensity of the laser are performed. For this experiments the direct impact of the laser intensity on the photo carrier density has to result in equally strong effects on the SO coupling. This conclusion is sustained by numerical estimations for the injected carrier density n_op to be in the range of $(0.5 - 2.6)\, n_0$ where $n_0 = 3.4 \times 10^{11}\,\mathrm{cm}^{-2}$. Such an estimation is justified by the range of utilized peak optical intensities $(2.36 - 11.8)\,\mathrm{MW/cm}^2$ in combination with an absorbance of 2.6 % [140]*. Additionally, a 30 % Fresnel coupling loss due to the difference in the refractive index of air and the GaAs heterostructure is taken into account [141].

Figure 3.14 (a) depicts five line scans taken under the same conditions, varying only the optical peak intensity of the laser. The intensity is determined from the average power P_avg in front of the sample and the formula

$$I_\mathrm{op} = \frac{1}{\nu_\mathrm{R} t_\mathrm{pulse}\left[\pi (w_0/2)^2\right]} \cdot P_\mathrm{avg} \tag{3.23}$$

which takes into account the repetition rate of the laser ν_R. Further, the pulse duration $t_\mathrm{pulse} \sim 1\,\mathrm{ps}$ is calculated from the spectral width and the laser spot size on the sample is calculated by the initial FWHM of the Gaussian excitation spot w_0. For the purpose of better comparability among the individual measurements and with succeeding simulations, only the data for positive y-values are selected from the symmetric scans around zero. Studying individual line scans for a fixed $t_\mathrm{d} = 750\,\mathrm{ps}$ enables the inspection of subtle features that are much harder to recognize in full spatiotemporal maps. The normalized experimental curves undergo a strong change of shape while the intensity is raised. An increased modulation depth together with a longer ranging spin precession length are visible in the experimental data where both trends are highlighted with arrows. From the experiment it is apparent that the higher the intensity, the further away from the origin, the signal can be detected. This finding suggests an increased diffusion which is confirmed by individual analysis of the full spatiotemporal map for each intensity (data not shown). In accordance with the inset in Fig. 3.14, a linear rise of D_s with tuning up the intensity is confirmed. The same inset illustrates the estimated photo carrier density in dependence on I_op, explaining the increased diffusion coefficient as follows. The Fermi energy depends directly on the electron density in the system and a locally elevated density will result in an increased Fermi energy and velocity which follow the same distribution. Moreover, the Fermi velocity is a determining part of the diffusion coefficient given by $D_\mathrm{s} = \tau_\mathrm{ee} v_\mathrm{Fermi}^2/(2m^*)$. However, the direct calculation of a general D_s is complicated due to a spatial and temporal density modulation, the latter is caused by the recombination

---

[*] The spectral dependence of the absorbance in CdTe is given for room-temperature in the cited reference. To estimate the absorbance at 3.5 K, where the experiment is conducted, it is necessary to transfer the pump energy of 1.475 eV to RT by employing the Varshni formula and parameters given in Section 3.1. The resulting energy allows to pick the correct absorbance from the reference.

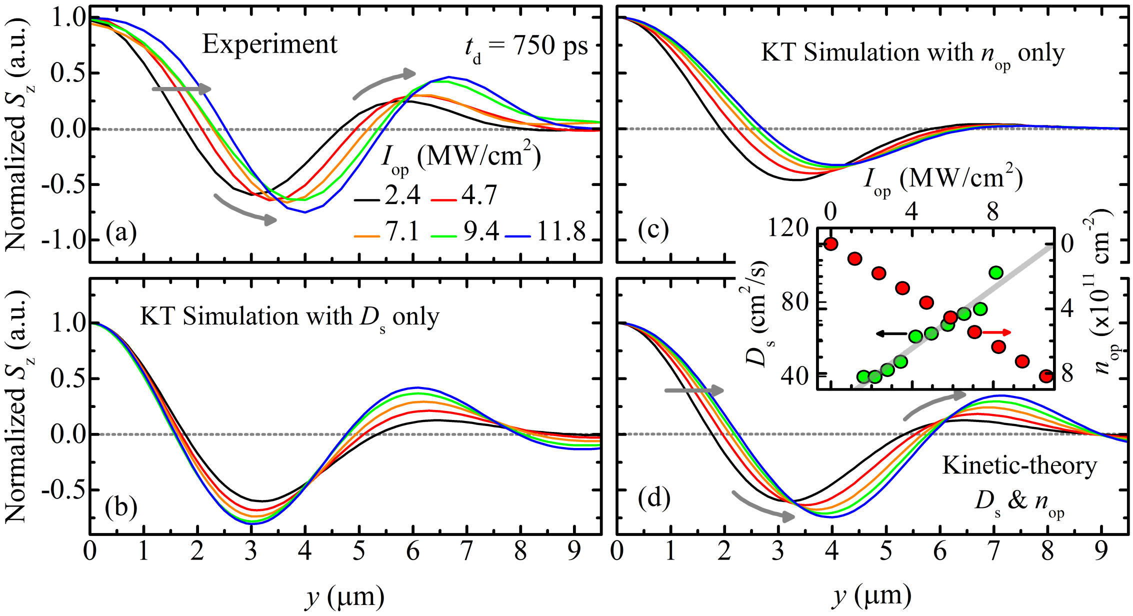

Fig. 3.14: **(a)** Experimental line scans for varying optical intensities taken at $t_\mathrm{d} = 750\,\mathrm{ps}$. **(b-c)** KT simulations of the experiment with changes of only n_op (c) or only D_s (b) in accordance with the inset that relates both entities with the peak laser intensity. **(d)** KT simulation based on spatially modulated SO coupling parameters and diffusion coefficient, reproducing the qualitative trends of the experiment illustrated by grey arrows.

of 2DEG electrons with holes. While spatial modulation cannot be reasonably considered, the lifetime of electrons for similar structures is known to be comparable or shorter than the spin lifetime[142; 143]. For the present sample a lifetime of $T_\mathrm{c} \sim 1\,\mathrm{ns}$ is obtained from transient reflection measurements at the probed Kerr rotation resonance. It was shown already in the previous section that a changed diffusion coefficient has a severe influence on the measured spin precession length λ_so due to a faster or slower transition from a multi-mode Gaussian to the single-mode PSH. For this reason it is vital to review the possibility that the variation of the diffusion itself causes the differently shaped line scans observed in the experiment.

The (b) panel in Fig. 3.14 displays KT simulations for the same parameter set as encountered in the experiment. As a result, a pronounced increase in the modulation depth can be achieved. However, the simultaneous variation of the spin precession length is not reproduced, resulting in a visible deviation of the simulation from the experiment. This leads to the conclusion that, indeed, the photo carrier density plays an important role in the SO coupling process and an according model is required to verify this assumption. For the purpose of a further validation a dynamic carrier density in space and time is modeled by the expression

$$n_\mathrm{e}(x, y, t_\mathrm{d}) = n_0 + n_\mathrm{op} \ln(2)\pi \left[\frac{w_0^2}{w^2(t)}\right]^2 e^{-4\ln(2)\left[x^2+y^2\right]/w^2(t)} \cdot e^{-t_\mathrm{d}/T_\mathrm{c}} \tag{3.24}$$

that combines intrinsic and optical doping. The combination follows an approach that considers the diffusive broadening of the electron distribution as well as the temporal decay due to electron-hole recombination and is schematically shown in panel (f) of Fig. 3.13. The found expression in Eq. (3.24) enters directly into the calculation of the cubic Dresselhaus parameter as

$$\beta_3(x, y, t_\mathrm{d}) = \gamma_\mathrm{D}\pi \cdot n_\mathrm{e}(x, y, t_\mathrm{d})/2, \tag{3.25}$$

imposing novel spatiotemporal dynamics to β_3 in the form of a local and transient increase. On the other side, it is reasonable to account for a similar dependence in α. The Rashba parameter is indirectly affected as additional charge screens the internal electric field in the QW, entering into $\alpha = \gamma_\mathrm{R}\mathcal{E}_\mathrm{QW}$. An according model is based on the depolarization field $\delta\mathcal{E}_\mathrm{z}$ created by a minute number of carriers given by the density δn_e. The depolarization field is then given by

$$\delta\mathcal{E}_\mathrm{z} = \rho \cdot \frac{e^2 m^2 d_\mathrm{QW}^3}{\epsilon\hbar}\mathcal{E}_\mathrm{z}\delta n_\mathrm{e} \tag{3.26}$$

where ϵ denotes the dielectric constant and ρ is a dimensionless parameter that models the fabrication of the QW and is not strongly affected by the carrier density itself. From this consideration the impact of optical doping can be passed to the Rashba parameter by perturbation with the depolarization field, yielding

$$\alpha(x, y, t_\mathrm{d}) = \alpha_0 \cdot e^{-\rho m^* e^2 d_\mathrm{QW}^3/(\epsilon\hbar)[n_\mathrm{e}(x,y,t_\mathrm{d}) - n_0]} \tag{3.27}$$

where α_0 represents the as-grown Rashba parameter, formerly addressed as α. By now, the differential equation employed for kinetic theory simulations can be equipped with the new expressions for α and β_3 and solved numerically. This yields the simulated curves in Fig. 3.14 (c) where the optical density is chosen from the relation shown in the inset, matching the intensities used in the experiment. The obtained simulations reveal a strong tuning of the zero crossings for the signal whereas the distinct tuning of the modulation depth seen in the experiment is not reproduced. As a consequence, the local variation of the SO coupling alone cannot be the origin of the s-shape.

Reviving the observations made for the diffusion coefficient, the simulation is redone with a combined approach where an increase of the diffusion coefficient and of the optical density is considered at the same time. This combination leads to the set of simulated curves in the (d) panel. Eventually, these simulations show a remarkable compliance with the experiment as both the modulation strength and the shift in the precession length are qualitatively reassembled. These successful simulations stand as a strong evidence for the assumed influence of optical doping on the PSH. This finding is strengthened by the proof that neither changes of D_s nor of n_op alone can explain the experiment. Moreover, the same kinetic theory model is used to investigate the origin of the unexplained s-shape that motivated the idea of photo carrier induced fine tuning. The penultimate Fig. 3.13 contains two false-color plots in panel (b) and (e) which depict KT simulations with density-dependent SO coupling parameters and the s-shape of stripes is now clearly recognizable. This visual comparison serves as an additional validation of the photo carrier density as fine tuning mechanism for the PSH and finally explains the saddle-point-like behavior.

The found gradients of the SO coupling parameters can be made responsible for several deviations of the CdTe data from the theoretical model in Section 3.2. This deviations include a high error of the diffusion coefficient in Table 3.1 and a curved appearance of the PSH in the 2Dmap of Fig. 3.4 (a). As no gradient of the SO coupling is included in the standard fit functions it is expected that the resulting fit parameters can only give a limited explanation of the experimental data.

3.4 The Traveling PSH

In the previous sections, various possibilities for tuning the SO coupling parameters are presented. Particularly the application of electric and magnetic fields, as a tool for precise engineering of the electron spin dynamics, is demonstrated. Moreover, the experimental results can be widely matched with the theoretical models established for the spatiotemporal evolution of a spin ensemble into a drifting persistent spin helix. Accordingly, a profound understanding of the underlying mechanisms of spin-orbit coupling and the spatial dynamics is established. At this point, the achieved understanding of magnetic, in-plane electric fields and gate fields shall now be merged into a novel approach towards a comprehensive control of the PSH, firstly demonstrated in the present GaAs QW sample. For this purpose, a tailored superposition of magnetic and electric fields is harnessed to transport the PSH while the spin orientation of the drifting spins is locked. The resulting phenomenon is called the traveling persistent spin helix (TPSH). The TPSH maintains a high symmetry of SO coupling fields in k-space, sustaining the robustness of the spin coherence during the transport. Coherent transport of long living spins is a fundamental advantage for the use of the PSH as new information carrier in spintronics where an encoding of information in α and β is conceivable. Promising proposal for PSH based spin transistors were already published [144]. However, fine coordination of all available tuning knobs is needed to unleashes the PSH from being a fundamental research object only. This coordination transforms the peculiar conjunction of spin encoded information and spatiotemporal dynamics into an application-ready phenomenon that can be integrated in future spintronic based technology.

Figure 3.15 depicts a four-fold schematic flowchart in order to illustrate the experimental realization of the TPSH, starting from the unperturbed PSH in (a) and subsequent combination of PSH patterns that are exposed to electric (b) or magnetic (c) fields respectively. For each step of the flowchart a measurement in form of a spatiotemporal false-color plot is matched with a scheme. The scheme visualizes the k-space distribution of effective and external magnetic fields in relation to the k-states which are occupied by the contributing electrons. The (a) panel depicts the characteristic appearance of the PSH as discussed thoroughly in Section 3.2. For this standard PSH a point symmetric distribution of the effective magnetic field is indicated by purple colored arrows along the k_y-axis. The absence of in-plane

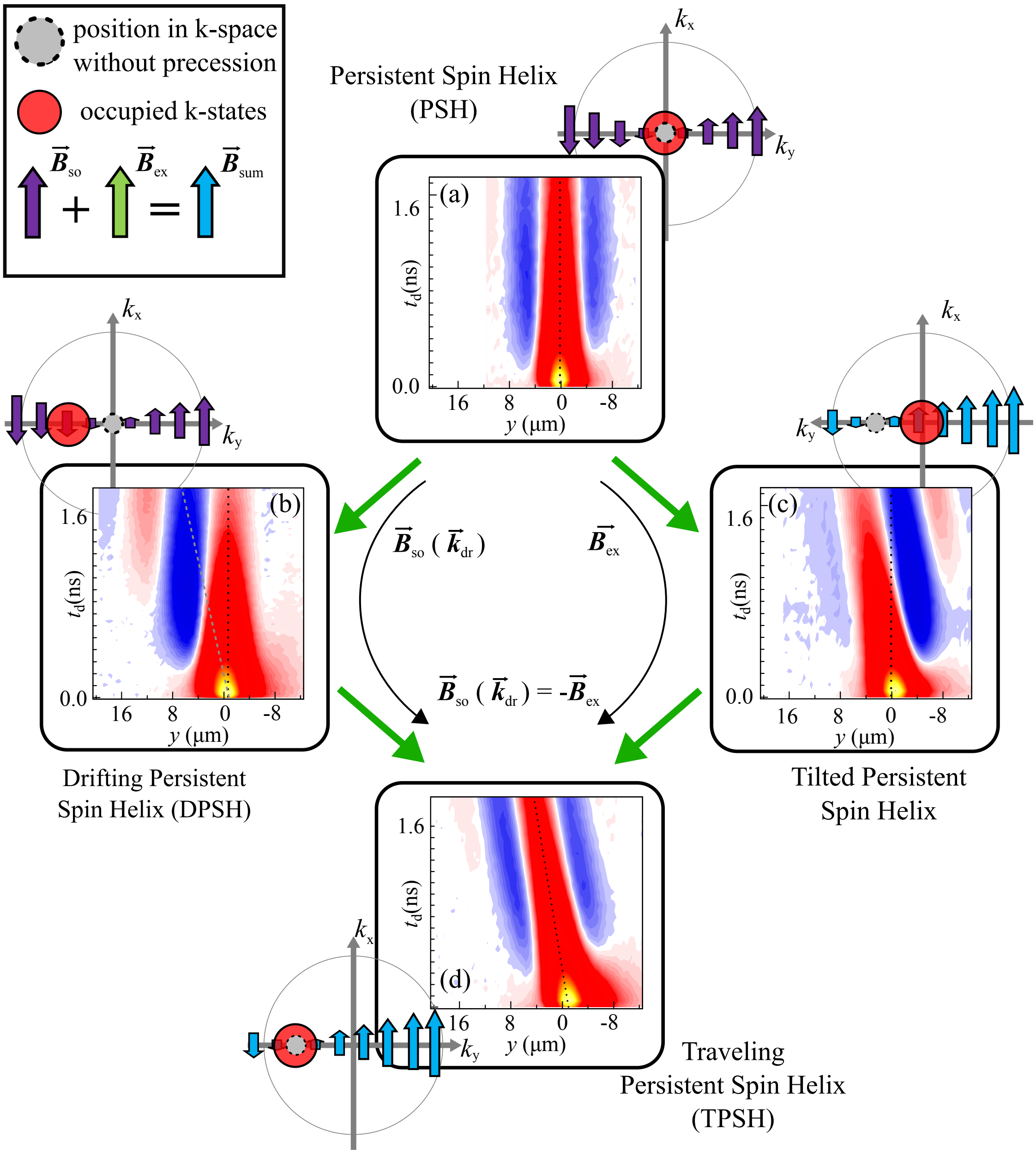

Fig. 3.15: Schematic flow-diagram, visualizing the emergence of the TPSH from the standard PSH as a result of superposing magnetic and electric fields. The false-color representations of spatiotemporal maps are combined with schematic illustrations of the effective magnetic field distribution in k-space. The effective and external magnetic fields are represented by colored arrows and the position of occupied states and states without spin precession are marked (cf. legend). The length of the arrows represents the field strength.

electric fields results in a k-space occupation that is centered around zero and broadened by diffusion as illustrated by a red circle. The electron spins which do not precess are those who exhibit zero momentum on average. In the scheme these k-states are marked by a grey dot with dashed margin. Within the associated false-color plot this configuration results in constant spin polarization around $y = 0\,\mu$m as highlighted by a dotted line drawn in parallel to the time axis. The spin precession, visible as emerging blue stripes, is purely related to diffusion momentum and the related effective magnetic field. The tunability of this standard PSH is somewhat limited as the spin orientation is entirely dictated by the spatial position of the spin carrying electron. Tuning within a certain range can be realized by adjusting of the spin precession length via the back gate voltage (cf. Section 3.3.3). However, the adjustments in space are rather minute and inevitably accompanied by a detuning of the Rashba to Dresselhaus parameter ratio, resulting in an undesirable modulation of the lifetime.

The application of in-plane electric field as presented in the (b) panel allows for a much stronger tuning of the spin dynamics. Here, the effective magnetic field distribution in k-space is not different from the standard PSH regime whereas the contributing electrons occupy wave vector states that are centered around the drift momentum. The real space position for electrons that do not feel any magnetic field remains at $y = 0\,\mu$m. This statement has to be partly adjusted after the discussion in Section 3.3.2 (cf. Fig. 3.8 and Fig. 3.9). In this section an imbalance in the cubic Dresselhaus contribution of drift and diffusion induced SO coupling is investigated, leading to a temporal precession independent from the spatial position. This specific effect was identified as a fine tuning mechanism and can therefore be neglected for the following considerations. In contrast to the standard PSH, the spatial dynamics of the DPSH can indeed be influenced by the choice of $E_{\mathrm{IP}}^{\mathrm{x}}$ and $E_{\mathrm{IP}}^{\mathrm{y}}$ in-plane electric field. In theory, the spins can be transferred to any point of the QW at any time. However, the applicable field strength is limited by the damage threshold of the sample. Regardless of how far the electrons can be moved, the orientation of the spin polarization is still following the spatial pattern of the standard PSH that is dictated by the unchanged effective field distribution. As a consequence, the underlying helix pattern is the same for PSH and DPSH in terms of strip orientation and position.

The situation of the DPSH is reversed for the tilted PSH observed in applied external magnetic fields and depicted in the (c) panel of the flowchart. In this regime the electron momenta are still centered around zero. The k-space position of spins without precession, on the other hand, is moved to non-zero values of momentum where the effective magnetic field is strong enough to cancel the external field. The application of external magnetic field enables the adjustment of the spin orientation as the Larmor frequency can be controlled via the magnetic field strength, acting in addition to the effective fields. In conclusion, the use of external magnetic field warrants a degree of freedom concerning the spin orientation. However, a freedom of transferring the spin polarization to a certain spatial position is not given, representing a major drawback for full control of the spins.

In summary, it can be said that the individual application of magnetic or electric fields is not sufficient for complete spin control. This leads to the conclusion that a superposition of electric and magnetic fields is needed to overcome the discussed limitations. The TPSH represents such a combination and is depicted in panel (d) of the flowchart. A careful selection of the electron drift wave vector $\boldsymbol{k}_{\mathrm{dr}}$ generates an effective field of the same magnitude as the external magnetic field. This equilibrium reads

$$B_{\mathrm{ex,x}} = -B_{\mathrm{so,x}}(k_{\mathrm{dr,y}}) = \frac{2m^*\mu_{\mathrm{e}}}{g\mu_{\mathrm{B}}\hbar}(\alpha+\beta)E_{\mathrm{IP}}^{\mathrm{y}} \qquad \text{with} \qquad k_{\mathrm{dr,y}} = -\frac{m^*}{\hbar}\mu_{\mathrm{e}}E_{\mathrm{IP}}^{\mathrm{y}} \tag{3.28}$$

where the electric field determines the drift velocity $v_{\mathrm{dr,y}} = -\mu_{\mathrm{e}}E_{\mathrm{IP}}^{\mathrm{y}}$ and thus the effective magnetic field. This specific TPSH condition is displayed in the (d) panel and can be understood as the standard configuration (cf. panel (a)) translated to negative values of momentum. The TPSH is equivalent to a standard PSH that evolves symmetrically around the center with the only difference that the center itself travels along with the drift current. Thus the spatiotemporal evolution in the false-color plot appears as a tilted PSH. In this configuration, the spin orientation at any position is freely eligible by redirecting the optically excited spins to this point while the SO coupling is virtually switched of. Remarkably, the SU(2) symmetry of the effective fields is not affected by this manipulation, sustaining the long coherence of spins while they are repositioned in space.

Before the established toolbox is used for the quantitative analysis of the TPSH, another qualitative discussion about the spatial appearance is conducted by means of the 2Dmaps displayed in Fig. 3.16. The figure depicts three columns of 2Dmaps, each containing five false-color plots for delay times from 0 ps to 1785 ps. Whereas the first two columns illustrate the spatial evolution of the already discussed PSH and DPSH the third column shows the TPSH. In accordance with the spatiotemporal map in panel (a) of Fig. 3.15, the standard PSH develops a striped oscillation pattern symmetric on both sides around the center position which is indicated by a dashed line that spans over all 2Dmaps of the column. In the middle column a DPSH is monitored for which an in-plan electric field of $E_{\mathrm{IP}}^{\mathrm{y}} = 1.00\,\mathrm{V/cm}$ propagates the spin ensemble to negative y-values. The corresponding shift of the center position is again marked by a dashed line, exhibiting a gradient due to the drift. Moreover, the spin pattern loses its symmetric shape since the drifting spin polarization does not spread isotropically. However, the position of stripes remains unchanged from the standard PSH picture with the only difference that the spins reach further in space and reveal more stripes.

The TPSH, shown in the right column, features a continuous shift of the stripes while the entire spin polarization propagates to the left. Here, v_{dr} and v_{y1} are matched, leading to a regime where the center position of the spin ensemble drifts and maintains its spin orientation.

It is noteworthy, that the diffusive spread of the spin polarization in space becomes anisotropic for long delay times. This is the case only for applied electric fields where the pattern is elongated along the y-axis whereas the standard PSH is stretched equally along both axes. This observation supports the idea of an accelerated spreading due to the separation of photoexcited electrons and holes. In accordance with the discussion given at the end of Section 3.3.2, charge separation leads to a gradient in the mobility along the direction of drift. This gradient would most likely go along with an anisotropic distribution of the ensemble.

Subsequent to the qualitative introduction a quantitative analysis is conducted on the spatiotemporal evolution of the traveling PSH shown in Fig. 3.17. Here, the time dependence of important fit parameters, extracted from the application of Eq. (3.3) to the spatiotemporal

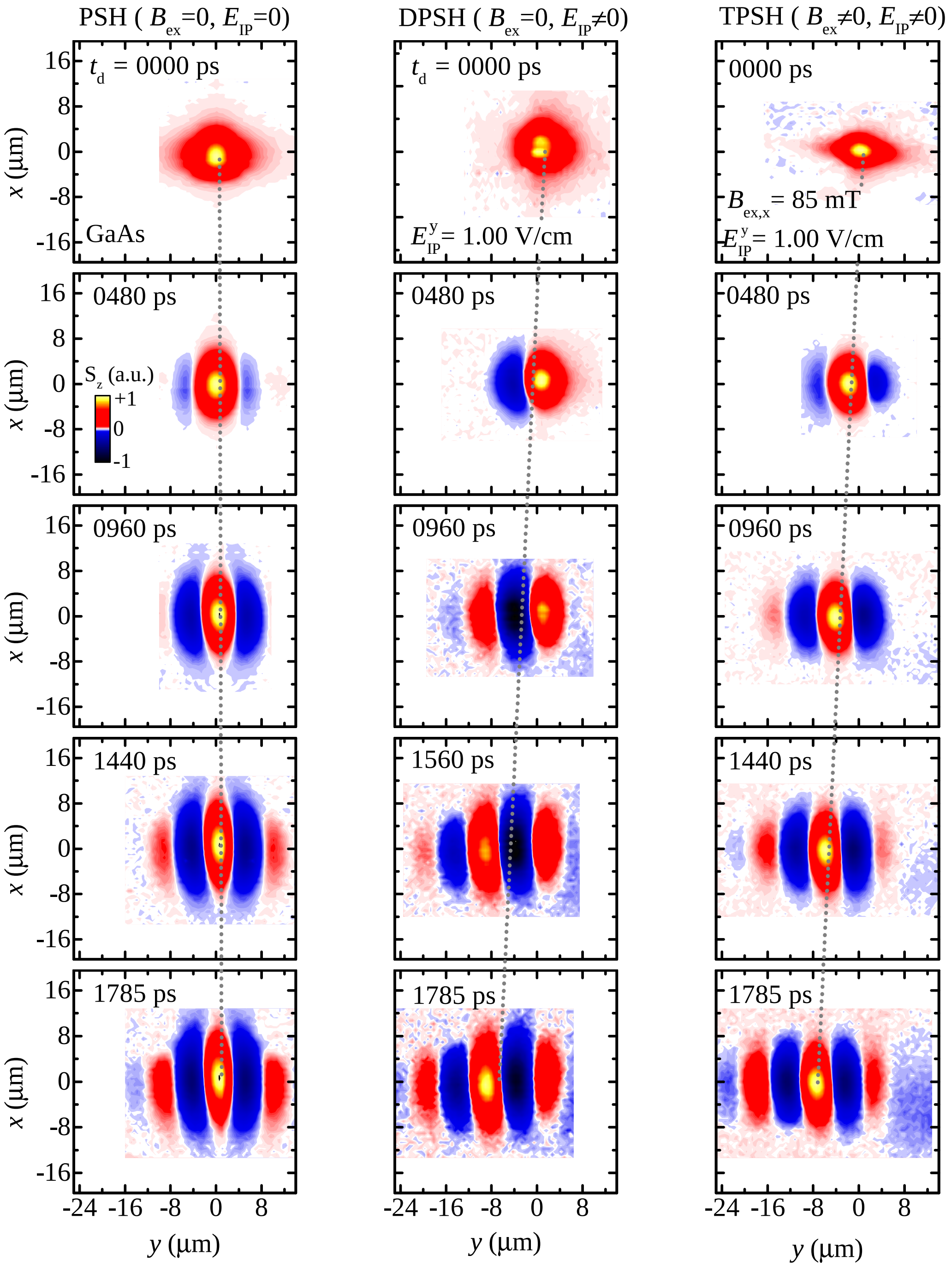

Fig. 3.16: Series of 2Dmaps for a variety of delay times, spanning the lifetime of the spin helix pattern. The evolution of the standard PSH (left column) and DPSH (center column) is compared with the appearance of the traveling PSH (right column). Dashed lines are added to each column in order to trace the center of spin polarization. Remarkably, the spin orientation is conserved along the dashed transient for all TPSH micrographs.

data, is investigated. The (c) panel depicts the same false-color plot as in the flowchart 3.15 where an in-plane electric field of $E^{\mathrm{y}}_{\mathrm{IP}} = 1.3\,\mathrm{V/cm}$ is combined with a magnetic field of

$B_{\mathrm{ex,x}} = 115\,\mathrm{mT}$ in perpendicular direction. This field combination locks the spin orientation and effectively switches off the SO-coupling for electrons that propagate with a drift velocity of $v_{\mathrm{dr,y}} = 7810\,\mathrm{m/s}$. This drift velocity is obtained from a best linear fit of the time-dependent parameter y_{c} which is illustrated in panel (g). In the same panel the cosine offset parameter y_1 is plotted and exhibits as well a linear decrease with proceeding delay time. It has to be stressed that the center of the Gaussian and the cosine center in panel (g) shift with almost equal velocity which is crucial for the formation of the TPSH. This is the case, because the agreement of both parameters over the entire delay time ensures that the spin-helix pattern develops symmetrically with constant spin orientation at the center position. The small difference in the velocities points at a non-perfect adjustment of the fields. This adjustment can be further improved by an increase (decrease) of the magnetic (electric) field strength. In the spatiotemporal map of panel (c) the imperfection manifests as a second red stripe of spin polarization that appears on the left side of the center from 1.0 ns on. Such a feature is not visible on the right hand of the center which indicates that the center of Gaussian moves slightly faster than the center of the cosine.

Carrying on with the parameterization, panel (f) gives insight into the diffusive behavior of the TPSH since it maps out the squared FWHM of the Gaussian spin distribution versus the delay time. The observed linear trend matches earlier findings for D_{s}. From a best linear fit, using Eq. (1.26), $D_{\mathrm{s}} = 145\,\mathrm{cm}^2/\mathrm{s}$ is obtained which is slightly higher yet still comparable with results from the DPSH for the same field. (cf. Fig. 3.9 (c)). In the preceding sections it was already discussed that an applied in-plane field leads to an accelerated diffusion compared to the standard PSH. In the TPSH case, however, the enhanced diffusion is harnessed for a faster developing spin pattern while the symmetry of the oscillation is maintained. In summary, it can be claimed that the additional magnetic field has no influence on the diffusion.

Moreover, the fit function allows for the determination of $\lambda_{\mathrm{so,y}}$ and the corresponding time dependence is depicted in (e) panel where a characteristic convergence of the spin precession length to the final PSH mode is revealed. This reciprocal time dependence is discussed for the PSH (cf. Fig. 3.3) as spatial confinement effect. It is not surprising to see a similar trend in the TPSH that evolves as well from a Gaussian shaped excitation. A best fit with Eq. (3.4) provides a value of $11.2\,\mu\mathrm{m}$ for the PSH mode $\lambda_{0,\mathrm{y}}$. This value is elevated compared with the corresponding DPSH result in Fig. 3.9 (d) where a slightly smaller $\lambda_{0,\mathrm{y}}$ is measured for the present field of $1.3\,\mathrm{V/cm}$. This finding is of great interest as it suggests a different influence of the in-plane electric field in the case of TPSH than in the DPSH regime and thus has to be investigated in more detail.

The schematic field distribution in Fig. 3.15, used to motivate the TPSH, is focused on spin transport along the y-axis. Independently of this, the underlying concept of spin locking is equally applicable for transport along the x-axis. In this experimental configuration the external field $B_{\mathrm{ex,y}}$ is adjusted to be equal in strength with the effective magnetic field that originates from the drift wave vector $\boldsymbol{k}_{\mathrm{dr}} = (m^* v_{\mathrm{dr,x}}/\hbar, 0)$. Accordingly, the effective magnetic field for electrons that propagate along the x-axis is determined by the difference $(-\alpha + \beta)$

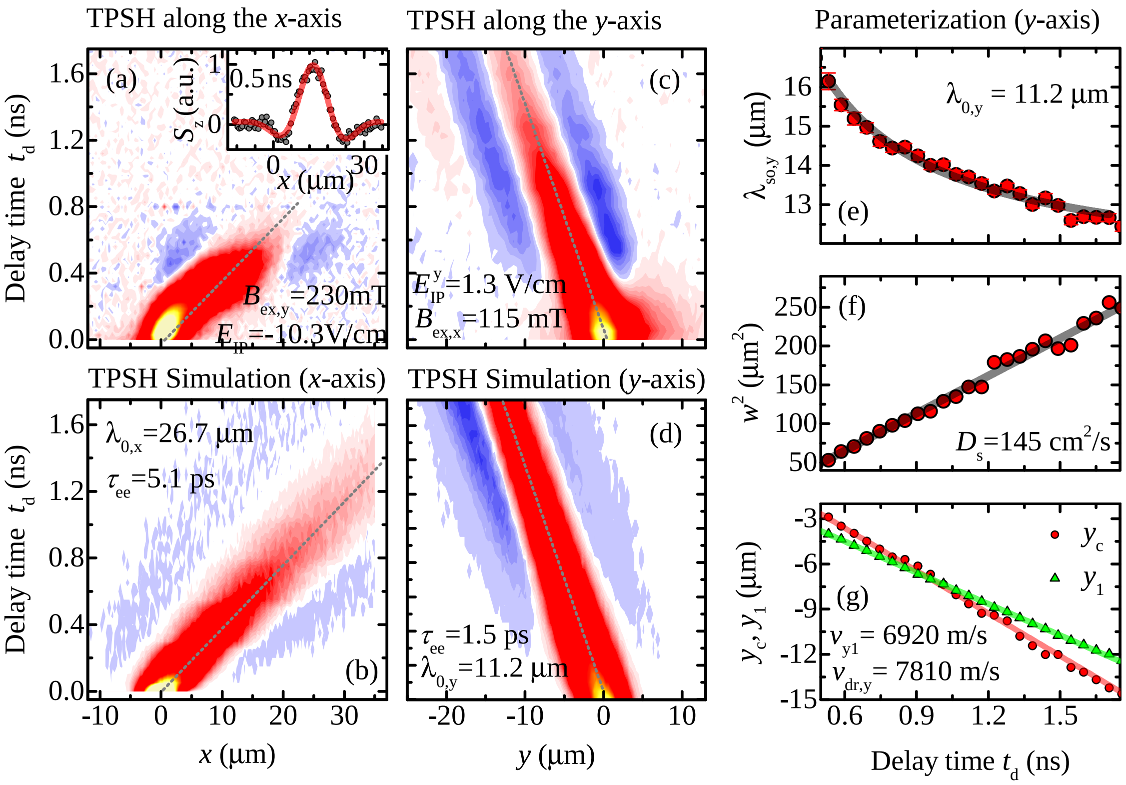

Fig. 3.17: **(a,c)** Spatiotemporal appearance of the TPSH along the y- and x-axis in false-color representation respectively. An individual cutout line is taken out from the x-axis TPSH and depicted as inset in panel (a). **(e-g)** Fit parameters that are extracted from the y-axis spatiotemporal measurement. The resulting TPSH parameters are integrated into the MC simulation shown in **(b,d)**.

of the SO coupling parameters and hence generally weaker than along the y-axis. This leads to longer spin precession length and thus no precession can be detected along the x-axis in the PSH. However, this limitation is overcome in the TPSH regime. Here, the application of in-plane field has been shown to yield an enhanced diffusion coefficient which enables the polarization to spread further around its center and reach length scales for which oscillations are detectable.

Figure 3.17 (a) shows a false-color plot representation of a spatiotemporal measurement of a TPSH along the x-axis. Aiming at fast diffusion, a strong field of $E^{\mathrm{x}}_{\mathrm{IP}} = 10.3\,\mathrm{V/cm}$ is chosen. This field strength corresponds to the highest possible effective magnetic field that can be canceled by the external electromagnet, being tuned to $B_{\mathrm{ex,y}} = 231\,\mathrm{mT}$. Due to the high electric field and a corresponding diffusion coefficient as high as $D_{\mathrm{s}} = 473.1\mathrm{cm}^2/\mathrm{s}$ the TPSH lifetime is somewhat limited. This causes the signal to be decayed before $t_{\mathrm{d}} = 800\,\mathrm{ps}$. Nevertheless, the characteristic appearance of the TPSH as a symmetric spin pattern that evolves around a continuously drifting center is present in the false-color plot. This is warranted by the almost equal drift and phase velocities $v_{\mathrm{dr,x}} = 26.9\,\mathrm{km/s}$ and $v_{\mathrm{y1}} =$

25.8 km/s. As a result, it is possible for the first time to monitor a symmetric cutout line at $t_\mathrm{d} = 506\,\mathrm{ps}$ for the x-axis with clear oscillatory features as visible in the inset of the (a) panel. From a best fit of this line scan with Eq. (3.3) a spatial precession length of $\lambda_\mathrm{so,x} = 28.3\,\mu\mathrm{m}$ is obtained and used to calculate the TPSH mode $\lambda_\mathrm{0,x} = 26.7\,\mu\mathrm{m}$ by employing Eq. (3.4). An extraction of $\lambda_\mathrm{0,x}$ from a single value does not reach the same fidelity as a fit of $\lambda_\mathrm{so,x}(t_\mathrm{d})$, yet, a good estimate is feasible. The TPSH mode $\lambda_\mathrm{0,x}$ can be transformed in the corresponding difference of the Rashba and Dresselhaus parameter by Eq. (3.9), yielding $(-\alpha + \beta) = 1.40\,\mathrm{meV\AA}$. This value represents an increase compared to the outcome of $(-\alpha + \beta) = 1.15\,\mathrm{meV\AA}$ stated from measurements with magnetic field only (cf. Fig. 3.6). The discrepancy is attributed to the effect of in-plane electric fields on the SO coupling (cf. Fig. 3.10). Remarkably, the change of $\lambda_\mathrm{0,x}$ is smaller for the same electric field strength in the TPSH regime than in the DPSH case.

The comparably longer precession length of the TPSH suggests a possibly different influence of the in-plane electric field when compared with results from the DPSH in Section 3.3.2. In order to clarify this observation, the TPSH is analyzed by tuning the in-plane electric field strength while the external magnetic field remains fixed. Particular attention is paid to the specific electric field $E^\mathrm{y}_\mathrm{TPSH}$ for which a perfect TPSH with balanced effective and external magnetic fields is expected. This approach aims at the identification of peculiar PSH characteristics that are only enabled by the special regime of the TPSH.

An exemplary measurement is displayed in Fig. 3.18 (a) where the delay time is set to $t_\mathrm{d} = 1595\,\mathrm{ps}$ and a constant external magnetic field of $B_\mathrm{ex,x} = 143\,\mathrm{mT}$ is applied. The false-color plot shows the spin precession pattern along the y-axis throught a varying field range of $E^\mathrm{y}_\mathrm{IP} = -(3.0 - 0.0)\,\mathrm{V/cm}$. This range is distributed around the field value of $E^\mathrm{y}_\mathrm{TPSH} = 1.42\,\mathrm{V/cm}$ necessary to achieve TPSH conditions. Additionally, Fig. 3.18 shows the in-plane field dependence of $\lambda_\mathrm{0,y}$ (i), D_s (ii) and v_y1 (iii) extracted from three measurements of the kind shown in panel (a). For the three experiments at $t_\mathrm{d} = 1595\,\mathrm{ps}$ the external magnetic field is set to 0 mT (red), 28 mT (green) and 86 mT (blue) respectively.

As discussed above, the conditions for a TPSH are fulfilled when the drift velocity matches the gradient of the cosine offset parameter v_y1. The corresponding field $E^\mathrm{y}_\mathrm{TPSH}$ is determined for each parameter set individually from the panels (a,iii) , (b,iii) and (c,iii). These panels depict the field dependence of the drift velocity and the phase velocity. On the one hand, v_dr (black) is independent of the external magnetic field yet changes linearly with the applied field strength. On the other hand, v_y1 is mainly set by the magnetic field whereas the electric field has only a minute influence via the cubic Dresselhaus parameter (cf. Fig. 3.9 (g)) that is negligible in this context. As a result, the drift velocity data are unchanged in all three panels while the constant phase velocity is vertically shifted with the applied magnetic field. Accordingly, $E^\mathrm{y}_\mathrm{TPSH}$ is obtained from the intersections where $v_\mathrm{y1} = v_\mathrm{dr}$. Here, values of $E^\mathrm{y}_\mathrm{TPSH}(0\,\mathrm{mT}) = 0\,\mathrm{V/cm}$, $E^\mathrm{y}_\mathrm{TPSH}(28\,\mathrm{mT}) = -0.3\,\mathrm{V/cm}$ and $E^\mathrm{y}_\mathrm{TPSH}(86\,\mathrm{mT}) = -1.1\,\mathrm{V/cm}$ are found and indicated by black dashed lines which span each column respectively. These pairs of magnetic and electric field values are in good agreement with the model in Eq. (3.28).

Looking for an effect related to the TPSH regime the parameters $\lambda_{0,\mathrm{y}}$ and D_s are calculated from single fit parameters and depicted in the same figure for each magnetic field respectively. Here, special interest is paid to the values of E_IP^y that are marked by a black line in each column of the figure. The red data set was recorded without an external magnetic field and is intended to serve as a comparison, i.e., it represents a trivial TPSH with zero velocity. The set is equivalent to the data discussed already in the DPSH Section in Fig. 3.9. In the DPSH section it was found that the $\lambda_{0,\mathrm{y}}$ values in panel (a,i) form a peak that is centered around zero in-plane field. Subsequently, the trend was reproduced by a best fit with an absolute value function. At the same time, the diffusion coefficient, calculated from the squared width of the spin ensemble at $t_\mathrm{d} = 1595\,\mathrm{ps}$ and depicted in (a,ii), reveals a negative peak that is modeled by a Gaussian function with negative amplitude and positive intercept. The center of this trough coincides with the peak of $\lambda_{0,\mathrm{y}}$ at $E_\mathrm{IP}^\mathrm{y} = 0\,\mathrm{V/cm}$. Remarkably, the peak in $\lambda_{0,\mathrm{y}}$ and the trough in D_s are jointly shifted as the magnetic field is set to $28\,\mathrm{mT}$ and $86\,\mathrm{mT}$. This trend is clearly visible in the green and blue data sets of the figure. Furthermore, the center position of the peak and trough can be correlated with $E_\mathrm{TPSH}^\mathrm{y}$. Although, the overlap of peak and through are not in perfect agreement for $B_\mathrm{ex,x} = 86\,\mathrm{mT}$ they are both clearly shifted to higher field strength when compared to the other columns.

This observation underlines the specificity of the TPSH configuration which influences the parameters of the spin pattern beyond the ability of separately applied magnetic or electric fields. The data shown in Fig.3.18 indicate a recalibration of already known PSH characteristics which no longer change symmetrically around $E_\mathrm{IP}^\mathrm{y} = 0\,\mathrm{V/cm}$, but around the respective electric field $E_\mathrm{TPSH}^\mathrm{y}$. This idea connects with the qualitative discussion of the scheme in Fig. 3.15. In this scheme the TPSH was introduced as a standard-like PSH that evolves in a moving frame around the drifting center of the spin polarization while the real standard PSH evolves in the lab frame with fixed $y_\mathrm{c} = 0\,\mu\mathrm{m}$.

For a final validation of the proposed trend a more detailed analysis is inevitable since a variety of questions is raised by the studied data. For instance, it is not clear how the combined magnetic and electric fields act on the electron spins to change their diffusion behavior. While possible influences of the electric field, such as heating and electron hole separation, are discussed in Section 3.3.2 it is unanswered how an additionally acting magnetic field interferes with these effects. Firstly, a feasible mechanism could be related to pure spin diffusion that must be considered in addition to the classical carrier diffusion. In this case, an influence of the PSH specific SU(2) symmetry on the spin diffusion process is conceivable. Secondly, the effective magnetic field, seen by the majority of spins, and the corresponding symmetry is affected differently in the case of DPSH and TPSH and might explain the trend seen in panel (a,ii), (b,ii) and (c,ii) of Fig. 3.18. Thirdly, it must be considered that the discussed data for $\lambda_{0,\mathrm{y}}$ are derived from a single temporal snapshot of precession length $\lambda_{\mathrm{so,y}}$ and D_s extracted both from one $S_\mathrm{s}(y)$ curve for a given in-plane field. The diffusion coefficient in turn is derived from the according fit parameter $w^2(t_\mathrm{d})$. This approach presupposes a linear spread of the distribution for the entire time of the TPSH evolution. However, it is possible that

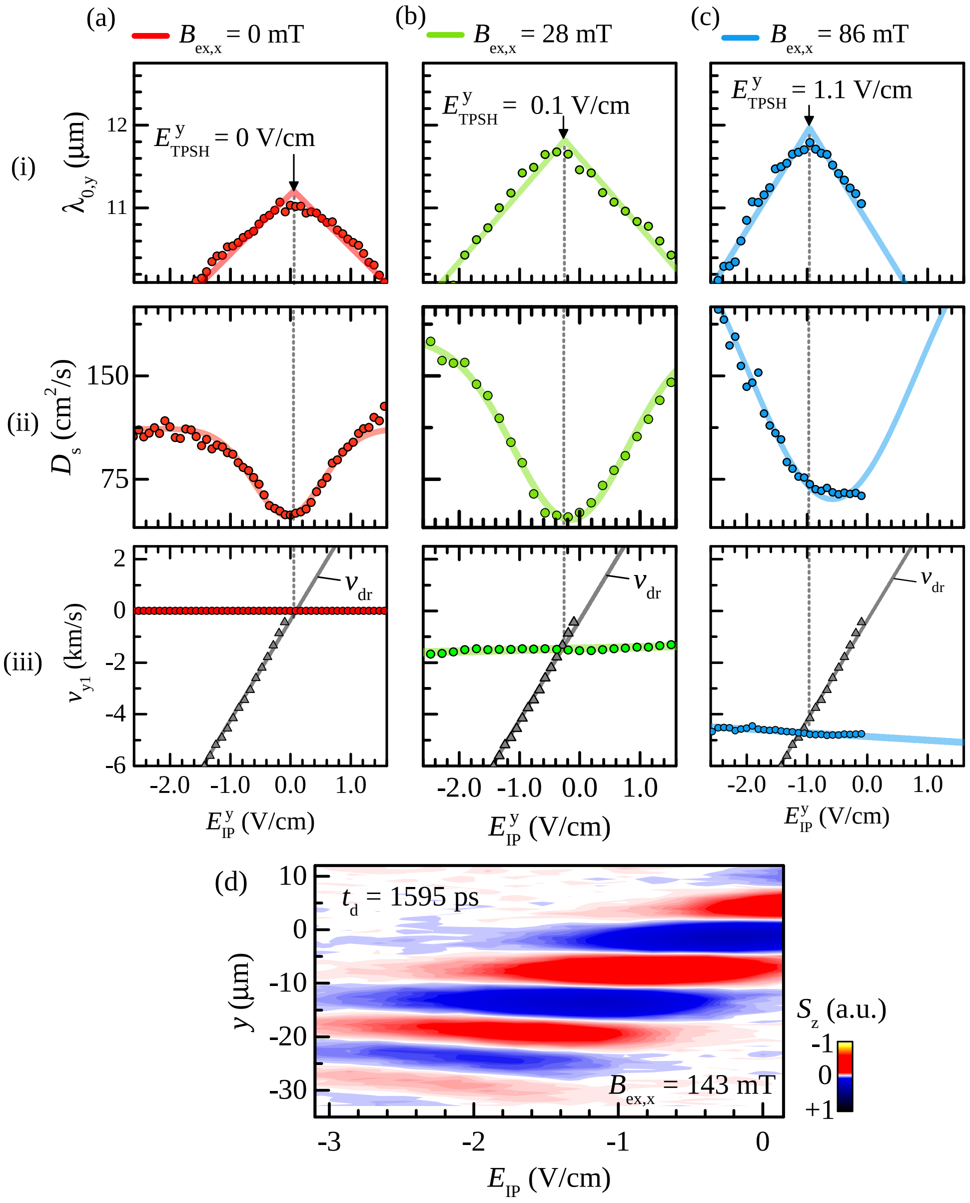

Fig. 3.18: TPSH parameter analysis for a detuning of the in-plane electric field around E^{y}_{TPSH}. **(a)** False-color plot representation of the spin pattern for fixed $t_d = 1595\,\text{ps}$ and $B_{ex,x} = 143\,\text{mT}$. **(b)** Identification of E^{y}_{TPSH} from three measurements with different applied magnetic field $B_{ex,x}$ represent by the colors red, green and blue. Grey circles highlight the TPSH conditions from a combined representation of drift and phase velocity in dependence on E^{y}_{IP}. **(c-d)** PSH mode $\lambda_{0,y}$ and the diffusion coefficient extracted from the same measurements as in (b) respectively. The peak and trough like trends in the data sets are fit with absolute value functions ($\lambda_{0,y}$) and Gaussians (D_s). Grey bars mark the electric fields for which the TPSH requirements are met.

non-linear effects, such as charge separation, appear during the diffusion. This would decrease the validity of the presented data. The limitation has to be taken into account when another interesting feature of the $\lambda_{0,y}$ trend in the precession length is discussed in the following.

So far it was observed that an increasing in-plane electric field strength is accompanied by a downward trend in $\lambda_{0,y}$. The individual three data sets in (a,ii), (b,ii) and (c,ii) generally reproduce this peak-like behavior centered around $E^{\mathrm{y}}_{\mathrm{TPSH}}$. However, an increase in the peak value of $\lambda_{0,\mathrm{y}}$ at $E^{\mathrm{y}}_{\mathrm{TPSH}}$ with raised magnetic field strength is visible. The peak height in the panels is increasing from $11.2\,\mu$m (red) to $11.8\,\mu$m (green) and further to $12.0\,\mu$m (blue). This trend is highly interesting as it implies a tunability of the SO coupling with reversed sign compared to the application of in-plane fields only. For the DPSS it was seen that the precession length becomes smaller for higher fields and thus $(\alpha + \beta)$ is assumed to increase (cf. Fig. 3.9). This effect of E_{IP} on the SO coupling seems to be drastically changed by the TPSH regime.

Outlook for a device oriented application of the TPSH

In the previous section, the TPSH manipulation scheme was introduced, enabling complete control over the spin orientation of a PSH during transport in a 2DEG. This control is based on locking the spin orientation with a precisely tailored external magnetic field. In this final part of the section, the TPSH is embedded in a Hall Bar geometry that allows the proposal for a prototype spin transistor design. Despite all the difficulties in realizing spintronic devices and despite the fact that spin transistors have already been demonstrated with a variety of materials and mechanisms, this idea should serve as an inspiration. In particular, the considerable advantages of the TPSH compared to earlier proposals in similar systems are pointed out.

Inspired by the spin field-effect transistor design, envisioned by Data and Das [18] some 30 years ago, a variety of concepts for spin information processing on the transistor level have been discussed in literature. Many fundamental issues, such as low spin-injection efficiency, spin relaxation and spin precession decoherence, are still mayor challenges for the field. Regardless of this, it is generally accepted that SO coupling effects and the related effective fields have to be fully controlled in a way that they can be integrated in the device architecture. This is beyond question for devices that directly harness the SO related Spin Hall effect [145]. However, it is likewise true for transistors based on an all-electric all-semiconductor approach [146] or transition metal dichalcogenides such as MoSe_2 [147]. In the latter concept, SO related valleytronics plays an important role for the functionality. Against this background, a transistor design close to the one proposed here was already introduced by Wunderlich *et al.* [148]. For this device design the Spin Hall effect (SHE) is important as it allows for the electrical generation and detection of spin currents. The related theory was predicted by Dyakonov an Perel [31] already 40 years ago. Generally, the SHE describes the appearance of a spin current transverse to an electrical current in systems where the conducting electrons experience SO coupling from electric field gradients of unpolarized impurities. As a result, a spatial separation of spins with opposite spin polarization is achieved. The so-called Mott scattering results in a Hall effect as the axis of separation is perpendicular to the electrical bias direction which can be used to create charge gradients in a Hall bar cross if a majority spin polarization exists among the electrons. For further theoretical background and experimental evidence the reader is referred to literature [32; 149].

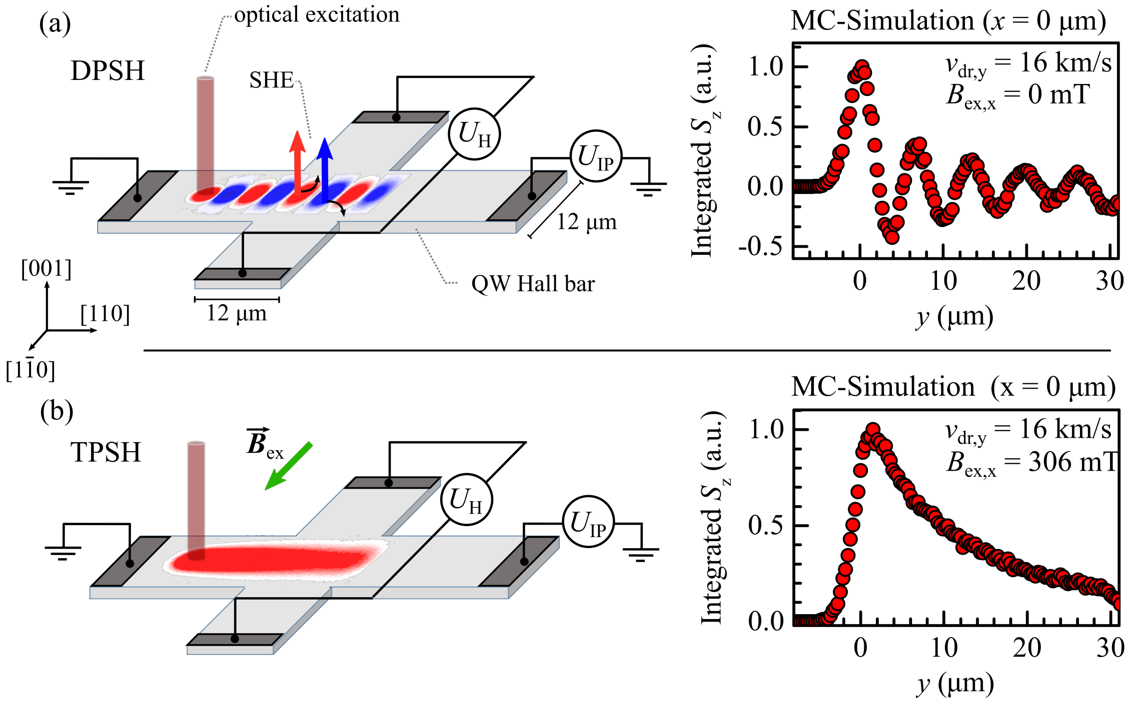

Fig. 3.19: Fundamental architecture of a spin transistor prototype based on the SHE. **(a)** A propagating DPSH spin pattern inhibits an effective buildup of Hall voltage U_H. **(b)** The TPSH configuration can be employed to achieve a design that is insensitive to SO induced precession. Cutout transients on the right hand depict the integrated and normalized spin polarization at $x = 0\,\mu$m.

The general functionality of a spin based transistor that combines the SHE with the PSH is schematically illustrated in Fig. 3.19 (a) where a Hall bar cross is depicted on the left side. Similar to the investigated GaAs structure (cf. Fig. 2.3) a spin polarization is excited all-optical and away from the intersection. Subsequently, the spin package is transported by an in-plane electric field generated by an applied voltage U_{IP}. While the spin polarization passes through the intersection a second voltage can be measured perpendicular to the direction of drift. This voltage U_H represents the charge gradient created by the SHE. Thus the polarization of the detected potential is directly determined by the spin orientation of the propagating electrons. On the surface of the Hall bar scheme in 3.19 (a) a 2Dmap MC simulation of a DPSH spin pattern is shown. The simulation is based on the parameter set of the GaAs sample studied in this thesis an resembles a picture of the spin polarization integrated over the period $t_d = (0.0 - 2.0)$ ns with a temporal resolution of 0.05 ns. It is composed from the superposition of 2Dmaps for different delay times generated by a MC simulation with $v_{dr,y} = 16$ km/s. Such a superposition models an experimental scheme with a continuous spin excitation. In this scheme, spin precession due to diffusion plays only a minor role for the overall spin orientation. This is due to a long $\lambda_{so,x}$ and an averaging effect that inhibits a flip of the spin polarization along the y-direction. The characteristic spin precession around the effective magnetic field is clearly present and the spatial precession length is similar to the

Hall bar dimensions. This is further confirmed by the transient cutout line at $x = 0\,\mu$m displayed on the right hand of the figure. In this configuration, the spin polarization within the intersection is neither homogeneous in time nor in space due to the spatiotemporal precession. This modulation of S_z represents a severe challenge for the detection of voltage within the SHE that relies on spatial deflection of electrons in dependence on their spin orientation. It is likely that the precession diminishes the measurable voltage or even inhibits the detection at all as the fluctuating direction of the deflection averages the charge accumulation to zero.

An additional effect, seen in the work of Wunderlich *et al.* [148], is a sign dependence of U_{IP} on the y-axis position of optical excitation. This is explained by a translation of the SO induced precession pattern in parallel with the spot of excitation. A change in the pattern is accompanied by a change in the dominant spin polarization within the intersection. This sensitivity to the geometry of excitation and the problematic influence of spin precession due to effective magnetic fields can be overcome by introducing a TPSH regime to the setup design.

The integrated spin polarization for the TPSH regime is illustrated in the bottom part (b) of Fig. 3.19 where the same parameters as in the top panel are extended by a magnetic field $B_{\mathrm{ex,x}} = 306\,\mathrm{mT}$ in order to create the MC simulation. The resulting false-color plot uncovers the advantage that arises from a locked spin polarization due to disabled SO coupling. When the external magnetic field is switched on, the spin polarization remains constant during the entire passage through the Hall bar intersection. In this case, the measurement of U_{H} does not suffer any longer from spin precession and the sign can be expected to be robust against changes in the excitation position. In addition, the sign of the Hall voltage read out is now determined by the originally excited spin orientation. Therefore, it can be controlled by the optical polarization of the laser pulse, leading to the desired switch that operates on electron spins.

Chapter 4

Summary

In the introduction to this thesis, the importance of spin-orbit coupling for the field of spintronics was outlined and supported by a variety of exemplary phenomena. Motivated by this impact, the persistent spin helix is identified as an attractive model system for understanding SO coupling phenomena in topological and quantum matter. Previous studies documented the emergence of the PSH texture in a regime where Dresselhaus and Rashba contributions are of similar strength. This prior work showed a good agreement of the theoretical model with corresponding experimental observation. However, these studies were either insensitive to temporal dynamics or limited to the investigation of single parameter dependences with insufficient consideration of interconnections. In addition, the experimental field of PSH research is centered around GaAs 2DEG structures only, leaving out the universal character of this spin texture.

By investigated the spin helix in two materials, the present thesis extents the understanding of SO coupling effects to the unstudied material CdTe while topical issues are addressed in the better understood material GaAs. Especially, the high mobility GaAs sample enabled the simultaneous optimization and study of operating conditions and system parameters, including the Fermi energy, the diffusion coefficient, electric drift and gate fields and not least the Rashba and Dresselhaus parameters themselves. On the one hand, the complex mutual dependences of this tuning knobs in GaAs allowed for a comparative study close to the most recent results reported under similar conditions in literature. On the other hand, additional effects were discovered in CdTe where optical doping is identified as a novel tuning mechanism. An overview about the most striking results of this study are compiled in Fig. 4.1.

In summary, the SO coupling parameters α and β are found to tune with the electric field applied to the 2DEG within the GaAs QW via a back gate. By studying the spatial precession lengths $\lambda_{0,\mathrm{x}}$ and $\lambda_{0,\mathrm{y}}$ along the $[1\bar{1}0]$ and $[110]$ directions the sum, difference and individual values of α and β are extracted (cf. Chapter 3.3.3). Moreover, the Dresselhaus parameter can be separated in a linear and cubic contribution due to a theoretical calculation of β_3 from the Fermi energy which is accessible by means of PL measurements (cf. Chapter 3.1). All obtained parameters are given in Fig. 4.1 (a) where the effect of an increasing gate field on the SO coupling is depicted. A pronounced decrease of the Rashba parameter with increasing U_{BG} confirms the direct relation of α with the external electric field E_{QW} across the heterostructure. A close to constant value for β_1 is found in agreement with the theory model whereas the increase of β_3 is attributed to electron density tuning via U_{BG}. As a result of the simultaneous variation of density and the α/β ratio, the spin lifetime shows a peak-like dependence on U_{BG}. In general, the back gate allows for direct modification of the Rashba SO coupling, making it an advantageous tuning knob for spintronics. On the contrary, the diffusion coefficient $D_{\mathrm{s}} = \tau_{\mathrm{ee}} E_{\mathrm{F}}/m^*$ is not significantly altered by U_{BG}. This is explained by a canceling of simultaneous changes in E_{F} and the scattering time τ_{ee} with increasing electron density.

Furthermore, spatiotemporal analysis of the spin polarization as a function of in-plane electric and magnetic fields shows multiple modifications of the PSH pattern. Until now, the negligible precession of spins traveling perpendicular to the spin helix pattern prevented the extraction of the difference $(-\alpha + \beta)$. By tilting the spatiotemporal evolution of the spin patter with magnetic fields applied along the $[1\bar{1}0]$ and $[110]$ this drawback can be removed. Accordingly, the individual Rashba and Dresselhaus parameters can be accessed with high precession. Despite the direct interaction of effective and external magnetic fields, a dependence of the SO coupling on the applied field strength was not observed. However, a strong effect on the SO parameters is found for anisotropic spin transport where in-plane electric fields reveal a tunability of the spin precession length $\lambda_{0,\mathrm{y}}$. Figure 4.1 (b) depicts the related increase of $(\alpha + \beta)$ with field strength and a similar trend is found for $\lambda_{0,\mathrm{x}}$ and $(-\alpha + \beta)$ (cf. Fig. 3.10). In general, this thesis presents a first in-depth analysis of spin drift perpendicular to the spin helix pattern. Such fields reveal oscillations along $[1\bar{1}0]$ which could not been detected in purely diffusive experiments, allowing for the extraction of $(-\alpha + \beta)$ from the spin precession length $\lambda_{0,\mathrm{x}}$ without the need for an external magnetic field. Moreover, oscillations along the x-axis enable the extraction of β_3 from temporal precession which is induced by external drift fields, having been seen previously along the y-axis only. Besides this, the comparatively high drift fields along the x-direction reveal a peculiar tuning of the diffusion coefficient. This enhancement of almost an order of magnitude for the highest fields of $\sim 13\,\mathrm{V/cm}$ is discussed as a result of intensive 2DEG heating and linked with a drastic decrease of the spin lifetime that occurs simultaneously. The latter result warrants further study because an effect of electric field induced electron hole separation on diffusion and mobility cannot be ruled out.

Chapter 3.3.4 reports on the first experimental demonstration of the PSH formation in a 2DEG that is hosted in a II/VI material, namely a high mobility CdTe QW sample. Confirming the universality of the PSH, the SO coupling is found to be close to a perfectly balanced regime, featuring a ratio of $\alpha/\beta = 1.3$. The characteristic PSH evolution is well comparable to the behavior in GaAs and allows for the extraction of a diffusion coefficient and the Rashba and Dresselhaus parameters, employing the already developed methods. It is found that a locally injected distribution of photocarriers affects the SO coupling parameter and the diffusion coefficient. This relation is modeled with a Gaussian distribution of electrons in space that translates into a gradient in the Rashba and cubic Dresselhaus parameters. While the

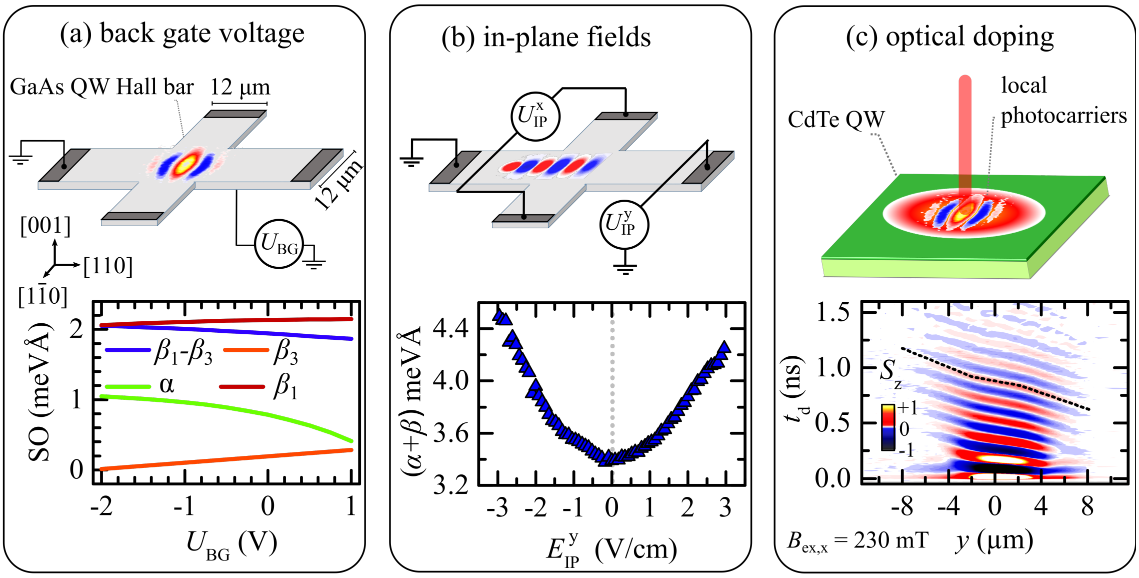

Fig. 4.1: Overview of manipulation schemes studied in the present thesis. **(a)** Application of back gate voltage allows for tuning of α and β_3. **(b)** By applying voltage to the Hall bar structure, the spins can be translated along the QW, leading to a strong variation of the summed SO parameters. **(c)** Optical doping of the CdTe sample results in a local gradient of the Rashba and cubic Dresselhaus parameters, manifesting as *s*-like shaped polarization stripes in the spatiotemporal maps with applied external magnetic field.

change in α is explained by screening effects of the internal electric fields, β_3 is changed by a local elevation of the Fermi energy. This considerations arise from a *s*-like distortion of the polarization stripes in spatiotemporal maps with applied external magnetic field as displayed in Fig. 4.1 (c). In order to validate the proposed model, the spin precession is studied in dependence on the optical intensity, i.e., the photocarrier density. Subsequently, the results are successfully compared with kinetic theory simulations that incorporate local perturbations due to photocarriers, making α and β dependent on time and space. The finding of a precession length that can be modified all-optical by the laser intensity is an important key for a control of SO coupling in semiconductor nanostructures.

As an attempt to combine the developed tuning mechanisms, Chapter 3.4 is centered around a precisely tailored application of in-plane magnetic and electric fields, resulting in a locked spin orientation during transport in the GaAs structure. The so-called traveling PSH resembles a standard diffusive evolution of the spin orientation symmetrically around the center of the distribution. However, in the TPSH the center of the spin distribution itself propagates in space. The pattern is realized along the y- and the x-axis, implying full control over the spin polarization in time and space (cf. Fig. 3.17). A study of the diffusion coefficient and the spatial precession length in dependence of electric field strength reveals a simultaneous shift of a peak in $\lambda_{0,\mathrm{y}}$ and a trough in D_s with the specific field $E^\mathrm{y}_\mathrm{TPSH}$ (cf. Fig. 3.18). The field $E^\mathrm{y}_\mathrm{TPSH}$ denotes the required field for the emergence of the TPSH and thus needs to be adjusted to the fixed external magnetic field strength. It is, therefore, concluded that the traveling spin helix regime provides a special environment for the spatiotemporal spin evolution, including a changed influence of in-plane fields on the SO coupling. Here, the interplay of electric fields and the SU(2) symmetry of the effective magnetic fields has to be studied further by both experimental and theoretical means. Nevertheless, the TPSH forms the core part of a proposal for a novel spintronics switching device proposed in the end of Section 3.4. The general device structure is based on a previously developed design that harnesses the spin hall effect. By including the TPSH spin locking this switching device can be improved and restrictions that arise from precession around effective magnetic fields are removed.

Appendix A

Simulations

A.1 Kinetic Theory

The Theoretical Background Section 1.3 combines spatial and temporal spin dynamics in order to find a theoretical model for the PSH. This appendix will promote a more complete description for the dynamics of a spin ensemble exposed to external electric $\boldsymbol{\mathcal{E}}$ and magnetic fields $\boldsymbol{B}$. As a result, an extended version of the drift-diffusion equation is obtained. Subsequently, this partial differential equation can be solved numerically in order to create the simulations presented in the Experimental Results Chapter 3 of this thesis. Next to this numerical approach, analytical solutions can be realized due to Fourier transforming the correlation function of spin polarization at different spatial positions as shown in literature [42; 55].

Starting from the vector of spin polarization $\boldsymbol{S} = (S_\mathrm{x}, S_\mathrm{y}, S_\mathrm{z})$ attributed to an ensemble of spins, the main mechanisms, acting on $\boldsymbol{S}$ are joined in the drift-diffusion equation

$$\frac{\partial}{\partial t}\boldsymbol{S} = \underbrace{\boldsymbol{\Omega_0} \times \boldsymbol{S}}_{\text{precession}} + \underbrace{D_\mathrm{s} \triangle \boldsymbol{s}}_{\text{diffusion}} + \underbrace{\mu_\mathrm{e} \boldsymbol{\mathcal{E}} \cdot \nabla \boldsymbol{S}}_{\text{drift}} - \underbrace{\boldsymbol{S}/T_\mathrm{s}}_{\text{relaxation}} \tag{A.1}$$

where $\boldsymbol{\Omega_0} = (\Omega_\mathrm{x}, \Omega_\mathrm{y}, \Omega_\mathrm{z})$ denotes the vectorial Larmor precession frequency of a spin in an external magnetic field, μ_e is the electron mobility, D_s is the spin diffusion coefficient and T_s is the spin lifetime. Moreover, for a full description of the PSH it is vital to consider the momentum-dependent precession of spins around the effective magnetic field which arises from Rashba and Dresselhaus SO coupling (cf. Section 1.3.4). Due to the anisotropic distribution of these effective magnetic fields in k-space, the spin precession has to be described by a tensor $\boldsymbol{\Lambda}$ with elements derived from Eq. (1.29). For the same reason, the isotropic dephasing proposed in Eq. A.1 has to be replaced by a tensor, namely the Dyakonov-Perel spin-relaxation-rate tensor $\boldsymbol{\Gamma}$. Accordingly, the complete spin distribution dynamics in two dimensions is modeled by the expression

$$\frac{\partial}{\partial t}\boldsymbol{S} = (\boldsymbol{\Omega_0} + \boldsymbol{\Omega}_\mathrm{dr}) \times \boldsymbol{S} + D_\mathrm{s}\frac{\partial^2 \boldsymbol{S}}{\partial \boldsymbol{r}^2} - \boldsymbol{\Gamma}\boldsymbol{S} - \left(\boldsymbol{v}_\mathrm{dr} \cdot \frac{\partial}{\partial \boldsymbol{r}}\right)\boldsymbol{S} - \left(\boldsymbol{\Lambda}\frac{\partial}{\partial \boldsymbol{r}}\right) \times \boldsymbol{S} \tag{A.2}$$

with

$$\mathbf{\Gamma} = \left\{ \begin{matrix} D_\mathrm{s}[2m^*(\alpha-\beta)/\hbar^2]^2 & 0 & 0 \\ 0 & D_\mathrm{s}[2m^*(\alpha+\beta)/\hbar^2]^2 & 0 \\ 0 & 0 & 2D_\mathrm{s}(2m^*/\hbar^2)^2 \cdot (\alpha^2+\beta^2) \end{matrix} \right\} \tag{A.3}$$

and

$$\mathbf{\Lambda} = \begin{bmatrix} 0 & 4D_\mathrm{s}m^*(\alpha+\beta)/\hbar^2 & 0 \\ -4D_\mathrm{s}m^*(\alpha-\beta)/\hbar^2 & 0 & 0 \\ 0 & 0 & 0 \end{bmatrix} \tag{A.4}$$

where $\boldsymbol{r} = (x, y)$ denotes the position vector. In addition to the precession around an external field, a second precession frequency $\mathbf{\Omega}_\mathrm{dr}$ has to be taken into account as the spins precess in the effective magnetic field created by the drift momentum. Equation A.2 can be solved numerically for experimentally determined Rashba and Dresselhaus parameters α and β. Remarkably, the equation enables a versatile application of combined external electric and magnetic fields as presented in the results section of this work. In summary, the kinetic equation represents a powerful tool for the generation of simulated data. Such predictions can be visualized and thus allow for a comparison with empirically obtained data. The degree of overlap in between simulation and experiment facilitates a validation of the PSH model developed in Section 1.3.4 and 1.3.5.

A.2 Monte Carlo Simulation

Complementary to the kinetic theory, the Monte Carlo (MC) method provides an equivalent approach for the theoretical simulation of spin dynamics. In general, the MC method is commonly used in computational algorithms as it permits to solve deterministic problems where the need for complex calculation can be bypassed through a large number of random samplings. From a stochastic point of view, this approach is favorable when the law of large numbers allows for the substitution of a hard to determine parameter with an approximated mean value. In comparison with the analytical solving of a differential equation a MC simulation demands a much higher expense in computational calculations. However, often times MC based algorithms can be formulated with less effort since the calculation of complicated physical effects can be avoided in favor of random sampling. In particular, the spatial evolution of an excited spin ensemble can be described by a MC model. For this purpose, the diffusion of the spin carrying electrons is modeled as the result of consecutive elastic scattering events followed by a random redirection of the electrons velocity vector. Recent publication have shown that the MC algorithm is a suitable tool for the validation of the PSH evolution in general [124] and as well for rather small features predicted by theory [54; 150; 151].

The specific Monte Carlo algorithm employed for the simulations presented in this thesis is discussed qualitatively in the following. The MC algorithm accumulates the iterative pathway of upto 1×10^6 virtual electrons, traveling with the constant Fermi velocity which can be obtained directly from the electron density via $v_\mathrm{F} = \hbar\sqrt{2\pi n_\mathrm{e}}/m^*$. Assuming the electron

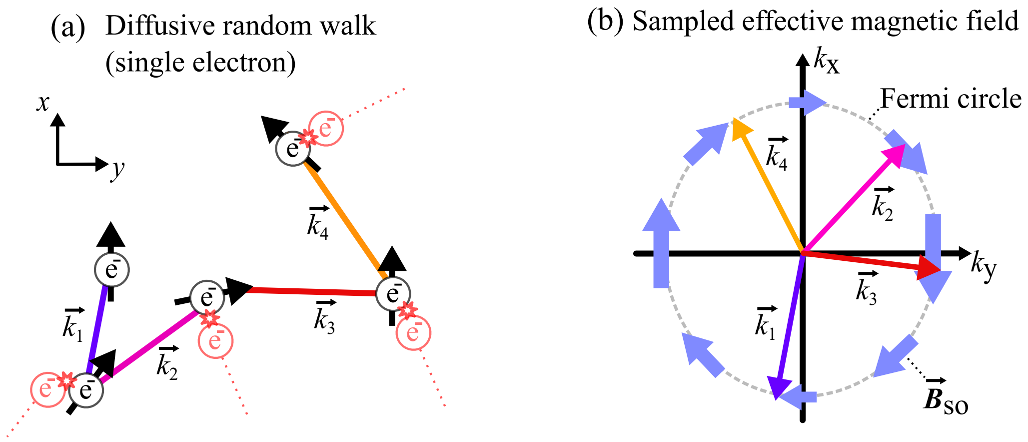

Fig. A.1: Fundamentals of MC based simulations of the PSH evolution. **(a)** Schematic random walk of a single spin carrying electron. The attributed wave vector experiences a redirection due to each scattering event indicated by a star-like symbol. The corresponding reorientation of the wave vector on the Fermi circle is illustrated in **(b)**.

velocity to be constant is a reasonable approach within the Fermi-Dirac regime where the occupied states for non-localized carriers are restricted to a small energy band around the Fermi energy. For increased temperatures where this energy band is smeared out a distribution of velocities, in accordance with the Boltzmann statistics, must be applied. Figure A.1 (a) visualizes a schematic random walk in the QW plane where the electron experiences an elastic scattering event after having traveled for the free mean path $l = v_\mathrm{F}\tau$ given by the scattering time. The scattering time is individually drawn from an exponential distribution which has a probability density that is given by

$$f(t, \tau_\mathrm{ee}) = \frac{1}{\tau_\mathrm{ee}} e^{-t/\tau_\mathrm{ee}} \tag{A.5}$$

where τ_ee is the electron momentum relaxation time. This sampling accounts for the fact that the time in between two scattering events is not a constant value but exhibits a stochastic variation. The momentum relaxation time can be obtained from the experimentally observed diffusion coefficient given by $D_\mathrm{s} = \tau_\mathrm{ee} v_\mathrm{F}^2/2$. As a result of scattering the wave vector $\vec{k}$ of the electron is rotated on the two-dimensional Fermi circle in k-space depicted in Figure A.1 (b) and hence the electron continues its travel along a different direction. The rotation of the wave vector is approximated by a random rotation angle φ taken from a uniform distribution from π to $-\pi$. The effective magnetic field, seen by the electron spin during the unperturbed propagation between two scattering events, is taken as constant. However, recalling Eq. (1.27) it has been shown that Rashba and Dresselhaus SO coupling is momentum-dependent and consequently $\boldsymbol{B}_\mathrm{so}$ will change together with the wave vector after each event of scattering. Therefore, it is necessary to calculate the three-dimensional rotation for each spin polarization vector $\boldsymbol{S} = (S_\mathrm{x}, S_\mathrm{y}, S_\mathrm{z})$ individually. The axis of rotation is given by the effective field vector

$\boldsymbol{B}_{\mathrm{so}}(k_{\mathrm{x}}, k_{\mathrm{y}})$ that acts as a torque on the spin momentum for each iteration i as

$$\begin{pmatrix} S_{\mathrm{x}} \\ S_{\mathrm{y}} \\ S_{\mathrm{z}} \end{pmatrix}_{(\mathrm{i}+1)} = \boldsymbol{R}\left(\frac{\boldsymbol{B}_{\mathrm{so,i}}}{|\boldsymbol{B}_{\mathrm{so,i}}|}, \Omega_{\mathrm{so,i}}\tau\right) \cdot \begin{pmatrix} S_{\mathrm{x}} \\ S_{\mathrm{y}} \\ S_{\mathrm{z}} \end{pmatrix}_{\mathrm{i}} \tag{A.6}$$

where $\boldsymbol{R}(\boldsymbol{T}, \theta)$ is a standard three-dimensional rotation matrix which rotates a vector around the axis $\boldsymbol{T}$ by the angle $\theta = \Omega_{\mathrm{so}}\tau$. The angle of rotation is the accumulated Larmor precession between to scattering events. Within the MC simulation the resulting vector of spin polarization is tracked together with the current position and wave vector of each electron. Hence, the spatial position of each iteration step is obtained from

$$\begin{pmatrix} x \\ y \end{pmatrix}_{(\mathrm{i}+1)} = \frac{\hbar}{m^*} \begin{bmatrix} k_{\mathrm{F}} \sin(\varphi_{\mathrm{i}}) \\ k_{\mathrm{F}} \cos(\varphi_{\mathrm{i}}) \end{bmatrix} \cdot \tau + \begin{pmatrix} x \\ y \end{pmatrix}_{\mathrm{i}}. \tag{A.7}$$

After a certain number of scattering events N the S_{z} component of spin polarization and the spin position is transferred to a two-dimensional false-color plot histogram which displays the spin polarization in dependence on the spatial position for a time $t_{\mathrm{d}} = N \cdot \tau$ after the excitation. Modeling the Gaussian laser beam profile the initial position (x_0, y_0) of each spin is randomly sampled from a Gaussian distribution around the origin with a FWHM equivalent to the spot size of the laser. Due to a large number of electrons the bins in the false-color plot are filled up with the sum of all z spin components $\sum_{\mathrm{i}} S_{\mathrm{z}}^{\mathrm{i}}$ assigned to the specific area covered by the bin.

Bibliography

[1] A. Acin, I. Bloch, H. Buhrman, T. Calarco, C. Eichler, J. Eisert, D. Esteve, N. Gisin, S. J. Glaser, F. Jelezko, et al., “The quantum technologies roadmap: a European community view,” *New Journal of Physics* **20**, 080201 (2018)

[2] W. Gerlach and O. Stern, “Der experimentelle Nachweis der Richtungsquantelung im Magnetfeld,” *Zeitschrift für Physik* **9**, 349–352 (1922)

[3] G. E. Uhlenbeck and S. Goudsmit, “Ersetzung der Hypothese vom unmechanischen Zwang durch eine Forderung bezüglich des inneren Verhaltens jedes einzelnen Elektrons,” *Die Naturwissenschaften* **13**, 953–954 (1925)

[4] G. E. Uhlenbeck and S. Goudsmit, “Spinning Electrons and the Structure of Spectra,” *Nature* **117**, 264–265 (1926)

[5] P. A. M. Dirac, “The quantum theory of the electron,” *Proceedings of the Royal Society of London A: Mathematical, Physical and Engineering Sciences* **117**, 610–624 (1928)

[6] F. M. Wanlass and C. T. Sah, “Nanowatt logic using field-effect metal-oxide semiconductor triodes,” in: *Semiconductor Devices: Pioneering Papers*, (World Scientific, 1991) 637–638

[7] G. Moore, “Moore’s law,” *Electronics Magazine* **38**, (1965)

[8] M. M. Waldrop, “The chips are down for Moore’s law,” *Nature News* **530**, 144 (2016)

[9] R. F. Service, “Chipmakers look past Moore’s law, and silicon.,” *Science (New York, NY)* **361**, 321 (2018)

[10] J. Hruska, *"Details Leak on Intel’s Upcoming Ice Lake CPU, 10nm Schedule"*, ExtremeTech, (2017)

[11] D. D. Awschalom and M. E. Flatté, “Challenges for semiconductor spintronics,” *Nature physics* **3**, 153 (2007)

[12] R. Landauer, “Irreversibility and heat generation in the computing process,” *IBM journal of research and development* **5**, 183–191 (1961)

[13] T. Schäpers, *Semiconductor Spintronics* (Walter de Gruyter GmbH & Co KG, 2016)

[14] M. Julliere, “Tunneling between ferromagnetic films,” *Physics letters A* **54**, 225–226 (1975)

[15] M. Johnson and R. H. Silsbee, “Interfacial charge-spin coupling: Injection and detection of spin magnetization in metals,” *Physical Review Letters* **55**, 1790 (1985)

[16] M. N. Baibich, J. M. Broto, A. Fert, F. N. Van Dau, F. Petroff, P. Etienne, G. Creuzet, A. Friederich and J. Chazelas, “Giant magnetoresistance of (001) Fe/(001) Cr magnetic superlattices,” *Physical review letters* **61**, 2472 (1988)

[17] G. Binasch, P. Grünberg, F. Saurenbach and W. Zinn, "Enhanced magnetoresistance in layered magnetic structures with antiferromagnetic interlayer exchange," *Physical review B* **39**, 4828 (1989)

[18] S. Datta and B. Das, "Electronic analog of the electro-optic modulator," *Applied Physics Letters* **56**, 665–667 (1990)

[19] A. Trabesinger, "Quantum computing: towards reality," *Nature* **543**, S1–S1 (2017)

[20] H. Häffner, C. F. Roos and R. Blatt, "Quantum computing with trapped ions," *Physics reports* **469**, 155–203 (2008)

[21] J. Clarke and F. K. Wilhelm, "Superconducting quantum bits," *Nature* **453**, 1031 (2008)

[22] M. Veldhorst, J. C. C. Hwang, C. H. Yang, A. W. Leenstra, B. de Ronde, J. P. Dehollain, J. T. Muhonen, F. E. Hudson, K. M. Itoh, A. Morello, et al., "An addressable quantum dot qubit with fault-tolerant control-fidelity," *Nature nanotechnology* **9**, 981 (2014)

[23] D. Loss and D. P. DiVincenzo, "Quantum computation with quantum dots," *Physical Review A* **57**, 120 (1998)

[24] J. M. Kikkawa, I. P. Smorchkova, N. Samarth and D. D. Awschalom, "Room-temperature spin memory in two-dimensional electron gases," *Science* **277**, 1284–1287 (1997)

[25] G. Kalai, "How quantum computers fail: quantum codes, correlations in physical systems, and noise accumulation," *arXiv preprint arXiv:1106.0485*, (2011)

[26] G. Kalai and G. Kindler, "Gaussian noise sensitivity and BosonSampling," *arXiv preprint arXiv:1409.3093*, (2014)

[27] M. I. Dyakonov, "The case against quantum computing," *IEEE Spectrum*, (2018)

[28] W. H. Lau and M. E. Flatté, "Tunability of electron spin coherence in III–V quantum wells," *Journal of applied physics* **91**, 8682–8684 (2002)

[29] A. Manchon, H. C. Koo, J. Nitta, S. M. Frolov and R. A. Duine, "New perspectives for Rashba spin–orbit coupling," *Nature materials* **14**, 871 (2015)

[30] T. Kuschel and G. Reiss, "Spin orbitronics: Charges ride the spin wave," *Nature nanotechnology* **10**, 22 (2015)

[31] M. I. Dyakonov and V.I. Perel, "Current-induced spin orientation of electrons in semiconductors," *Physics Letters A* **35**, 459–460 (1971)

[32] J. E. Hirsch, "Spin hall effect," *Physical Review Letters* **83**, 1834 (1999)

[33] K. D. Petersson, L. W. McFaul, M. D. Schroer, M. Jung, J. M. Taylor, A. A. Houck and J. R. Petta, "Circuit quantum electrodynamics with a spin qubit," *Nature* **490**, 380 (2012)

[34] S. Fukami, C. Zhang, S. DuttaGupta, A. Kurenkov and H. Ohno, "Magnetization switching by spin–orbit torque in an antiferromagnet–ferromagnet bilayer system," *Nature materials* **15**, 535 (2016)

[35] E. Gibney and D. Castelvecchi, *Nobel for 2D exotic matter*, 2016

[36] M. König, S. Wiedmann, C. Brüne, A. Roth, H. Buhmann, L.W. Molenkamp, X. Qi and S. Zhang, "Quantum spin Hall insulator state in HgTe quantum wells," *Science* **318**, 766–770 (2007)

[37] R. M. Lutchyn, J. D. Sau and S. D. Sarma, "Majorana fermions and a topological phase transition in semiconductor-superconductor heterostructures," *Physical review letters* **105**, 077001 (2010)

[38] J. R. Schaibley, H. Yu, G. Clark, P. Rivera, J. S. Ross, K. L. Seyler, W. Yao and X. Xu, "Valleytronics in 2D materials," *Nature Reviews Materials* **1**, 16055 (2016)

[39] G. Dresselhaus, "Spin-orbit coupling effects in zinc blende structures," *Physical Review* **100**, 580 (1955)

[40] E. I. Rashba, "Properties of semiconductors with an extremum loop. I. Cyclotron and combinational resonance in a magnetic field perpendicular to the plane of the loop," *Physics of the Solid State* **2**, 1109–1122 (1960)

[41] M. I. Dyakonov and V. Y. Kachorovskii, "Fiz. Tech. Poluprovodn. 20, 178 (1986)," *Sov. Phys. Semicond* **20**, 110 (1986)

[42] A.V. Poshakinskiy and S.A. Tarasenko, "Spatiotemporal spin fluctuations caused by spin-orbit-coupled Brownian motion," *Physical Review B* **92**, 045308 (2015)

[43] S. D. Ganichev and L. E. Golub, "Interplay of Rashba/Dresselhaus spin splittings probed by photogalvanic spectroscopy–A review," *physica status solidi (b)* **251**, 1801–1823 (2014)

[44] B. A. Bernevig, J. Orenstein and S. Zhang, "Exact SU (2) symmetry and persistent spin helix in a spin-orbit coupled system," *Physical review letters* **97**, 236601 (2006)

[45] J. D. Koralek, C. P. Weber, J. Orenstein, B. A. Bernevig, S. Zhang, S. Mack and D. D. Awschalom, "Emergence of the persistent spin helix in semiconductor quantum wells," *Nature* **458**, 610 (2009)

[46] V. N. Gridnev, "Anisotropic spin diffusion in a semiconductor quantum well," *Journal of Experimental and Theoretical Physics Letters* **76**, 502–506 (2002)

[47] S. Anghel, A. Singh, F. Passmann, H. Iwata, J. N. Moore, G. Yusa, X. Li and M. Betz, "Enhanced spin-polarization lifetimes in a two-dimensional electron gas in a gate-controlled GaAs quantum well," *Physical Review B* **94**, 035303 (2016)

[48] M. P. Walser, C. Reichl, W. Wegscheider and G. Salis, "Direct mapping of the formation of a persistent spin helix," *Nature Physics* **8**, 757 (2012)

[49] A. Sasaki, S. Nonaka, Y. Kunihashi, M. Kohda, T. Bauernfeind, T. Dollinger, K. Richter and J. Nitta, "Direct determination of spin–orbit interaction coefficients and realization of the persistent spin helix symmetry," *Nature nanotechnology* **9**, 703 (2014)

[50] B. Jusserand, D. Richards, H. Peric and B. Etienne, "Zero-magnetic-field spin splitting in the GaAs conduction band from Raman scattering on modulation-doped quantum wells," *Physical review letters* **69**, 848 (1992)

[51] S. Anghel, F. Passmann, A. Singh, C. Ruppert, A. V. Poshakinskiy, S.A. Tarasenko, J.N. Moore, G. Yusa, T. Mano, T. Noda, et al., "Field control of anisotropic spin transport and spin helix dynamics in a modulation-doped GaAs quantum well," *Physical Review B* **97**, 125410 (2018)

[52] K. Yoshizumi, A. Sasaki, M. Kohda and J. Nitta, "Gate-controlled switching between persistent and inverse persistent spin helix states," *Applied Physics Letters* **108**, 132402 (2016)

[53] Y. Kunihashi, H. Sanada, H. Gotoh, K. Onomitsu, M. Kohda, J. Nitta and T. Sogawa, "Drift transport of helical spin coherence with tailored spin–orbit interactions," *Nature communications* **7**, 10722 (2016)

[54] P. Altmann, F. G. G. Hernandez, G. J. Ferreira, M. Kohda, C. Reichl, W. Wegscheider and G. Salis, "Current-controlled spin precession of quasistationary electrons in a cubic spin-orbit field," *Physical review letters* **116**, 196802 (2016)

[55] Y. Kunihashi, H. Sanada, Y. Tanaka, H. Gotoh, K. Onomitsu, K. Nakagawara, M. Kohda, J. Nitta and T. Sogawa, "Drift-Induced Enhancement of Cubic Dresselhaus Spin-Orbit Interaction in a Two-Dimensional Electron Gas," *Physical review letters* **119**, 187703 (2017)

[56] F. Passmann, S. Anghel, T. Tischler, A. V. Poshakinskiy, S. A. Tarasenko, G. Karczewski, T. Wojtowicz, A. D. Bristow and M. Betz, "Persistent spin helix manipulation by optical doping of a CdTe quantum well," *Physical Review B* **97**, 201413 (2018)

[57] M. Schwemmer, A. Hanninger, M. Weingartner, M. Oltscher, M. Ciorga, D. Weiss, D. Schuh, D. Bougeard, T. Korn and C. Schüller, "Deterministic transfer of spin polarization in wire-like lateral structures via the persistent spin helix," *Applied Physics Letters* **109**, 172106 (2016)

[58] F. Dettwiler, J. Fu, S. Mack, P. J. Weigele, J. C. Egues, D. D. Awschalom and D. M. Zumbühl, "Stretchable persistent spin helices in GaAs quantum wells," *Physical Review X* **7**, 031010 (2017)

[59] G. J. Ferreira, F. G. G. Hernandez, P. Altmann and G. Salis, "Spin drift and diffusion in one-and two-subband helical systems," *Physical Review B* **95**, 125119 (2017)

[60] M. Luengo-Kovac, F. C. D. Moraes, G. J. Ferreira, A. S. L. Ribeiro, G.M. Gusev, A. K. Bakarov, V. Sih and F. G. G. Hernandez, "Gate control of the spin mobility through the modification of the spin-orbit interaction in two-dimensional systems," *Physical Review B* **95**, 245315 (2017)

[61] J. Fu, P. H. Penteado, M. O. Hachiya, D. Loss and J. C. Egues, "Persistent Skyrmion Lattice of Noninteracting Electrons with Spin-Orbit Coupling," *Physical review letters* **117**, 226401 (2016)

[62] W. Nolting, *Grundkurs Theoretische Physik 5/2: Quantenmechanik - Methoden und Anwendungen*, Springer-Lehrbuch (Springer Berlin Heidelberg, 2014)

[63] F. Schwabl, *Quantenmechanik (QM I): Eine Einführung*, Springer-Lehrbuch (Springer Berlin Heidelberg, 2007)

[64] P. Zeeman, *Philosophical Magazine* (Taylor & Francis, 1897)

[65] A. Landé, "Über den anomalen Zeemaneffekt (Teil I)," *Zeitschrift für Physik* **5**, 231–241 (1921)

[66] W. Pauli, "Über den Einfluß der Geschwindigkeitsabhängigkeit der Elektronenmasse auf den Zeemaneffekt," *Zeitschrift fur Physik* **31**, 373–385 (1925)

[67] F. Schwabl, *Quantenmechanik für Fortgeschrittene: QM II*, Springer-Lehrbuch (Springer Berlin Heidelberg, 2013)

[68] O. B. Klein, "Quantentheorie und fünfdimensionale Relativitätstheorie," *Zeitschrift für Physik* **37**, 895–906 (1926)

[69] W. Gordon, "Der Comptoneffekt nach der Schrödingerschen Theorie," *Zeitschrift für Physik* **40**, 117–133 (1926)

[70] L. L. Foldy and S. A. Wouthuysen, "On the Dirac theory of spin 1/2 particles and its non-relativistic limit," *Physical Review* **78**, 29 (1950)

[71] F. Bloch, “Über die Quantenmechanik der Elektronen in Kristallgittern,” *Zeitschrift für Physik* **52**, 555–600 (1929)

[72] C. F. Klingshirn, *Semiconductor Optics*, Graduate Texts in Physics (Springer Berlin Heidelberg, 2012)

[73] M. Grundmann, *The Physics of Semiconductors: An Introduction Including Nanophysics and Applications*, Graduate Texts in Physics (Springer Berlin Heidelberg, 2010)

[74] N. W. Ashcroft and D. N. Mermin, *Festkörperphysik* (Oldenbourg Wissenschaftsverlag, 2012)

[75] H. Hellmann, “A new approximation method in the problem of many electrons,” *The Journal of Chemical Physics* **3**, 61–61 (1935)

[76] B. C. Taylor and O. Madelung, *Introduction to Solid-State Theory*, Springer Series in Solid-State Sciences (Springer Berlin Heidelberg, 2012)

[77] J. C. Slater and G. F. Koster, “Simplified LCAO Method for the Periodic Potential Problem,” *Phys. Rev.* **94**, 1498–1524 (1954)

[78] P. Y. Yu and M. Cardona, *Fundamentals of semiconductors: physics and materials properties* (Springer, 1996)

[79] G. F. Koster, J. O. Dimmock, R. G. Wheeler and H. Statz, “Properties of the 32 point groups,” *MIT Press, Cambridge* **1**, 963 (1963)

[80] S. M. Sze, *Semiconductor devices: physics and technology* (John Wiley Sons, 2008)

[81] D. B. Roundy, B. Sun and J. V. Schenck, *Physics 427 Lecture*, 2017, URL: `http://physics.oregonstate.edu/~roundyd/COURSES/ph427/index.html`

[82] E. Noether, “Invariante variationsprobleme, Nachr. d. König. Gesellsch. d. Wiss. zu Göttingen, Math-phys. Klasse (1918) 235–257,” *English Reprint: physics/0503066, http://dx. doi. org/10.1080/00411457108231446* **57**, (1918)

[83] M. Fox, *Optical Properties of Solids*, Oxford Master Series in Physics (OUP Oxford, 2010)

[84] E. Fermi, *Nuclear physics: a course given by Enrico Fermi at the University of Chicago* (University of Chicago Press, 1950)

[85] K. Seeger, “Semiconductor Physics (Springer-Verlag, Berlin, 1997).,”

[86] I. Žutić, J. Fabian and S. D. Sarma, “Spintronics: Fundamentals and applications,” *Reviews of modern physics* **76**, 323 (2004)

[87] S. A. Wolf, D. D. Awschalom, R. A. Buhrman, J. M. Daughton, S. Molnar, M. L. Roukes, A. Y. Chtchelkanova and D. M. Treger, “Spintronics: A Spin-Based Electronics Vision for the Future,” *Science* **294**, 1488–1495 (2001)

[88] P. Drude, “Zur elektronentheorie der metalle,” *Annalen der Physik* **306**, 566–613 (1900)

[89] C. Kittel, *Introduction to Solid State Physics* (Wiley, 2004)

[90] P. L. Bhatnagar, E. P. Gross and M. Krook, “A model for collision processes in gases. I. Small amplitude processes in charged and neutral one-component systems,” *Physical review* **94**, 511 (1954)

[91] J. Fabian, A. Matos-Abiague, C. Ertler, P. Stano and I. Žutić, “Semiconductor spintronics,” *Acta Physica Slovaca. Reviews and Tutorials* **57**, 565–907 (2007)

[92] K. Seeger, *Semiconductor Physics: An Introduction*, Advanced Texts in Physics (Springer Berlin Heidelberg, 2013)

[93] A. Einstein, “Über die von der molekularkinetischen Theorie der Wärme geforderte Bewegung von in ruhenden Flüssigkeiten suspendierten Teilchen,” *Annalen der Physik* **322**, 549–560 (1905)

[94] C. Hamaguchi, *Basic semiconductor physics*, vol. 212 (Springer, 2001)

[95] G. Slavcheva and P. Roussignol, *Optical Generation and Control of Quantum Coherence in Semiconductor Nanostructures*, NanoScience and Technology (Springer Berlin Heidelberg, 2010)

[96] M. I. Dyakonov, *Spin Physics in Semiconductors*, Springer Series in Solid-State Sciences (Springer Berlin Heidelberg, 2008)

[97] E. L. Ivchenko, “Optical Spectroscopy of Semiconductor Nanostructures (Alpha Science, Harrow, UK, 2005),” *Google Scholar*

[98] H. A. Kramers, “HA Kramers, Proc. Acad. Sci. Amsterdam 33, 959 (1930).,” in: *Proc. Acad. Sci. Amsterdam*, vol. 33, (1930) 959

[99] L. D. Landau and L. M. Lifschitz, *Lehrbuch der theoretischen Physik*, vol. 6 (Akademie-Verlag Berlin, 1981)

[100] R. Winkler, *Spin-orbit coupling effects in two-dimensional electron and hole systems*, vol. 191 (Springer Science & Business Media, 2003)

[101] J. Schliemann, “Colloquium: Persistent spin textures in semiconductor nanostructures,” *Reviews of Modern Physics* **89**, 011001 (2017)

[102] J. Ishihara, Y. Ohno and H. Ohno, “Direct imaging of gate-controlled persistent spin helix state in a modulation-doped GaAs/AlGaAs quantum well,” *Applied Physics Express* **7**, 013001 (2013)

[103] M. Faraday, “Faraday, M., 1846, Philos. Trans. R. Soc. London 136, 104.,” *Philos. Trans. R. Soc. London* **136**, 104 (1846)

[104] E. Hecht and K. Lippert, *Optik*, De Gruyter Studium Series (Walter de Gruyter GmbH, 2018)

[105] J. Kerr, “XLIII. On rotation of the plane of polarization by reflection from the pole of a magnet,” *The London, Edinburgh, and Dublin Philosophical Magazine and Journal of Science* **3**, 321–343 (1877)

[106] S. Sugano and N. Kojima, *Magneto-Optics*, Springer Series in Solid-State Sciences (Springer Berlin Heidelberg, 2013)

[107] R. F. Wallis and M. Balkanski, *Many-body aspects of solid state spectroscopy* (North-Holland, 1986)

[108] J. Shah, *Ultrafast spectroscopy of semiconductors and semiconductor nanostructures*, vol. 115 (Springer Science & Business Media, 2013)

[109] A. Singh, G. Moody, S. Wu, Y. Wu, N. J. Ghimire, J. Yan, D. G. Mandrus, Xi. Xu and X. Li, “Coherent electronic coupling in atomically thin MoSe 2,” *Physical review letters* **112**, 216804 (2014)

[110] S. Adachi, *Properties of group-IV, III-V and II-VI semiconductors, series in materials for electronic and optoelectronic application*, 2005

[111] H. Haken and H. Wolf, *Atom-und Quantenphysik: Einführung in die experimentellen und theoretischen Grundlagen. vol. 8., aktualisierte u. erw. Aufl*, 2004

[112] A. N. Chantis, M. van Schilfgaarde and T. Kotani, “Ab initio prediction of conduction band spin splitting in zinc blende semiconductors,” *Physical review letters* **96**, 086405 (2006)

[113] L. Vina, “Spin relaxation in low-dimensional systems,” *Journal of Physics: Condensed Matter* **11**, 5929 (1999)

[114] G. S. Marlow and M. B. Das, “The effects of contact size and non-zero metal resistance on the determination of specific contact resistance,” *Solid-State Electronics* **25**, 91–94 (1982)

[115] B.A. Piot, J. Kunc, M. Potemski, D.K. Maude, C. Betthausen, A. Vogl, D. Weiss, G. Karczewski and T. Wojtowicz, “Fractional quantum Hall effect in CdTe,” *Physical Review B* **82**, 081307 (2010)

[116] O. Madelung, *Semiconductors: Data Handbook* (Springer Berlin Heidelberg, 2004)

[117] B. M. Ashkinadze, V. V. Rudenkov, P. C. M. Christianen, J. C. Maan, E. Linder, E. Cohen and L. N. Pfeiffer, “Photoluminescence spectral evolution from 2DEG-free hole to charged excitons in modulation-doped GaAs/AlGaAs quantum wells,” *physica status solidi (c)* **1**, 510–513 (2004)

[118] V. Huard, R. T. Cox, K. Saminadayar, A. Arnoult and S. Tatarenko, “Bound States in Optical Absorption of Semiconductor Quantum Wells Containing a Two-Dimensional Electron Gas,” *Physical Review Letters* **84**, 187–190 (2000)

[119] G. Yusa, H. Shtrikman and I. Bar-Joseph, “Onset of exciton absorption in modulation-doped GaAs quantum wells,” *Phys. Rev. B* **62**, 15390–15393 (2000)

[120] V. P. Kochereshko, G. V. Astakhov, D. R. Yakovlev, W. Ossau, G. Landwehr, T. Wojtowicz, G. Karczewski and J. Kossut, “Excitons and Trions in II–VI Quantum Wells with Modulation Doping,” *physica status solidi (b)* **221**, 345–348 (2000)

[121] C. Aku-Leh, F. Perez, B. Jusserand, D. Richards, W. Pacuski, P. Kossacki, M. Menant and G. Karczewski, “Measuring the spin polarization and Zeeman energy of a spin-polarized electron gas: Comparison between Raman scattering and photoluminescence,” *Physical Review B* **76**, 155416 (2007)

[122] F. Baboux, F. Perez, C. A. Ullrich, G. Karczewski and T. Wojtowicz, “Electron density magnification of the collective spin-orbit field in quantum wells,” *Physical Review B* **92**, 125307 (2015)

[123] C. Schoenhuber, M. P. Walser, G. Salis, C. Reichl, W. Wegscheider, T. Korn and C. Schueller, “Inelastic light-scattering from spin-density excitations in the regime of the persistent spin helix in a GaAs-AlGaAs quantum well,” *Physical Review B* **89**, 085406 (2014)

[124] G. Salis, M. P. Walser, P. Altmann, C. Reichl and W. Wegscheider, “Dynamics of a localized spin excitation close to the spin-helix regime,” *Physical Review B* **89**, 045304 (2014)

[125] W. J. H. Leyland, G. H. John, R. T. Harley, M. M. Glazov, E. L. Ivchenko, D. A. Ritchie, I. Farrer, A.J . Shields and M. Henini, “Enhanced spin-relaxation time due to electron-electron scattering in semiconductor quantum wells,” *Physical Review B* **75**, 165309 (2007)

[126] P. Altmann, M. P. Walser, C. Reichl, W. Wegscheider and G. Salis, "Suppressed decay of a laterally confined persistent spin helix," *Physical Review B* **90**, 201306 (2014)

[127] N. S. Averkiev and L. E. Golub, "Giant spin relaxation anisotropy in zinc-blende heterostructures," *Physical Review B* **60**, 15582 (1999)

[128] R. M. Hannak, M. Oestreich, A. P. Heberle, W. W. Ru and K. Ko, "Electron g factor in quantum wells determined by spin quantum beats," *Solid state communications* **93**, 313–317 (1995)

[129] M. J. Snelling, G. P. Flinn, A. S. Plaut, R. T. Harley, A. C. Tropper, R. Eccleston and C. C. Phillips, "Magnetic g factor of electrons in GaAs/Al x Ga 1- x As quantum wells," *Physical Review B* **44**, 11345 (1991)

[130] M. J. Snelling, E Blackwood, C. J. McDonagh, R. T. Harley and C. T. B. Foxon, "Exciton, heavy-hole, and electron g factors in type-I GaAs/Al x Ga 1- x As quantum wells," *Physical Review B* **45**, 3922 (1992)

[131] J. Kunc, B. A. Piot, D. K. Maude, M. Potemski, R. Grill, C. Betthausen, D. Weiss, V. Kolkovsky, G. Karczewski and T. Wojtowicz, "Magnetoresistance quantum oscillations in a magnetic two-dimensional electron gas," *Physical Review B* **92**, 085304 (2015)

[132] B. Van Zeghbroeck, "Principles of semiconductor devices," *Colarado University* **34**, (2004)

[133] J. Shah, A. Pinczuk, H. L. Störmer, A. C. Gossard and W. Wiegmann, "Hot electrons in modulation-doped GaAs-AlGaAs heterostructures," *Applied Physics Letters* **44**, 322–324 (1984)

[134] J. Shah, A. Pinczuk, H.L. Störmer, A.C. Gossard and W. Wiegmann, "Electric field induced heating of high mobility electrons in modulation-doped GaAs-AlGaAs heterostructures," *Applied Physics Letters* **42**, 55–57 (1983)

[135] R.A. Höpfel and G. Weimann, "Electron heating and free-carrier absorption in GaAs/AlGaAs single heterostructures," *Applied Physics Letters* **46**, 291–293 (1985)

[136] C. H. Yang, J. M. Carlson-Swindle, S. A. Lyon and J. M. Worlock, "Hot-electron relaxation in GaAs quantum wells," *Physical review letters* **55**, 2359 (1985)

[137] G. V. Budkin and S. A. Tarasenko, "Heating and cooling of a two-dimensional electron gas by terahertz radiation," *Journal of Experimental and Theoretical Physics* **112**, 656–663 (2011)

[138] A. A. Verevkin, N. G. Ptitsina, K. V. Smirnov, G. N. Gol'tsman, E. M. Gershenzon and K. S. Ingvesson, "Direct measurements of energy relaxation times on an AlGaAs/GaAs heterointerface in the range 4.2–50 K," *Journal of Experimental and Theoretical Physics Letters* **64**, 404–409 (1996)

[139] L. Meier, G. Salis, I. Shorubalko, E. Gini, S. Schön and K. Ensslin, "Measurement of Rashba and Dresselhaus spin–orbit magnetic fields," *Nature Physics* **3**, 650 (2007)

[140] E. D. Palik, "Handbook of Optical Constants of Solids (Academic, Orlando, 1985)," *Google Scholar*, 286–297

[141] S. Adachi and T. Kimura, "Optical constants of Zn1-xCdxTe ternary alloys: experiment and modeling," *Japanese journal of applied physics* **32**, 3496 (1993)

[142] E. A. Zhukov, D. R. Yakovlev, M. Bayer, M. M. Glazov, E. L. Ivchenko, G. Karczewski, T. Wojtowicz and J. Kossut, "Spin coherence of a two-dimensional electron gas induced by resonant excitation of trions and excitons in CdTeˆﬀl(Cd, Mg)Te quantum wells," *Phys. Rev. B* **76**, 205310 (2007)

[143] E. A. Zhukov, D. R. Yakovlev, M. M. Glazov, L. Fokina, G. Karczewski, T. Wojtowicz, J. Kossut and M. Bayer, “Optical control of electron spin coherence in CdTe/(Cd, Mg) Te quantum wells,” *Physical Review B* **81**, 235320 (2010)

[144] Y. Kunihashi, M. Kohda, H. Sanada, H. Gotoh, T. Sogawa and J. Nitta, “Proposal of spin complementary field effect transistor,” *Applied Physics Letters* **100**, 113502 (2012)

[145] T. Jungwirth, J. Wunderlich and K. Olejník, “Spin Hall effect devices,” *Nature materials* **11**, 382 (2012)

[146] P. Chuang, S. Ho, L. W. Smith, F. Sfigakis, M. Pepper, C. Chen, J. Fan, J. P. Griffiths, I. Farrer, H. E. Beere, et al., “All-electric all-semiconductor spin field-effect transistors,” *Nature nanotechnology* **10**, 35 (2015)

[147] K. Mak, K. L. McGill, J. Park and P. L. McEuen, “The valley Hall effect in MoS2 transistors,” *Science* **344**, 1489–1492 (2014)

[148] J. Wunderlich, B. Park, A. C. Irvine, L.P. Zârbo, E. Rozkotová, P. Nemec, V. Novák, J. Sinova and T. Jungwirth, “Spin Hall effect transistor,” *Science* **330**, 1801–1804 (2010)

[149] J. Sinova, S. O. Valenzuela, J. Wunderlich, C. H. Back and T. Jungwirth, “Spin hall effects,” *Reviews of Modern Physics* **87**, 1213 (2015)

[150] R. Kurosawa, K. Morita, M. Kohda and Y. Ishitani, “Effect of cubic Dresselhaus spin-orbit interaction in a persistent spin helix state including phonon scattering in semiconductor quantum wells,” *Applied Physics Letters* **107**, 182103 (2015)

[151] D. Iizasa, D. Sato, K. Morita, J. Nitta and M. Kohda, “Robustness of a persistent spin helix against a cubic Dresselhaus field in (001) and (110) oriented two-dimensional electron gases,” *Physical Review B* **98**, 165112 (2018)

Symbols and Acronyms

Symbol or Acronym	Meaning
$\boldsymbol{A}(\boldsymbol{r},\boldsymbol{t})$	vector potential
A_0	amplitude parameter of the PSH fit function
a	spin-orbit coupling constant
α	Rashba parameter
α_0	Rashba parameter as grown
BIA	bulk inversion asymmetry
$\boldsymbol{B}$	magnetic field vector
$\boldsymbol{B}_{\mathrm{so}}(\boldsymbol{k}) = (B_{\mathrm{so,x}}, B_{\mathrm{so,y}}, B_{\mathrm{so,z}})$	effective magnetic field vector
$\boldsymbol{B}_{\mathrm{ex}}(\boldsymbol{k}) = (B_{\mathrm{ex,x}}, B_{\mathrm{ex,y}}, B_{\mathrm{ex,z}})$	external magnetic field vector
b_{QW}	width of the QW channel
β	Dresselhaus SO coupling parameter
β_1	linear Dresselhaus SO coupling parameter
β_3	cubic Dresselhaus SO coupling parameter
c	velocity of light
CCD	charge coupled device
DPSH	drifting persistent spin helix
DP	Dyakonov-Perel
Δ_{so}	split-off energy
Δ	energy difference in between $\|1\rangle$ and $\|2\rangle$
$\boldsymbol{D}$	displacement vector
d_{QW}	QW thickness (quantization axis)
E	energy
$\delta\mathcal{E}$	electric depolarization field
$\boldsymbol{\mathcal{E}}$	electric field
E_{F}	Fermi energy
E_{g}	band gap energy
$E_{\mathrm{IP}}^{\mathrm{y}}$	external in-plane electric field along y-axis
$E_{\mathrm{IP}}^{\mathrm{x}}$	external in-plane electric field along x-axis
$E_{\mathrm{TPSH}}^{\mathrm{x}}$	electric field of the TPSH regime x-axis
$E_{\mathrm{TPSH}}^{\mathrm{y}}$	electric field of the TPSH regime y-axis
E_{QW}	external out-of-plane electric field

Symbol or Acronym	Meaning
e	electron charge
ϵ_0	vacuum permittivity
$\boldsymbol{\epsilon}(\omega)$	vacuum permittivity tensor
ϵ_{ij}	complex components of $\boldsymbol{\epsilon}(\omega)$
η_{K}	Kerr ellipticity
EOM	electro-optical modulator
FWHM	full width at half maximum
ϕ_0	angle between k_{dif} and x-axis
φ_{i}	Foldy-Wouthuysen transformation
γ	relativistic Lorentz factor
γ_{hw}	spectral transition half-width
Γ_{i}	irreducible group representation
$\boldsymbol{G}$	vector of the reciprocal lattice
g	electron g-factor
$\hbar$	reduced Planck constant
hh	heavy hole
HeNe	Helium-neon laser
I_{op}	optical peak intensity of the laser
$\hat{\boldsymbol{J}}$	total angular momentum operator
J_{s}	spin current
j	total angular momentum quantum number
KR	Kerr rotation
k_{B}	Boltzmann constant
$\boldsymbol{k} = (k_{\mathrm{x}}, k_{\mathrm{y}})$	electron wave vector
$\boldsymbol{k}_{\mathrm{F}}$	Fermi wave vector
$\boldsymbol{k}_{\mathrm{dif}}$	diffusion wave vector
$\boldsymbol{k}_{\mathrm{dr}}$	drift wave vector
$\boldsymbol{L}$	classical angular momentum vector
L_{s}	spin diffusion length
l_{QW}	length of the QW channel
$\hat{\boldsymbol{L}} = (\hat{L}_{\mathrm{x}}, \hat{L}_{\mathrm{y}}, \hat{L}_{\mathrm{z}})$	orbital angular momentum operator
l	azimuthal quantum number
l_{p}	mean free path
lh	light hole
$\|l, m_{\mathrm{l}}\rangle$	angular momentum operator eigenstates
$\lambda_{\mathrm{so,x}}$	transient precession length along the x-axis
$\lambda_{\mathrm{so,y}}$	transient precession length along the y-axis
$\lambda_{0,\mathrm{x}}$	precession length along the x-axis
$\lambda_{0,\mathrm{y}}$	precession length along the y-axis

Symbol or Acronym	Meaning
m	electron mass
m^*	effective electron mass
m_l	orbital angular momentum quantum number
m_s	spin angular momentum quantum number
m_j	total angular momentum quantum number
$\hat{\boldsymbol{\mu}}_\mathrm{j}$	total magnetic moment operator
$\hat{\boldsymbol{\mu}}_\mathrm{l}$	orbital magnetic moment operator
$\hat{\boldsymbol{\mu}}_\mathrm{s}$	spin magnetic moment operator
μ_B	Bohr magneton
μ_e	electron mobility
$\boldsymbol{\mu}(\omega)$	permeability tensor
μ_0	vacuum permeability
MOKE	magneto-optic Kerr effect
$\boldsymbol{M}$	macroscopic magnetization
$N_\pm^2$	complex refractive index
n_0	two-dimensional electron gas density
n_op	photo carrier density
n_e	dynamic two-dimensional electron gas density
n_op	initial photocarrier density
ν_R	laser repetition rate
ω	angular frequency
ω_so	precession frequency caused by SO coupling
ω_L	scalar Larmor precession frequency
$\boldsymbol{\omega_0} = (\omega_\mathrm{x}, \omega_\mathrm{y}, \omega_\mathrm{z})$	vector of Larmor precession frequencies
P_avg	average laser power
$\boldsymbol{p}$	classical momentum vector
$p_\pm$	hopping probabilities for diffusion model
PL	photoluminescence
PSH	persistent spin helix
Q	position
$\boldsymbol{r}$	position vector in Cartesian coordinates
$r_\pm$	complex reflection index
$\boldsymbol{R}$	vector of the direct lattice
$\boldsymbol{R}(T, \Theta)$	three-dimensional rotation matrix
R_QW	resistance of the QW channel
r_B	Bohr radius
$\rho(\hbar\omega)$	density of states
ρ	dimensionless parameter for the depolarization field
$\mathrm{d}R/R$	transient reflection
RT	room-temperature

Symbol or Acronym	Meaning
SHE	spin Hall effect
SIA	structure inversion asymmetry
s	spin quantum number
$s(x, y, t)$	spin polarization in space time
$S_{\mathrm{z}}(x, y, t)$	experimentally detected spin polarization
s_0	initial spin polarization
$\hat{\boldsymbol{S}} = (\hat{S}_{\mathrm{x}}, \hat{S}_{\mathrm{y}}, \hat{S}_{\mathrm{z}})$	spin angular momentum operator
SO	spin-orbit
$\lvert s, m_{\mathrm{s}}\rangle$	eigenstates of the spin operator
$\sigma^{\pm}$	left/ right circularly polarized light
Si-δ	silicon delta layer
Θ_{K}	Kerr rotation angle
Θ_{D}	Debye temperature
θ	angle between wave vector and x-axis
T_{S}	general spin lifetime
T_{c}	carrier lifetime
T_{e}	electron gas temperature
T_1	longitudinal spin lifetime
T_2	transversal spin lifetime
t_{d}	delay time
t_{pulse}	duration of laser pulse
τ	time of flight
τ_{p}	electron-impurity scattering time
τ_{ee}	electron-electron scattering time
τ_{c}	correlation time
TPSH	traveling persistent spin helix
$u_{\boldsymbol{k},\mathrm{n}}$	Bloch function
$U(r)$	crystal potential
$U^{\mathrm{x}}_{\mathrm{IP}}$	in-plane voltage along [110]
$U^{\mathrm{y}}_{\mathrm{IP}}$	in-plane voltage along $[1\bar{1}0]$
$U^{\mathrm{y}}_{\mathrm{BG}}$	back gate voltage
$\boldsymbol{v} = (\hat{v}_{\mathrm{x}}, \hat{v}_{\mathrm{y}}, \hat{v}_{\mathrm{z}})$	velocity vector
$V(\boldsymbol{r})$	potential energy
v_{y1}	temporal gradient of the y_1 parameter
v_{x1}	temporal gradient of the x_1 parameter
v_{Fermi}	Fermi velocity
w_0	initial width of spin polarization
$w(t)$	time-dependent width of spin polarization
X	
x_1	phase parameter of x-axis fit function

Symbol or Acronym	Meaning
x_1'	phase parameter of rearranged x-axis fit function
x_c	center parameter of x-axis fit function
y_1	phase parameter of y-axis fit function
y_1'	phase parameter of rearranged y-axis fit function
y_c	center parameter of y-axis fit function
Z	atomic charge number
$\|0\rangle, \|1\rangle, \|2\rangle$	toy model states
2Dmap	two-dimensional false-color map in space

Publications

B. L. Wilmer, F. Passmann, M. Gehl, G. Khitrova, and A. D. Bristow
“Multidimensional coherent spectroscopy of a semiconductor microcavity”
Physical Review B **91**, 201304 (2015)

J. Debus, D. Kudlacik, V.F. Sapega, D. Dunker, P. Bohn, F. Passmann, D. Braukmann, J. Rautert, D. R. Yakovlev, D. Reuter, A. D. Wieck, and M. Bayer
“Nuclear spin polarization in the electron spin-flip Raman scattering of singly charged (In,Ga)As/GaAs quantum dots”
Physical Review B **92**, 195421 (2015)

S. Anghel, A. Singh, F. Passmann, H. Iwata, J. N. Moore, G. Yusa, X. Li, and M. Betz
“Enhanced spin-polarization lifetimes in a two-dimensional electron gas in a gate-controlled GaAs quantum well”
Physical Review B **94**, 035303 (2016)

S. Anghel, F. Passmann, A. Singh, C. Ruppert, A. V. Poshakinskiy, S. A. Tarasenko, J. N. Moore, G. Yusa, T. Mano, T. Noda, X. Li, A. D. Bristow, and M. Betz
“Field control of anisotropic spin transport and spin helix dynamics in a modulation-doped GaAs quantum well”
Physical Review B **97**, 125410 (2018)

F. Passmann, S. Anghel, T. Tischler, A. V. Poshakinskiy, S. A. Tarasenko, G. Karczewski, T. Wojtowicz, A. D. Bristow, and M. Betz
“Persistent spin helix manipulation by optical doping of a CdTe quantum well”
Physical Review B **97**, 201413 (R) (2018)

S. Anghel, F. Passmann, C. Ruppert, A. D. Bristow and M. Betz
“Coupled exciton-trion spin dynamics in a MoSe2 monolayer”
2D Materials **5**, 045024 (2018)

F. Passmann, A. D. Bristow, J. N. Moore, G. Yusa, T. Mano, T. Noda, M. Betz and S. Anghel
“Transport of a persistent spin helix drifting transverse to the spin texture ”
Physical Review B, submitted (2019)

Acknowledgements

Looking back at the last years, I would like to express my deepest gratitude to all those people who I met during my journey towards this thesis and especially to all those who helped me with all the small and not so small challenges along the way. I am particularly grateful to …

… my advisor Prof. Markus Betz for giving me the opportunity to study and work at E2b, for his scientific guidance and for his patience to discuss every question and every idea that I could possibly came up with.

… Dr. Sergiu Anghel for the great team work, all our never-ending discussions from which I learned more about physics than in any lecture and for his undaunted will to turn our research into reality.

… Prof. Alan D. Bristow whose kind invitation to work with him in Morgantown provided the best motivation to start a career in physics. I am very thankful for Alan's enthusiastic encouragement and his humorous way of supporting Sergiu and me in twirling the Persistent Spin Helix.

… to all our russian colleagues from the Ioffe-Institute. I would like to thank in particular Prof. Mikhail M. Glazov, Prof. Sergey A. Tarasenko and Dr. Alexander V. Poshakinskiy whose outstanding hospitality made my visits in Sankt Petersburg memorable. I like to thank very much Sergey and Sasha for their willingness to explain our sometimes more or less meaningful experimental results and for introducing me to the exciting world of theoretical physics.

… all the colleagues whose amazing team spirit makes working at E2 a remarkable experience. Special thanks should be given to Dr. Elmar Sternemann, Dr. Jan Lohrenz, Dr. Thorben Jostemeier, Stephan Melzer, Jan Mundry, Laura Krauß-Kodytek, Dr. Claudia Ruppert, Daniel Schmidt and Michal Kobecki for their scientific advice and for keeping me entertained during our endless coffee breaks. My special thanks extend to Dr. Akshay Singh for his assistance during the first months at E2b.

… Nina Collette, Katharina Sparka and Michaela Wäscher for their support in fighting all my paper work as well as Lars Wieschollek, Daniel Tüttmann and Klaus Wiegers for sharing their technical expertise and providing us with helium.

… my family and all the friends who made sure to keep me distracted from work from time to time. I am particularly grateful for the unwavering support of my parents Karola and Bernd Paßmann without whom I would have certainly not be able to write a thesis in physics.

… my fiancée Inga Lehmann whose love and support guided me in so numerous ways.

All at the end, I want to express the great joy that my nephews Theo and Til and my niece Marie brought to me. It is my pleasure to see them growing up showing the same curiosity about the world which inherently stands at the first step of any scientific endeavor…

Dortmund, 31st of January 2019, Felix Paßmann